Modeling and Simulation of Neocortical Micro- and Mesocircuitry. Part II: Physiology and Experimentation

James B. Isbister[1,†], András Ecker[1,†], Christoph Pokorny[1,†], Sirio Bolaños-Puchet[1,†], Daniela Egas Santander[1,†], Alexis Arnaudon[1], Omar Awile[1], Natali Barros-Zulaica[1], Jorge Blanco Alonso[1], Elvis Boci[1], Giuseppe Chindemi[1,2], Jean-Denis Courcol[1], Tanguy Damart[1], Thomas Delemontex[1], Alexander Dietz[1], Gianluca Ficarelli[1], Mike Gevaert[1], Joni Herttuainen[1], Genrich Ivaska[1], Weina Ji[1], Daniel Keller[1], James King[1], Pramod Kumbhar[1], Samuel Lapere[1], Polina Litvak[1], Darshan Mandge[1], Eilif B. Muller[1,3,4], Fernando Pereira[1], Judit Planas[1], Rajnish Ranjan[1], Maria Reva[1], Armando Romani[1], Christian Rössert[1], Felix Schürmann[1], Vishal Sood[1], Aleksandra Teska[1], Anil Tuncel[1], Werner Van Geit[1], Matthias Wolf[1], Henry Markram[1,*,‡], Srikanth Ramaswamy[1,5,*,‡], and Michael W. Reimann[1,*,‡]

[1]Blue Brain Project, École polytechnique fédérale de Lausanne (EPFL), Campus Biotech, Geneva, Switzerland
[2]Department of Basic Neurosciences, University of Geneva, Geneva, Switzerland
[3]Department of Neurosciences, Faculty of Medicine, Université de Montréal, Montréal, Canada
[4]CHU Sainte-Justine Research Center, Montréal, Canada
[5]Neural Circuits Laboratory, Newcastle University, Newcastle, UK
[†]Co-lead authors
[‡]Co-senior authors
[*]Corresponding authors

May 17, 2023

Abstract

In recent years, large-scale computational models of the cortex have emerged as a powerful way to study the multi-scale mechanisms of neural processing. However, due to computational costs and difficulty of parameterization, detailed biophysical reconstructions have so far been restricted to small volumes of tissue, where the study of macro- and meso-scale interactions that are central to cortical function is not possible. We describe here, and in a companion paper, an approach to address the scaling challenges and provide a model of multiple interacting cortical regions at a subcellular level of detail. The model consists of 4.2 million morphologically detailed neurons in 8 sub-regions and connected with 13.2 billion synapses through local and long-range connectivity. Its anatomical aspects are described in the companion paper; here, we introduce physiological models of neuronal activity and synaptic transmission that integrate a large number of literature sources and were built using previously published algorithms. Biological neuronal diversity was captured in 208 morpho-electrical neuron types, five types of synaptic short-term dynamics, and pathway-specificity of synaptic parameters. A representation of synaptic input from cortical regions not present in the model was added and efficiently calibrated to reference firing rates. The model exhibits a spectrum of dynamical states differing in the degree to which they are internally versus externally driven. We characterized which parts of the spectrum are compatible with available experimental data on layer-specific delays and amplitudes of responses to simple stimuli, and found an *in vivo*-like regime at the edge of a transition from asynchronous to synchronous spontaneous activity. We developed a rich set of simulation tools to recreate a diverse set of laboratory experiments *in silico*, providing further validation and demonstrating the utility of the model in a variety of paradigms. Finally, we found that the large spatial scale of the model, that incorporates multiple cortical regions, led to the emergence of multiple independent computational units interacting through long-range synaptic pathways. The model provides a framework for the continued integration of experimental findings, for challenging hypotheses and making testable predictions, and provides a foundation for further simulation-based studies of cortical processing and learning.

1 Introduction

The brain operates at multiple scales, from cells and synapses to meso-scale circuits and beyond. Computational models can help us understand its operations, but to bridge these scales, information from different levels of organization must be integrated. Such integration emerges in *large-scale, data-driven, biophysically detailed* models (Markram et al., 2015; Billeh et al., 2020) that differ from more abstract models in that they emphasize *anatomical completeness* of a chosen brain volume over implementing a specific hypothesis about brain function. In this "bottom-up" modelling approach, many constituent models existing at a finer level of detail, are combined into larger models of brain regions. In particular, such a model should explicitly include different cell and synapse types, in the same quantities and configuration as the biological tissue it represents. Of course, models can only approximate this ideal, and must be gradually refined by incorporating additional information. Data-driven, biophysically detailed models can be used to derive new hypotheses, and enable existing hypotheses to be examined in a strict biological and spatial context.

Of perhaps greater importance is the ability to model brain functions in combination with other functions, or in new contexts. While abstract models typically study brain functions in isolation, the actual brain consists of a highly inter-connected network where many parallel computations underlie even simple behavior. In the cortex for example, top-down feedback connections interact with local circuits and inputs from subcortical regions to implement learning and shape perception. The cortex is at the crossroads of multiple interacting functions and mechanisms, at different conceptual and spatial levels. Biophysically detailed models are the ideal and perhaps only way to integrate knowledge and theories about such functions. The principle of anatomical completeness leads to challenges, which must be addressed, however. For example, anything outside the modeled volume will be missing. Consequently, the spatial scale of the model must encompass all interacting mechanisms to be studied. For interactions between brain regions, such as the role of long-range connections, this requires a model of multiple regions with inter-region connectivity.

Previously, we presented a data-driven, biophysically detailed model of a single cortical column of rat neocortex (Markram et al., 2015). While it served to generate insights into mechanisms at that limited spatial scale (Reimann et al., 2013, 2017, 2022b; Nolte et al., 2019, 2020; Newton et al., 2021), we have since expanded the spatial scale of the model by a factor of $\sim$140, modelling the entirety of non-barrel primary somatosensory cortex (nbS1) with inter-region long-range connectivity. In an accompanying manuscript (Reimann et al., 2022a) we describe the anatomical techniques that allowed us, among other improvements, to build the model in an anatomical atlas of these regions and capture synaptic connectivity at the larger scale. Here, we describe the improvements of constituent physiological models, i.e., models of single cell electrophysiology and synaptic physiology, along with the techniques we employ to simulate and validate *in vivo*-like activity in paradigms that recreate a selection of laboratory experiments. To our knowledge, these are the first simulations of *in vivo*-like spontaneous and stimulus-evoked activity of a biophysically detailed cortical model with inter-region connectivity at this scale.

In vivo-like activity and compensating for missing synapses

As mentioned, even if a region model is internally complete, inputs from external sources will still be absent. Critically, a significant fraction of synaptic input may originate from sources external to the model. Unless compensated for, the resulting lack in excitatory drive will prevent achievement of an *in vivo*-like and computationally relevant activity state (see also Billeh et al., 2020). Attempting compensation by changing existing anatomical or physiological parameters would violate the crucial stipulation of anatomical completeness, however. For improved interpretability of simulation results, we instead model the missing synaptic input explicitly through separate mechanisms, and validate the emerging network activity with respect to *in vivo* recordings.

As modeling each individual missing synapse ($\sim$4 times the number of internal synapses (Stepanyants et al., 2009; Markram et al., 2015)) would be too computationally expensive (Cremonesi et al., 2020), we instead model the impact of the activation of these synapses as noisy somatic conductance injections described by an Ornstein-Uhlenbeck (OU) process. Such input compensation must be specific for different neuron populations, however, due to their different firing rates (De Kock et al., 2007; Reyes-Puerta et al., 2015) and the precise laminar innervation profiles of long range projections (Felleman and Van Essen, 1991; Harris et al., 2019; Gao et al., 2022). Finding population-specific input compensation parameters is highly challenging due to the non-linearity and high computational cost of large biophysically detailed simulations. Here we present an automated algorithm which efficiently calibrates population-specific input compensation parameters to attain an *in vivo*-like regime, whilst accounting for the uncertainties associated with recordings of *in vivo* activity.

The result is a three-dimensional spectrum of activity states. The dimensions are defined by three meta-parameters describing aspects of the model's dynamics. The algorithm provides a mapping for each combination of meta-parameters to parameterizations of the input compensation mechanism. The meta-parameters are: the extracellular calcium concentration, which modulates synaptic reliability (Ohana and Sakmann, 1998; Rozov et al., 2001; Borst, 2010), the relative amount of noise in the external input compensation, and the overall activity level, described as a proportion of layer-specific reference firing rates. We determined which combinations of the meta-parameters are compatible with population-specific features of *in vivo* recordings of spontaneous and stimulus-evoked spiking activity. Such rapid and automatic calibration closes the loop for iterative refinement of cortical models.

In simulations of an *in vivo*-like activity state, we then reproduce and build upon experiments from three published studies in rodent cortex. We chose experiments using a wide array of techniques to assess the model under different conditions, and from different, even non-somatosensory brain regions to probe general principles of cortical activity. In addition to comparing our results to the original publication, we provide further analysis taking advantage of our complete knowledge on the internal states of the model. This further demonstrates that the anatomical completeness provided by the bottom-up modelling approach leads to great experimental versatility and enables the exploration of a virtually endless array of paradigms and hypotheses.

Access to the full structural connectome and the metrics outlined in the companion paper, allowed us to explore to what degree heterogeneities in the activity of the model

could be explained by its structural features, both for a smaller subvolume and the full model. For the smaller circuit, this allowed us to present a model which predicts the required input compensation needed for a sub-population based on the estimated mean number of missing synapses per neuron. This validates the assertion that the input compensation represent missing external input. For the entire model, this revealed non-trivial interactions between local and long-range connectivity shaping the emerging activity. Together these results provide insights and tools for calibrating and understanding larger cortical models, and using them to probe the relation between circuit structure and function.

2 Methods

The workflow employed to build the model is outlined in Fig. 1: Based on the anatomy of neurons and synapses (1.), we model neuronal (2.) and synaptic (3.) physiology. We add compensation for missing synapses from outside the modeled volume (4.), which is calibrated to lead to *in vivo*-like activity (5.). As a result, we are able to conduct *in-silico* experimentation (6.) and release the model (7.). Step 1 is described in the accompanying manuscript (Reimann et al., 2022a), while steps 2 and 3 are based on published methods and data (Table 1). They will be summarized in this section, along with descriptions of the remaining steps.

2.1 Anatomy and subvolumes

We base our full model of the nbS1 region on the purely anatomical model described in the accompanying manuscript (Reimann et al., 2022a). That is, we already have the locations and morphologies of neurons, as well as the locations of synaptic contacts. To enable certain analyses and more lightweight simulations, we defined standardized partitions of the model, where a subset of neurons (and their connections) contained in a subvolume are analyzed or simulated separately. We decomposed the volume into full-depth hexagonal prisms of a certain diameter that we call *hexagonal subvolumes*. These are slightly curved, following the geometry of the cortex, and have an intact layer structure. When the diameter of the hexagons is $520\mu m$, comparable to the size of the single cortical column model from (Markram et al., 2015), we call these subvolumes *columns*. Taken together, a *central column* and the six columns surrounding it define a *seven column subvolume*. Additionally, when we separately analyze the excitatory and inhibitory neurons in the different layers, we refer to them as neuron *populations* of the model or a partition of it. Inhibitory neurons that predominantly express PV (parvalbumin), Sst (somatostatin) or 5HT3aR (serotonin receptor 3A) markers, we refer to as *inhibitory subpopulations*. Correspondence with these biological markers was determined based on their morpho-electrical type, as previously done in Markram et al. (2015) (Fig. 2B).

2.2 Neuron physiology

2.2.1 Data on neuron physiology

Electrical models for individual neurons were built based on the *in vitro* recordings described in Reva et al. (2022). Briefly, currents and voltages were recorded for individual neurons under a standardized set of somatic stimuli. Recordings were classified into firing types as in Markram et al. (2015), similar to the Petilla terminology (Ascoli et al., 2008; Markram et al., 2004). The firing types (e-types) are (Fig. 2A): cAC, bAC, cNAC, bNAC, dNAC, cSTUT, bSTUT, dSTUT, cIR, bIR for inhibitory (I) cells, and cAD for excitatory (E) cells. The main differences to the Petilla terminology are that this classification does not have separate classes for 'fast spiking' and 'non-fast, non-adapting' firing, but it contains three types of stuttering cells: 'continuous', 'burst' and 'delayed'. From these recordings, a set of *electrical features*, such as action potential amplitudes, mean frequency, etc. were extracted to serve as constraints when defining electrical models of the individual firing types.

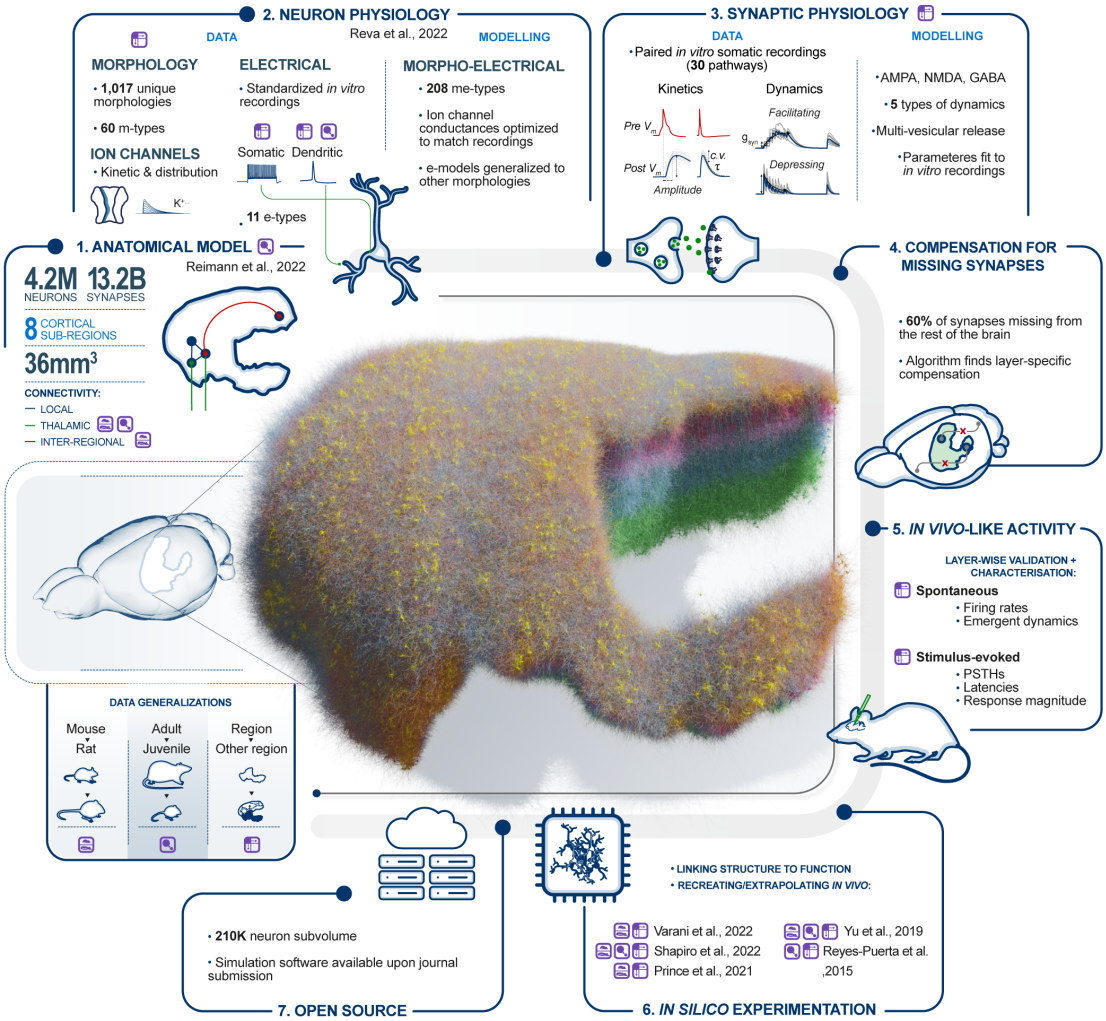

Figure 1: **Overview of the physiology workflow. 1. Anatomical model:** Summary of the anatomical nbS1 model described in the companion paper. **2. Neuron physiology:** Electrical models of single cells were built using previously established methods, from morphological reconstructions, somatic and dendritic recordings of membrane potentials from *in vitro* slice experiments, and ion channel kinetics. **3. Synaptic physiology:** Models of synapses were built using previously established methods, from paired recordings *in vitro*. **4. Compensation for missing synapses:** Excitatory synapses originating from outside nbS1 were compensated with noisy somatic conductance injection, parameterized by a novel algorithm. **5. *In vivo*-like activity:** We calibrated an *in silico* activity regime compatible with *in vivo* spontaneous and stimulus-evoked activity. **6. *In silico* experimentation:** Five laboratory experiments were recreated. Two were used for calibration and three of them were extended beyond their original scope. **7. Open Source:** A seven column subvolume of the model is available on Zenodo (see data availability statement). **Data generalisations:** Three data generalisation strategies were employed to obtain the required data. Left: Mouse to rat, middle: Adult to juvenile (P14) rat, right: Hindlimb (S1HL) and barrel field (S1BF) subregions to the whole nbS1. Throughout the figure, the corresponding purple icons show where these strategies were used.

Table 1: Sources for modeling techniques and data to parameterize them that were combined in this work to model the physiology of nbS1 and conduct *in silico* experimentation.

	Data	
Stage	**Topic**	**Reference**
Neuron physiology	E-type composition	Markram et al. (2004, 2015)
	Electrophysiological recordings	Markram et al. (2015)
		Larkum et al. (2001)
		Nevian et al. (2007)
	Ion-channel models	Reva et al. (2022)
Synaptic physiology	Synaptic pathway physiology	Markram et al. (2015)
		Barros-Zulaica et al. (2019)
		Gupta et al. (2000)
		13 additional sources in
		Suppl. Tables S4, S5, S6
In vivo-like activity	*In vivo* spont. firing rates	Reyes-Puerta et al. (2015)
		De Kock et al. (2007)
	In vivo evoked responses	Reyes-Puerta et al. (2015)
		Yu et al. (2019)
	In vivo thalamic spiking	Diamond et al. (1992)
		Yu et al. (2019)
In silico experimentation	L4 - L2/3 pathway	Varani et al. (2022)
	Visual contrast	Shapiro et al. (2022)
	Coding in inhibitory subtypes	Prince et al. (2021)
	Modeling methods	
Stage	**Topic**	**Reference**
Neuron physiology	E-model building	Van Geit et al. (2016),
		Reva et al. (2022)
Synaptic physiology	Synapse model building	Ecker et al. (2020)
	Model of multi-vesicular release	Barros-Zulaica et al. (2019)
In vivo-like activity	Missing input compensation	*New, original methods
In silico experimentation		*New, original methods

2.2.2 Modeling and validating neuron electrophysiology

The pipeline for electrical model creation described in Reva et al. (2022) was used to build electrical models of all 11 e-types (Fig. 2A). Briefly, an electrical model is a multi-compartment neuron model with several ion channel mechanisms. For each combination of ion channel and compartment type (soma, axon initial segment, basal dendrite, & apical dendrite) a maximal conductance is parameterized. The values of these conductances are optimized with the evolutionary algorithm IBEA (Van Geit et al., 2016) using representative reconstructed neuron morphologies. The cost function to optimize is defined as the sum of the z-scores with respect to the electrical features in the experimental data. Next, for all morphological types in the anatomical model (Reimann et al., 2022a), the corresponding fractions of electrical types are determined from the experimental data as in Markram et al. (2015) (Fig. 2B), resulting in a set of 208 morpho-electrical types. For each of them, all combinations of reconstructed morphologies of the corresponding morphological type with the corresponding electrical model are evaluated with respect to the cost function defined above. A morphology is only used with electrical models where the value of the cost function is below a given threshold. Finally, for the cADpyr e-type, additional electrical features, such as the attenuation of the action potential along

the dendrite, were extracted and compared against experimental data for the purpose of validation (Fig. 2C). For some electrical models, further adjustments were needed to handle the large input currents present under conditions of high network activity. In short, for some pyramidal cell morphologies, the axon initial segment (AIS) was replaced by a cylinder with a length of 60 μm. Its diameter was manually calibrated such that the ratio of the AIS input resistance over the input resistance of somato-dendritic compartments was equal to 2. Afterwards, it was confirmed that the cost function of their electrical models remained below the threshold.

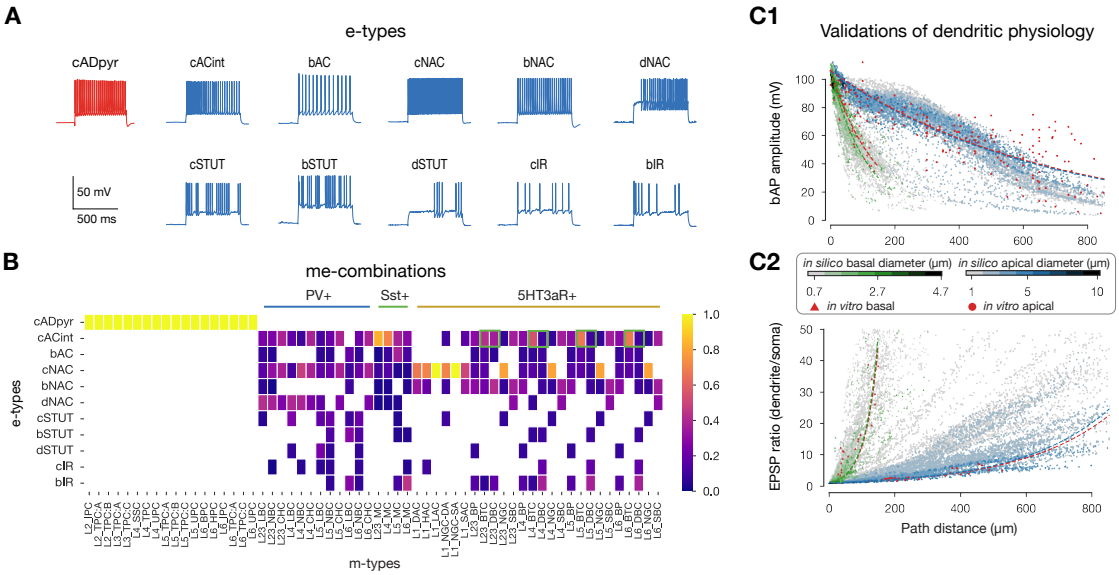

Figure 2: **Neuron physiology. A:** Electrical types used in the model. **B:** Morpho-electric (me) types and me-composition. On top m-types corresponding to I classes are indicated. For some m-types (BTCs and DBCs) the cell class is determined by the me-combination (the cACint e-type belongs to the Sst+ class, which is indicated with green boxes on the heatmap). **C**: Validation of dendritic physiology of L5 TTPCs. **C1**: Validation of the back-propagating action potential (bAP) amplitude. Reference data (in red) comes from Stuart and Sakmann (1994); Larkum et al. (2001) (apical) and Nevian et al. (2007) (basal). **C2:** Validation of EPSP attenuation. Reference data (in red) comes from Berger et al. (2001) (apical) and Nevian et al. (2007) (basal).

2.3 Synaptic physiology

2.3.1 Data on synaptic physiology

For the parameterization of cortico-cortical synaptic physiology we reused paired-recording data sources from Markram et al. (2015). To further constrain the variance of EPSP (excitatory postsynaptic potentials) amplitudes in L5 TTPCs (layer 5 thick-tufted pyramidal cells), we used fitted parameters from Barros-Zulaica et al. (2019). Furthermore, the dataset was also enriched with recent recordings from L6 (Qi and Feldmeyer, 2016; Yang et al., 2020, 2022).

Most of the data used to parameterize synaptic physiology of thalamocortical synapses is also the same as in Markram et al. (2015). However, instead of generalizing (L4 E) peak synaptic conductances for all thalamic fibers, synaptic conductances were constrained using EPSP amplitude measurements from thalamocortical slices (Beierlein and Connors, 2002; Beierlein et al., 2003). Fibers originating from POm (posteriormedial nucleus) were

not present in Markram et al. (2015), but as we did not find any *in vitro* measurements, we generalized physiological parameters from VPM (ventral posteriomedial) synapses to describe POm synapses. Although abundant, the data in Sermet et al. (2019) was collected in mouse brain slices from optogenetically activated thalamic fibers, which differs from the paired-recording or minimal activation paradigm that are more precise, and easier to reproduce *in silico*. Since their results depended on the laser power used, the authors themselves reported EPSP amplitudes normalized relative to the amplitude recorded in L4 E (for VPM) and L5 E (for POm). This allowed relative comparison between the EPSP amplitudes of different populations. To make use of this data, we used it as an external validation dataset (see below).

2.3.2 Modeling synaptic physiology

We used the Markram et al. (2015) model of synaptic physiology, upgraded to feature multi-vesicular release as described in Barros-Zulaica et al. (2019). The model is described in detail in Ecker et al. (2020). In short, synapses are modeled with a stochastic version of the Tsodyks-Markram model (Tsodyks and Markram, 1997; Markram et al., 1998; Fuhrmann et al., 2002; Loebel et al., 2009). This model assumes a pool of available vesicles at each synapse that is utilized by a presynaptic action potential, with a release probability dependent on the extracellular calcium concentration ($[Ca^{2+}]_o$). Additionally, single vesicles spontaneously release with a low frequency as an additional source of variability. The utilization of vesicles leads to a postsynaptic conductance with bi-exponential kinetics. Short-term dynamics of vesicle availability depends on the combination of (U_{SE}, D, and F) parameters, and the resulting synapse dynamics can be facilitating (E1/I1), depressing (E2/I2), or pseudo-linear (I3). We used the same parameter triplets and pathway assignment strategy as in Markram et al. (2015) (Fig. 3D). E synaptic currents consisted of both AMPA and NMDA components, while in most cases I currents consisted of a single $GABA_A$ component, except for neurogliaform cells, whose synapses featured a slow $GABA_B$ component as well. The NMDA component of E synaptic currents depends on the state of the Mg^{2+} block. This nonlinear voltage dependence is described with the Jahr and Stevens (1990) formalism, with parameters fitted to cortical recordings from Vargas-Caballero and Robinson (2003) by Chindemi et al. (2022).

The workflow for determining synaptic model parameters, starting with sparse data from the literature for a subset of parameters and resulting in a dense parameter set for all synaptic pathways, is described for the use case of hippocampal CA1 in Ecker et al. (2020). Briefly, synapse physiology parameters are taken from the literature, and after eventual corrections (for differences in the solutions used in the experiments), they are put directly into the model. However, not all synaptic peak conductances can be measured with paired recordings due to the space-clamp artifact (Markram et al., 2015; Ecker et al., 2020), and estimating the number of release-ready vesicles is also challenging experimentally (Loebel et al., 2009; Barros-Zulaica et al., 2019). Thus, these two parameters were determined in a simulation-driven iterative process. To this end, we reproduced paired recordings *in silico*, delivering spikes from the presynaptic cell and measuring the PSP at the soma of the postsynaptic cell. Peak conductance $\hat{g}$, and the average number of vesicles in the release-ready pool N_{RRP} were then adjusted to match the amplitude and coefficient of variation (CV) of the *in vitro* reference (Ecker et al., 2020). In some cases, this resulted in reaching the lower bound of univesicular release (Barros-Zulaica et al., 2019). Where experimental data was not available, we used mean synaptic physiology pa-

rameters from similar pathways (Markram et al., 2015; Ecker et al., 2020). For the VPM to L5 E pathway, we used the maximum of VPM to L4 E and VPM to L6 E conductances instead of the mean, based on resulting evoked firing rates found in a later modeling step (Supp. Fig. S4C). All resulting pathway-specific parameters are listed in Tables S1, S2, and 4, and the most common resulting short-term dynamics are depicted in Fig. 3D. To calibrate the mPSC frequencies for different pathways, we ran simulations with different values of the spontaneous release frequency for all synapses of a set of 1000 cells in a given pathway, and performed voltage-clamp recordings *in silico* to measure the resulting mPSC frequency at the soma (Fig. 3E1 left). We then fitted this data with a logarithmic function and interpolated the value of the spontaneous release frequency matching the *in vitro* reference value for the mPSC frequency (Fig. 3E1 right).

2.3.3 Validating synaptic physiology

We validated synaptic physiology against the amplitude and trial-to-trial variability of somatic potentials elicited by single presynaptic action potentials, as these measurements are dependent on most of the parameters of the synapse model (Ecker et al., 2020). As *in vitro* paired recording data is sparse, we used all available sources to determine synaptic parameters, and then used the same dataset to validate the process itself. Thus, the validation process resembles the calibration process. For any synaptic pathway we had *in vitro* reference values for, we randomly sampled 50 pairs of *in silico* neurons, clamped the postsynaptic cell, and measured the PSP at the soma of the postsynaptic cell in response to an action potential. This was repeated 35 times for every pair as in Ecker et al. (2020). Then, we extracted the mean and the CV of these amplitudes and compared them with reference data. Results of these PSP amplitude ($r = 0.99$, $n = 27$) and CV ($r = 0.63$, $n = 10$) validations are shown on Fig. 3B1 and C1, and listed in Supp. Tables S4 and S5 with the corresponding *in vitro* references. The frequency of the mPSCs was validated through measurements in *in silico* voltage-clamp experiments and comparison to the reference data ($r = 0.92$, $n = 5$, Fig. 3E2, Suppl. Table S6).

EPSP amplitudes of VPM evoked responses were also validated ($r = 0.97$, $n = 4$) in the same way for the four available pathways (Fig. 4B). To extend this validation, thalamocortical EPSP amplitudes were also compared with normalized EPSP amplitudes from Sermet et al. (2019) (Fig. 4D). However, it should be noted that this source reports normalized amplitudes in response to the activation of bundles of thalamic fibers. For example, the VPM to L6 PV+ pathway matches the data in terms of absolute amplitude (Fig. 4B), but appears too strong in terms of normalized amplitude, demonstrating the limitations of using this data for validation. Regardless, the results suggests that our POm to L5 E pathway might be too weak, as the rest of the POm to E and all the POm to PV+ interneuron pathways appear too strong relative to it (Fig. 4D2 right, first two columns). To improve this, additional data on that pathway is required (see Discussion).

2.4 Modeling the effect of missing extrinsic input

2.4.1 Datasets used for evaluation of *in vivo*-like dynamics

Activity in the model is compared with spike-sorted extracellular recordings from the barrel cortex of anaesthetised rats (Reyes-Puerta et al., 2015). The dataset contains single unit spike times for both spontaneous activity and responses to single whisker deflections,

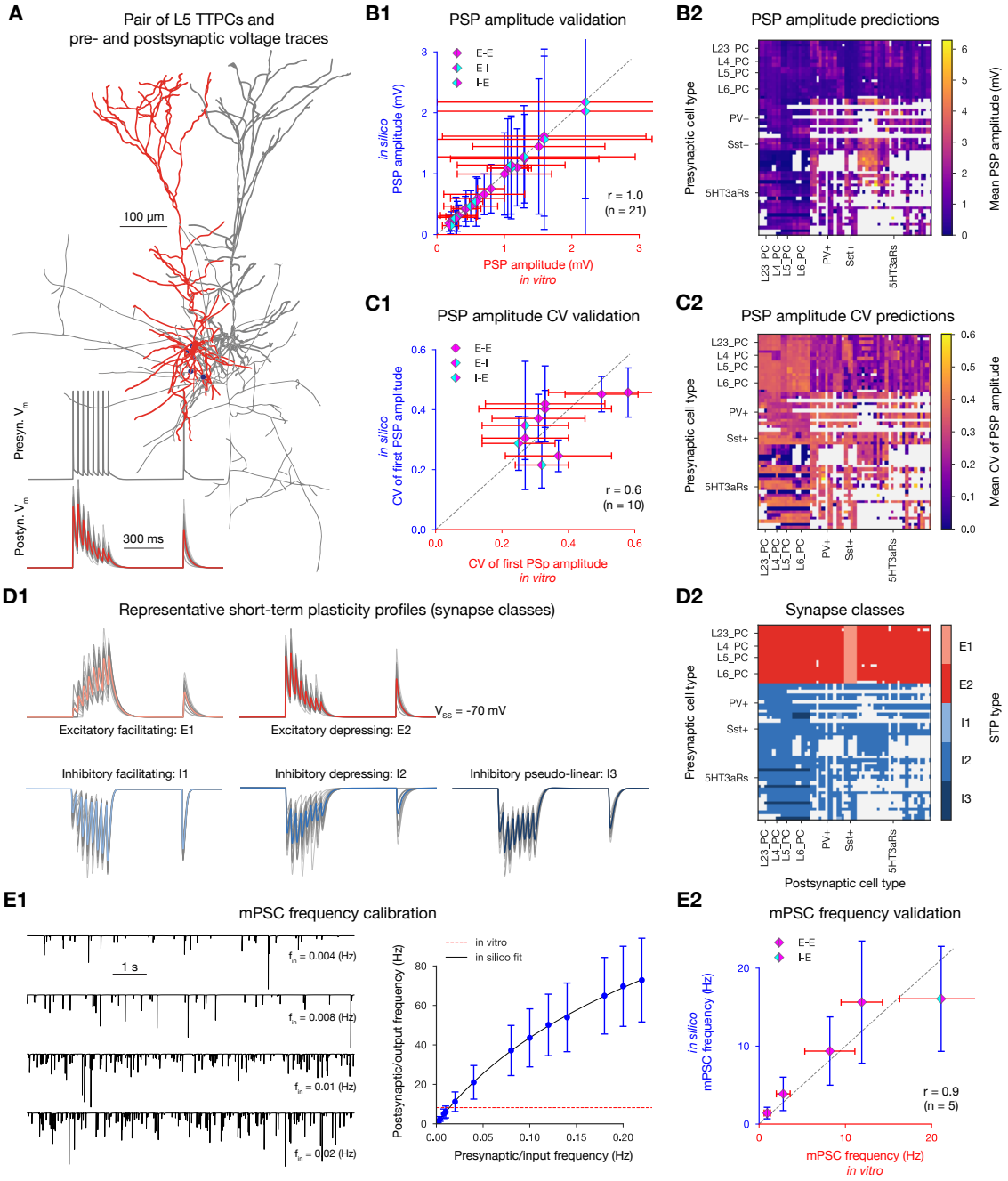

Figure 3: **Synaptic physiology.** **A:** Exemplary pair of L5 TTPCs (visualized with NeuroMorphoVis (Abdellah et al., 2018)). Presynaptic cell in gray, postsynaptic cell in red, synapses between them in purple. (Neurites are scaled for visibility, axon was cut to fit into the figure). Pre- and postsynaptic voltage traces below. **B1:** Validation of first PSP amplitudes (see also Table S4). Dashed gray line represents perfect correlation between experimental and model values. **B2:** Predicted PSP amplitudes of all viable pathways in the circuit. Pathways were considered viable if there were at least 10 connections in all 8 subregions of the model. Postsynaptic cells were held at -70 mV using an *in silico* voltage-clamp. Means were calculated over 100 pairs of neurons with 35 repetitions each. **C1** and **C2**: same as B1 and B2, but showing the CV of the first PSP amplitude, and corresponding Table S5. **D1:** Exemplary postsynaptic traces with different STP profiles. **D2:** Assignment of STP profiles to viable pathways. **E:** Calibration and validation of mPSC frequencies. E1: Calibration for L2/3 PCs. E2: Validation of all pathways (see also Table S6)

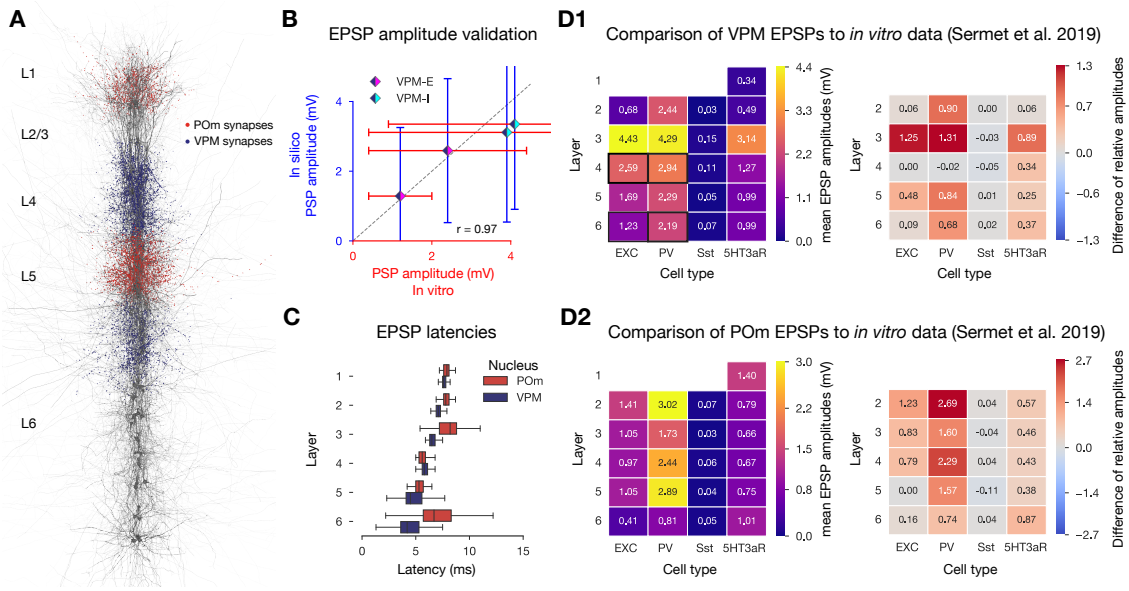

Figure 4: **Physiology of thalamocortical synapses A:** Location of synapses from VPM fibers (purple) and POm fibers (red) on 38 neurons (dark gray) in a 5 μm radius column (visualized with `BioExplorer`). **B:** Validation of EPSP amplitudes as in Fig. 3B1. The four pathways used for the validation are marked with a black rectangle on D1 to its right. **C**: EPSP latencies (time from presynaptic spike to the rise to 5% of peak EPSP amplitude in the postsynaptic trace). **D1** Left: mean VPM evoked EPSP amplitudes on postsynaptic cell types (over 50 pairs). Right: Comparison of normalized *in silico* amplitudes (normalized by L4 E as in Sermet et al. (2019)) to *in vitro* reference data from Sermet et al. (2019). Heatmap shows model minus reference values, thus positive values indicate a higher normalized EPSP amplitude in our model than in the reference experimental dataset. **D2**: same as D1 but for POm (normalized by L5 E as in Sermet et al. (2019)).

across 6 layer-wise neuron populations (L2/3 E, L2/3 I, L4 E, L4 I, L5 E & L5 I). We extend the dataset using the average of L2/3 I, L4 I and L5 I as a reference for L1 I and L6 I, and an alternative reference for L6 E (De Kock et al., 2007). The spontaneous firing rates of the 9 neuron populations are collected in the vector of reference firing rates, $\boldsymbol{V_{FR}}$.

As a secondary comparison, we use a dataset of *in vivo* juxtacellular and whole-cell recordings of barrel cortex responses in awake mice during an active whisker touch paradigm (Yu et al., 2019). While the animal model is different, using this data enables comparison to awake responses of layer-wise E populations and I subpopulations (VIP+ (vasoactive intestinal peptide, a subclass of our 5HT3aR+ population), Sst+, FS (fast spiking, corresponding to our PV+ population)). Moreover, this allows validating the model against properties of cortical responses across similar but different paradigms, reducing the risk of over fitting.

2.4.2 External input calibration

The initial calibration was made for a seven column subvolume (see Sec. 2.1, Fig. 5A1) containing 211,712 neurons. The total diameter of the simulated volume is approximately 1.5 mm. Each neuron receives a noisy conductance injection at the soma described by an Ornstein-Uhlenbeck (OU) process (similar to Destexhe et al. (2001), Fig. 5A2). The

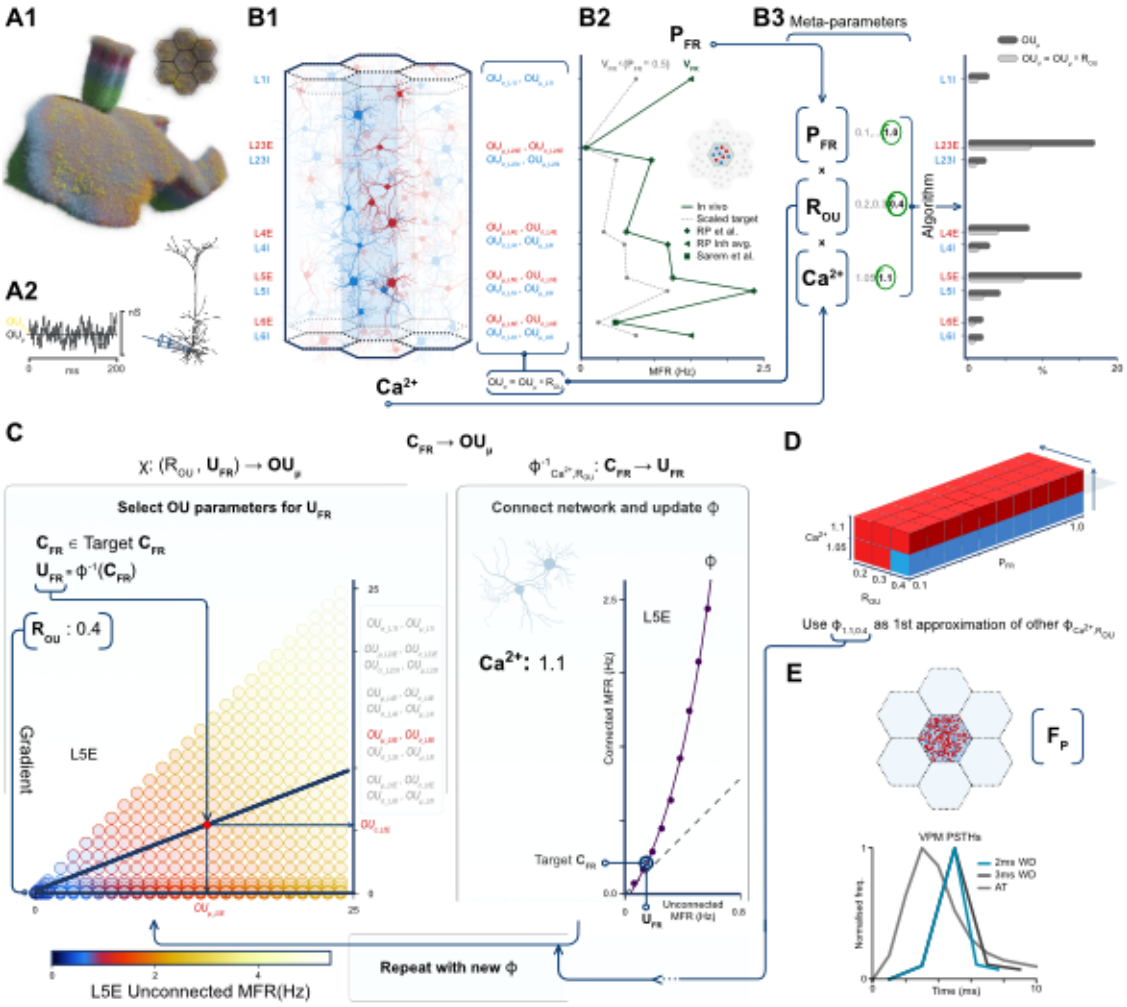

Figure 5: **Spontaneous and evoked activity calibration.** **A1:** Visualisation of full nbS1 model and a seven column subvolume (see Sec. 2.1) extracted from the S1FL region. Top view shows hexagons. **A2:** Illustration of OU-based noisy conductance injection at the soma. **B1:** OU parameters by population (layer and E/I-type). The calibration algorithm measures activity in the central column (30,190 neurons, blue shading) of the seven column subvolume. OU_σ is set to $OU_\mu * R_{OU}$ for all populations. **B2:** *In vivo* reference firing rates (dark green) and P_{FR} scaled firing rates (grey). **B3:** 3 meta-parameters ($[Ca^{2+}]_o$, R_{OU} and P_{FR}) and example values. **B4:** OU parameters generated by the algorithm to achieve P_{FR} scaled firing rates for an example set of meta-parameter values (circled green in B3). **C:** Left: Illustration of χ for L5 E. Firing rates from unconnected simulations of a single column. Simulations vary by OU_μ and OU_σ. Color shows firing rate. For a combination of R_{OU} and P_{FR}, interpolation over the simulation data points allows us to find OU_μ and OU_σ parameters which achieve the target unconnected firing rate. Right: Illustration of ϕ for L5 E. Exponential fit to unconnected vs. connected firing rates, used to estimate unconnected firing rates which will achieve target connected firing rates. **D:** Other $\phi_{Ca^{2+},R_{OU}}$ can be learned by using $\phi_{1.1,0.4}$ as a first approximation. **E:** Whisker stimuli were simulated by activating a percentage of VPM fibers (F_P) projecting to the central column. Lines show the 3 ms *in vivo* VPM whisker deflection PSTH and the *in vivo* active touch whisker deflection PSTH. The 2 ms whisker deflection PSTH was created by compressing the tail of the 3 ms whisker deflection PSTH by 66%.

mean (OU_μ) and standard deviation (OU_σ) of the process are defined as a percentage of an individual cell's input conductance at resting. OU_μ and OU_σ are parameterised separately for each population (combination of layer and E or I) (Fig. 5B1), leading to 18 parameters, grouped into two 9-dimensional vectors $\boldsymbol{OU_\mu}$ and $\boldsymbol{OU_\sigma}$.

The spontaneous firing rates across populations, denoted by the vector $\boldsymbol{C_{FR}}$, are determined by the vectors $\boldsymbol{OU_\mu}$ and $\boldsymbol{OU_\sigma}$, as well as the extracellular calcium concentration ($[Ca^{2+}]_o$) through its scaling of synaptic reliability, as in (Markram et al., 2015). The objective of the calibration procedure is to determine a mapping that outputs the 18 OU parameters required to achieve a particular set of firing rates $\boldsymbol{C_{FR}}$, for a given $[Ca^{2+}]_o$.

To do this efficiently, we impose two main restrictions: First, we restrict the coefficient of variation of the OU process ($\frac{OU_\sigma}{OU_\mu}$) to have the same value across populations, which we denote R_{OU} (Fig. 5B1). This reduces the dimensionality of the output parameter space for a given R_{OU} from 18 to 9 (as $\boldsymbol{OU_\sigma} = \boldsymbol{OU_\mu} * R_{OU}$). Second, we consider only compatible dynamic states, where the firing rates of the population groups are a proportion of reference *in vivo* firing rates, i.e. $\boldsymbol{C_{FR}} = P_{FR} * \boldsymbol{V_{FR}}$, with $P_{FR} \in [0, P_{max}]$ (Fig. 5B2), reducing the target $\boldsymbol{C_{FR}}$ values to a line in the space of possible $\boldsymbol{C_{FR}}$ values. The mapping must be determined for each value of $[Ca^{2+}]_o$ and R_{OU} separately (Fig. 5B3).

The calibration algorithm simplifies this task by splitting it into two separate parts: The first part creates a mapping, denoted χ, which allows us to find values of the 9 output parameters ($\boldsymbol{OU_\mu}$), which produce particular *unconnected firing rates* $\boldsymbol{U_{FR}}$ (i.e., where the neurons in the network are not connected to each other). The second part determines a mapping, denoted ϕ, between $\boldsymbol{U_{FR}}$ and the target $\boldsymbol{C_{FR}}$. In a recurrently connected network such as our model, the connected firing rate of a population depends on the firing rates of all other populations in complex and nonlinear ways. This is addressed by our restriction to compatible dynamic states, where by definition the firing rate of one population determines the firing rates of all others. Combining the two mappings allows us to find output parameters $\boldsymbol{OU_\mu}$ which produce particular connected firing rates $\boldsymbol{C_{FR}}$.

The first mapping, $\chi : (R_{OU}, \boldsymbol{U_{FR}}) \mapsto (\boldsymbol{OU_\mu}, \boldsymbol{OU_\sigma})$, is learned by running 1 second simulations over various combinations of OU_μ and OU_σ (Fig. 5C, left; Supp. Fig. S1). R_{OU} constrains OU_μ and OU_σ to a line of possible combinations in the 2D space. We generate an approximation of χ based on linear interpolation between the results of simulations along the line. Note in particular, that χ is independent of the extracellular calcium concentration.

Given the mapping χ, the remaining problem is to determine the values of $\boldsymbol{U_{FR}}$ that achieve certain target firing rates given by $P_{FR} * \boldsymbol{V_{FR}}$, for $P_{FR} \in [0, P_{max}]$ and each combination of $[Ca^{2+}]_o$ and R_{OU}, i.e., to determine the mapping ϕ as defined above. This is done by measuring values of $\boldsymbol{C_{FR}}$ produced for given values of $\boldsymbol{U_{FR}}$ in a number of simulations. However, instead of exploring the whole parameter space of possible $\boldsymbol{U_{FR}}$ values, we only explore a small number of values of $\boldsymbol{U_{FR}}$ which we expect to produce the target $\boldsymbol{C_{FR}}$ values. This is done by iteratively learning the mapping $\phi_{Ca^{2+},R_{OU}} : \boldsymbol{U_{FR}} \mapsto \boldsymbol{C_{FR}}$ and in each iteration using ϕ to predict $\boldsymbol{U_{FR}}$ values that bring the dynamics closer to the target firing rate, i.e. by sampling values given by $\boldsymbol{U_{FR}} = \phi^{-1}(C_{FR}) = \phi^{-1}(P_{FR} * \boldsymbol{V_{FR}})$ for 10 equidistant values of $P_{FR} \in [0, P_{max}]$. The initial guess of ϕ is simply the identity, i.e., assuming no effect of connecting the network, with $P_{max} = 0.5$. All other iterations

use $P_{max} = 1.0$. We update ϕ by fitting an exponential: $\boldsymbol{C_{FR}} = \alpha * e^{\beta \boldsymbol{U_{FR}}} + \kappa$ to the values of $\boldsymbol{U_{FR}}$, $\boldsymbol{C_{FR}}$ measured on the latest iteration (Fig. 5C, right).

We first approximated ϕ for $[Ca^{2+}]_o = 1.1\,\text{mM}$ and $R_{OU} = 0.4$. To reduce the number of iterations steps needed for other combinations of $[Ca^{2+}]_o$ and R_{OU}, we initialized the optimization process with the mapping ϕ obtained for this parameter pair instead of basing it on the identity (Fig. 5D).

2.4.3 Evoked activity comparison and validation

For the primary validation, stimulus-evoked responses were compared with *in vivo* responses to both *single whisker deflections* and *active whisker touches*. These stimuli were simulated in our model by activating a percentage (F_P) of the VPM fibers projecting to the central column of the simulated volume (Fig. 5E, upper). For each selected thalamic fiber, a single spike time was drawn from a probability distribution derived from an *in vivo* VPM PSTH (peristimulus time histogram).

First, *in silico* responses in the central column were compared to data on responses in the C2 barrel of the anaesthetized rat to single whisker deflections made at < 1Hz. Spike times were drawn from a PSTH of VPM responses to 3 ms mechanical single whisker deflections made at 1 Hz in urethane anesthetized rats (Diamond et al. (1992); Fig. 5E, lower). Since the *in vivo* data was from responses to 2 ms mechanical whisker deflections, we compressed the tail of the VPM PSTH to allow a direct comparison with the *in silico* responses Fig. 5F, lower). Second, network responses were compared with barrel cortex responses to active whisker touches in awake mice. A VPM PSTH for active whisker touch was used from the same dataset as the cortical responses (Yu et al., 2019). In both cases, the same thalamic stimulus was presented 10 times at 1 s intervals and at three stimulus intensities ($F_P : 5\%, 10\%, 15\%$). Together with $[Ca^{2+}]_o$, R_{OU} and P_{FR}, this resulted in a 4-dimensional parameter space. We then determined which parts of this space were compatible with data from the anesthetized or awake state.

Trial-averaged PSTHs were calculated for each parameter combination, both for all neurons, and for each of the layer-wise E and I populations. We then tested whether the latencies, 50% and 25%-decay points of the trial-averaged PSTHs were respectively no more than 10 ms, 10 ms and 40 ms later than those of the corresponding in vivo populations, and that there was no secondary rise in the PSTHs after the initial decay (by testing that none of the PSTHs for individual populations were more than 35% above baseline after 75 ms). L1 I was excluded from these tests, as it showed little or no response to the stimulus and we had no *in vivo* reference. These tests allowed us to split the 4D parameter space into two regions, one where *in silico* responses are consistent with *in vivo* responses, and another where they are not (see Results).

Simulations in the region of the parameter space with consistent responses were further compared to *in vivo* data, both to characterise network properties that were invariant over the parameter space, and to study how the 4 parameters affect network responses. For example, the order of layer-wise E, I and interneuron-type latencies were compared to *in vivo*, as well as the ratio between the evoked population response and the spontaneous baseline activity. This analysis also allowed us to select an *in vivo-like* working point for further experiments.

2.5 In-silico experimentation

Simulation of a morphologically detailed model first requires specifying the conditions (parameters and inputs) under which to perform the simulation. Given the correspondence between variables in the model and properties of biological systems, we are able to mimic to a certain extent the conditions and protocols of experimental studies. These are combinations of existing techniques, or even techniques that cannot or have not yet been performed experimentally. On top of the compensation for missing external input and different $[Ca^{2+}]_o$, we implemented further mechanisms to simulate specific experimental conditions. On a technical level, these comprise somatic current or conductance injections, adjustment of synaptic connectivity parameters, and selective activation of thalamic fibers. These are static conditions, however, in that their time course must be determined before the simulation is run. Somatic injections and connectivity adjustments can be targeted with single neuron or single pair resolution, respectively. To each thalamic fiber or neuron in the model, we can assign an arbitrary spike train, triggering synaptic release from all of its synapses with anatomically determined delays (from axonal conduction speed and path length). These mechanisms can target specific groups of neurons, e.g. based on neuron properties, such as location, layer, morphological or electrical type, or marker expression (determined based on morpho-electrical type as in Markram et al. (2015), Fig. 2B). We combined mechanisms to simulate various *in vitro* or *in vivo* experimental paradigms. Pathway lesions, for example, are simulated by selecting sets of pre- and postsynaptic neurons and removing all synaptic connections between them (Fig. S2A). Simulated optogenetic stimulation, in addition to being targeted at specific groups of neurons, took into account the attenuation of light with depth for the wavelength being used. Neurons were then inhibited or excited according to the intensity of light reaching them (Fig. S2B). Finally, sensory stimuli were simulated by generating instances of stimulus-specific stochastic spike trains activating the thalamic input fibers. For details on all these methods, see Supplementary Methods.

3 Results

3.1 Spontaneous activity calibration

We ran an algorithm to calibrate the parameters of the compensation of missing external synaptic input (see Methods), initially for a seven column subvolume (see Sec. 2.1), and later generalised to the full model. The subvolume contains 211,712 neurons and has a diameter of $\approx 1.5mm$ (Fig. 6A1). Each neuron has a time-varying conductance injected into the soma, described by a statistically independent Ornstein-Uhlenbeck (OU) process that mimics a barrage of random background synaptic inputs (Destexhe et al., 2001; Fig. 6A2). The mean (OU_μ) and standard deviation (OU_σ) of the injected conductances are specific for each layer-wise excitatory (E) and inhibitory (I) population, and they are scaled by a fixed, neuron specific scaling factor that accounts for neuron heterogeneity. A subspace of the parameter space resulting in *in vivo*-like spiking activity and described by three meta-parameters was identified (see Methods; Fig. 6B).

The first meta-parameter, R_{OU}, fixes the ratio between OU_σ and OU_μ across the different neuron populations, thus controlling the level of noise assumed to be present in the external synaptic input. The second meta-parameter specifies that the mean firing rate of each population should be a fixed proportion, $0 < P_{FR} \leq 1$, of its corresponding extracellularly measured spontaneous firing rate (Fig. 5B1). This is based on the insight that extracellular spike detection is likely to overestimate mean firing rates (Olshausen and Field, 2006; Wohrer et al., 2013), combined with the assumption that this bias affects all populations equally. Note, that other currently available experimental techniques to estimate mean firing rates have their own biases (see Discussion). Once accurate estimates of *in vivo* firing rates become available, we can use them in conjunction with $P_{FR} = 1$. The third meta-parameter, $[Ca^{2+}]_o$, scales the reliability and therefore the effective strength of synaptic transmission, and is explored within a narrow range of reported *in vivo* values ranging from 0.9 to 1.1 mM (Jones and Keep, 1988; Massimini and Amzica, 2001; Amzica et al., 2002; Gonzalez et al., 2022). Given a combination of $[Ca^{2+}]_o$ and R_{OU}, the goal of the algorithm was to find neuron population-specific OU_μ and OU_σ, such that the spontaneous firing rates defined by P_{FR} were realized in the model (Fig. 6C). Due to the non-linearity of the system, this required several iterations.

We began with $[Ca^{2+}]_o = 1.1$ mM and $R_{OU} = 0.4$, achieving after five iterations firing rates with low error for $P_{FR} = [0.1, 0.2, ..., 1.0]$ (50 simulations in total; Fig. 6D, left). The firing rates of the L2/3 I, and L4 I and L6 I populations could not be sufficiently lowered for $P_{FR} < 0.2$ and $P_{FR} < 0.1$ respectively, as they spontaneously fired even at their resting potentials (Supp. Fig. S1B). We continued with the remaining combinations of $R_{OU} = 0.2, 0.3, 0.4$, $[Ca^{2+}]_o = 1.05, 1.1$ mM. Using the mapping for $[Ca^{2+}]_o = 1.1$ mM and $R_{OU} = 0.4$ as a starting point reduced the required number of iterations to 3 with a total of 30 simulations per combination of $[Ca^{2+}]_o$ and R_{OU} (Fig. 6D2). Overall, OU parameters were found which satisfied 59 out of the 60 meta-parameter combinations with low error (Fig. 6E, F). The 60th parameter combination ($R_{OU} = 0.2$, $[Ca^{2+}]_o = 1.1$ mM and $P_{FR} = 1.0$) produced bursting activity uncharacteristic of *in vivo* activity, and so is excluded from the remaining analyses. In total, 200 simulations of 6.5 s biological time were run (Supp. Fig. S3); an average of 21.6 s of simulation time per meta-parameter combination.

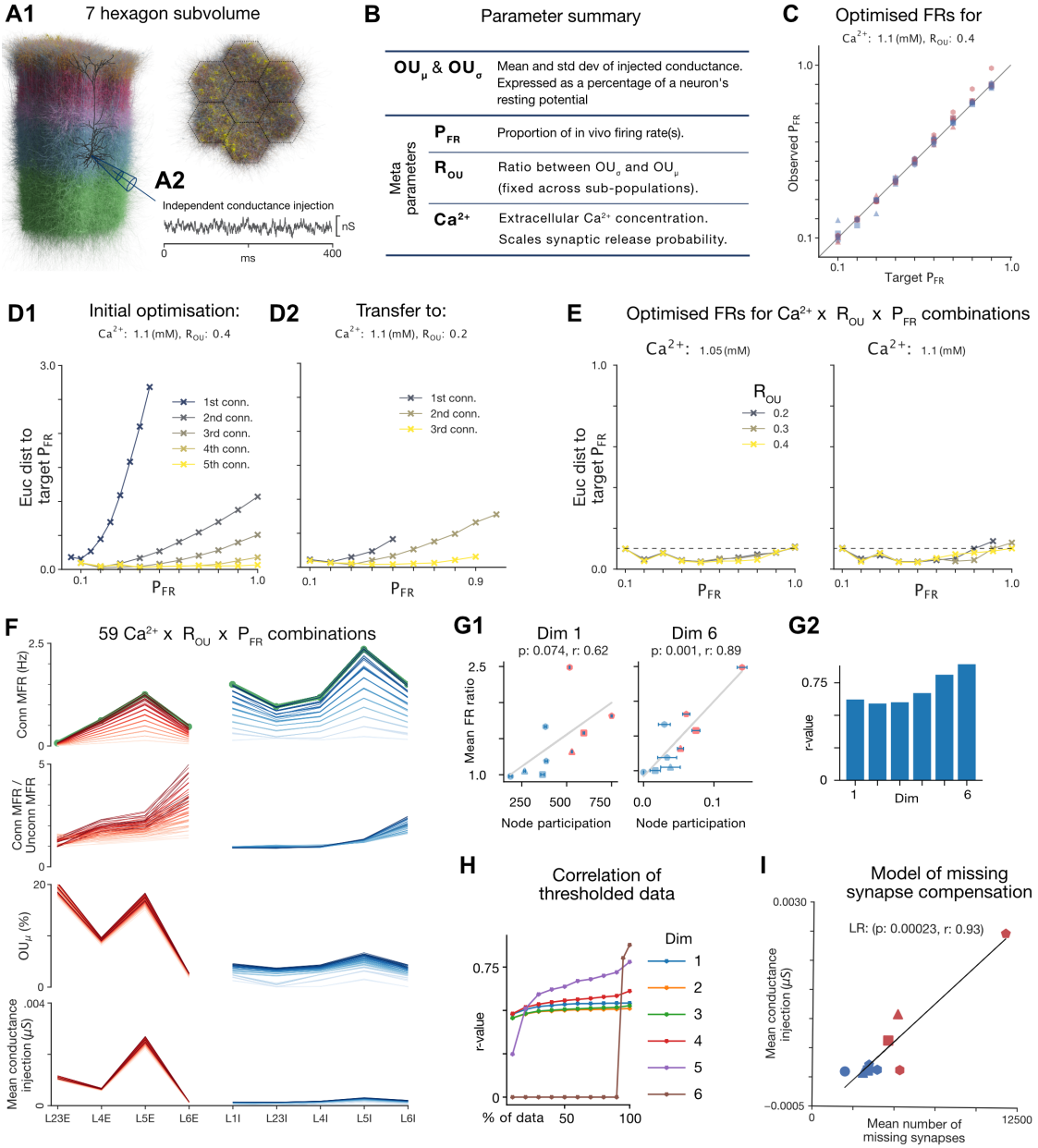

Figure 6: **Results of spontaneous activity calibration.** A1: Visualisation of a seven column subvolume and A2: somatic conductance injection. **B:** Table summarising the key parameters of the spontaneous calibration algorithm. **C:** For the 10 target P_{FR} values (0.1, ..., 1.0), the target connected P_{FR} (x-axis) is plotted against the observed P_{FR} (y-axis) for each neuron population after the 5 iterations of the calibration procedure for $[Ca^{2+}]_o = 1.1\,\text{mM}$ and $R_{OU} = 0.4$. E and I populations are shown in red and blue, respectively. The number of sides of the shape indicates the layer (triangle used for L2/3). **D1:** For the 10 target P_{FR} values (0.1, ..., 1.0), the Euclidean distance between the observed P_{FR} values and the target P_{FR} (over neuron populations) decreases over the 5 iterations for $[Ca^{2+}]_o = 1.1\,\text{mM}$ and $R_{OU} = 0.4$. **D2:** Same as D1 but for the three iterations for $[Ca^{2+}]_o = 1.1$ and $R_{OU} = 0.2$ when using the mapping found for $\phi_{1.1,0.4}$ as an initial starting point. **E:** Same measure as D1 and D2 for the final optimisation iterations of each combination of $[Ca^{2+}]_o$ and R_{OU}. The 5 combinations have a similar error to $[Ca^{2+}]_o = 1.1\,\text{mM}$ and $R_{OU} = 0.4$ despite using only 3 iterations rather than 5. The dashed line shows the error threshold for terminating the optimisation procedure. This was slightly relaxed for a small number of higher P_{FR} simulations.

F: (i) Firing rates, (ii) proportions between connected and unconnected firing rates, (iii) OU_μ and (iv) mean conductance injection by population for the final 59 non-bursting simulations. Each line represents a single simulation, although E and I values are separated. The darker the line (red or blue) the higher target P_{FR}. **G1:** The mean *node participation* of E and I populations in each layer for dimension one (left) and six (right) vs. the ratio between connected and unconnected firing rates for the parameter combination $[Ca^{2+}]_o = 1.05\,\text{mM}$, $R_{OU} = 0.4$ and $P_{FR} = 0.3$. Markers as in C. Line shows linear fit. **G2:** Correlation r-values for the data shown in G1 (for all dimensions 1-6). **H:** Correlation r-values for the correlation between mean node participation and the ratio between connected and unconnected firing rates (as in G) when neurons with highest node participation are not included in the calculation of mean node participation (via a sliding threshold). **I:** Mean missing number of synapses vs. the mean conductance injection, averaged over all combinations, for each population.

Each neuron population required a level of conductance injection within a small and specific range (Fig. 6F), demonstrating the need for efficient algorithmic determination of population-specific input compensation. The effect of local recurrent connectivity on firing rates increased from supra- to infragranular layers (Fig. 6F second from top), which correlated with a gradient in the topology of intra-layer synaptic connectivity: We calculated the mean *node participation* of neuron populations and in various dimensions (Fig. 6G1). For dimension one, this is simply the degree of a neuron; for dimensions above one, this generalizes the notion to counting participation in dense, directed motifs of increasing size (*directed simplices*; Reimann et al., 2017; see Supp. Methods). We found that correlations of this measure with the ratio of connected and unconnected firing rates increased with dimension (Fig. 6G2), indicating the importance of large directed simplices in shaping activity. The distributions of node participation were long-tailed (not shown) and the correlations were largely carried by a comparatively small number of neurons with high participation increasing the mean of a population. When neurons at the high end of the distribution were excluded, the strength of the correlation decreased, and this trend was stronger for the higher dimensions (Fig. 6H). This indicates that the structure of spiking correlations was largely determined by a small number of neurons in a topologically non-random connectivity core.

As it represents the effect of missing extrinsic input, the required strength of the conductance injection is expected to depend on the number of missing synapses. We estimated the number of missing synapses per neuron assuming a total density of E synapses of $1.1\,synapses/\mu m$, based on mean spine densities (Larkman, 1991; Datwani et al., 2002; Kawaguchi et al., 2006), and subtracting the number of synapses present in the model. We confirmed a strong correlation between the two measures (Fig. 6I).

3.2 Emerging spontaneous activity

Layer-wise E and I histograms of spontaneous activity for two exemplary meta-parameter combinations are shown in Fig. 7A. The two combinations have the same population firing rates ($P_{FR} = 0.9$) but different values of $[Ca^{2+}]_o$ and R_{OU}. The first simulation represents a regime in which the OU input compensation has a higher coefficient of variation ($R_{OU} = 0.4$) and lower synaptic transmission reliability ($[Ca^{2+}]_o = 1.05\,\text{mM}$) compared to the second ($R_{OU} = 0.2$, $[Ca^{2+}]_o = 1.1\,\text{mM}$). We found larger fluctuations in the second simulation that were correlated between E and I populations across layers.

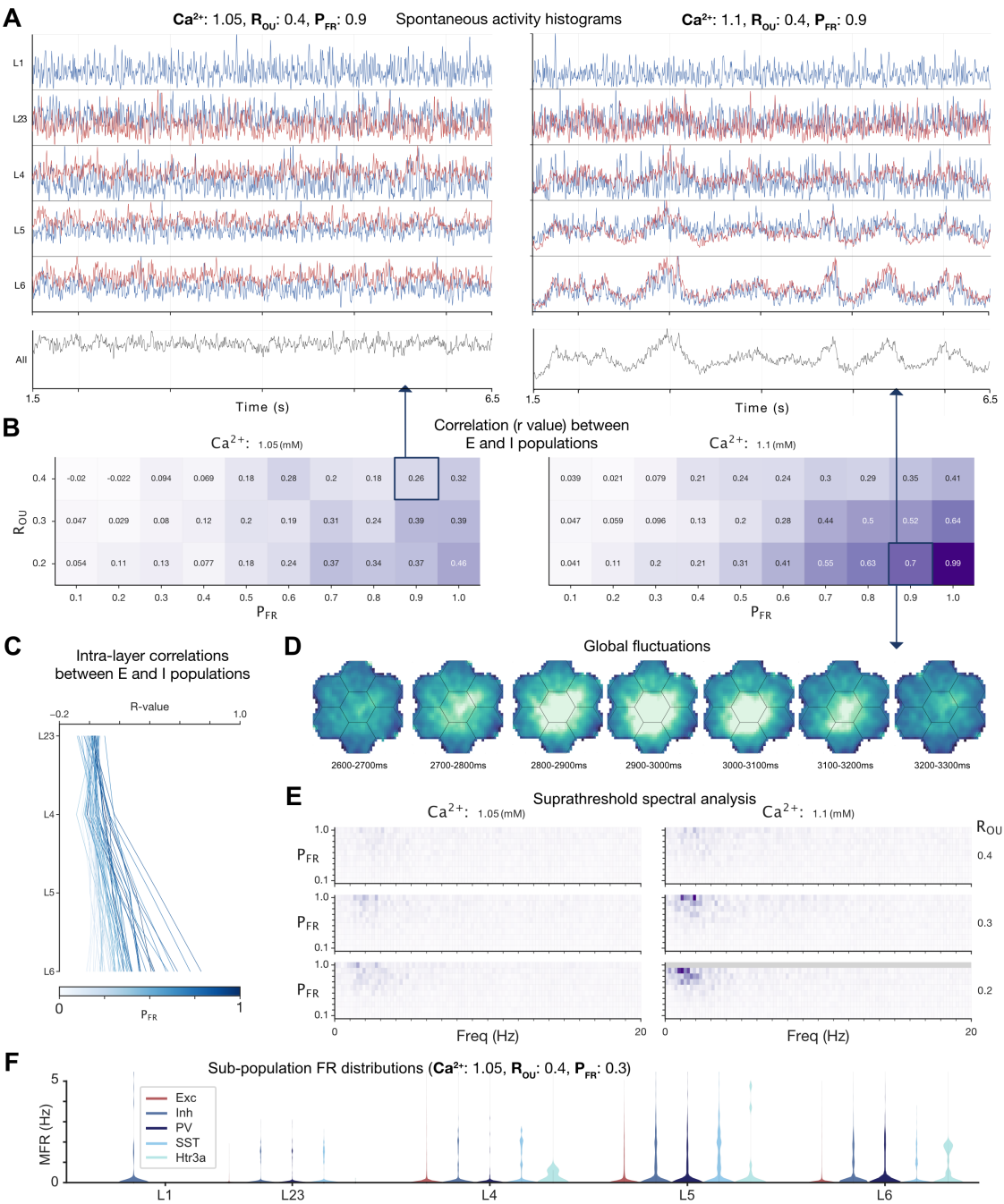

Figure 7: **Spontaneous activity results. A:** Max normalised histograms for two *in silico* parameter combinations (3 ms bin size, 1σ Gaussian smoothing:). **B:** Heatmap showing correlation r-value between the histograms (same bin size and smoothing as A) of the central column E and I populations. **C:** Correlation r-value between the histograms of layer-wise E and I populations for each of the 60 combinations. **D:** Activity for a single parameter combination in flat space over 7 consecutive 100 ms windows. Activity was smoothed using a Gaussian kernel ($\sigma = 1 pixel$). **E:** Fourier analysis of spontaneous activity for each of the 60 combinations. **F:** Firing rate distributions of different subpopulations for one of the parameter combinations. Plots were generated for 50 s of spiking activity.

Overall, increasing $[Ca^{2+}]_o$ and P_{FR}, and decreasing R_{OU}, increases the amplitude of correlated fluctuations of the network activity (Supp. Vid. 1; Fig. 7B). These result supports the notion that decreasing R_{OU} or increasing $[Ca^{2+}]_o$ shift the model along a spectrum from externally driven (and in this case, noise driven) to internally driven and therefore correlated activity. The shift is accompanied by an increase of power at the lower frequencies (Fig. 7E). In depth, the size of fluctuations and level of correlated activity increases from supragranular to infragranular layers (Fig. 7A, C; Supp. Vid. 1). This indicates that activity in deeper layers of the model is more internally driven, which is in line with the finding that in those layers the ratio of connected to unconnected firing rates is largest (Fig. 6F). In the horizontal dimensions, under higher correlation regimes, fluctuations are spatially coordinated and global within the central part of the model (Fig. 7D).

Finally, we confirmed that spontaneous firing rate distributions were long-tailed with peaks below 1 Hz for all of the meta-parameter combinations, in line with *in vivo* activity (Fig. 7F). When observed more closely, firing rate distributions did not appear smooth for some populations, with certain firing rates having higher probability (Supp. Fig. S3). This may indicate a lack of diversity in the neuron models used (anatomical or electrophysiological) or in the conductance injected across neurons in a population.

3.3 Stimulus-evoked responses

For the parameter combination $[Ca^{2+}]_o = 1.05\,\text{mM}$, $R_{OU} = 0.4$, $P_{FR} = 0.3$ and $F_P = 10\%$ we compared the temporal profile of specific neuron population responses to single whisker deflections (Reyes-Puerta et al., 2015) and active whisker touches to the literature (Yu et al., 2019). This was simulated by activating $F_P = 10\%$ of the thalamic fibers representing the inputs from VPM. While the model was of non-barrel somatosensory regions, and consequently lacked the anatomical distinction between barrels and septum, the test nevertheless provided validations of overall excitability and the laminar structure of responses that reflect general trends of cortical processing.

E and I populations in each layer show clear responses on each of the 10 trials of the test protocol (Fig. 8A1), except for L1, which has no clear response. Responses also remained localized to within 600 μm of the location of the stimulus (Fig. 8A2). Moreover, the trial-averaged PSTHs (baseline and max normalised) are similar to the *in vivo* responses (Fig. 8A3). As *in vivo*, the latencies (defined by the time point of the maximum response) of the I populations precede those of the corresponding E group in each layer. Minor discrepancies compared to the *in vivo* dataset include shorter and longer sustained responses of L2/3 E and L4 E, respectively, and a slower latency of L4 I.

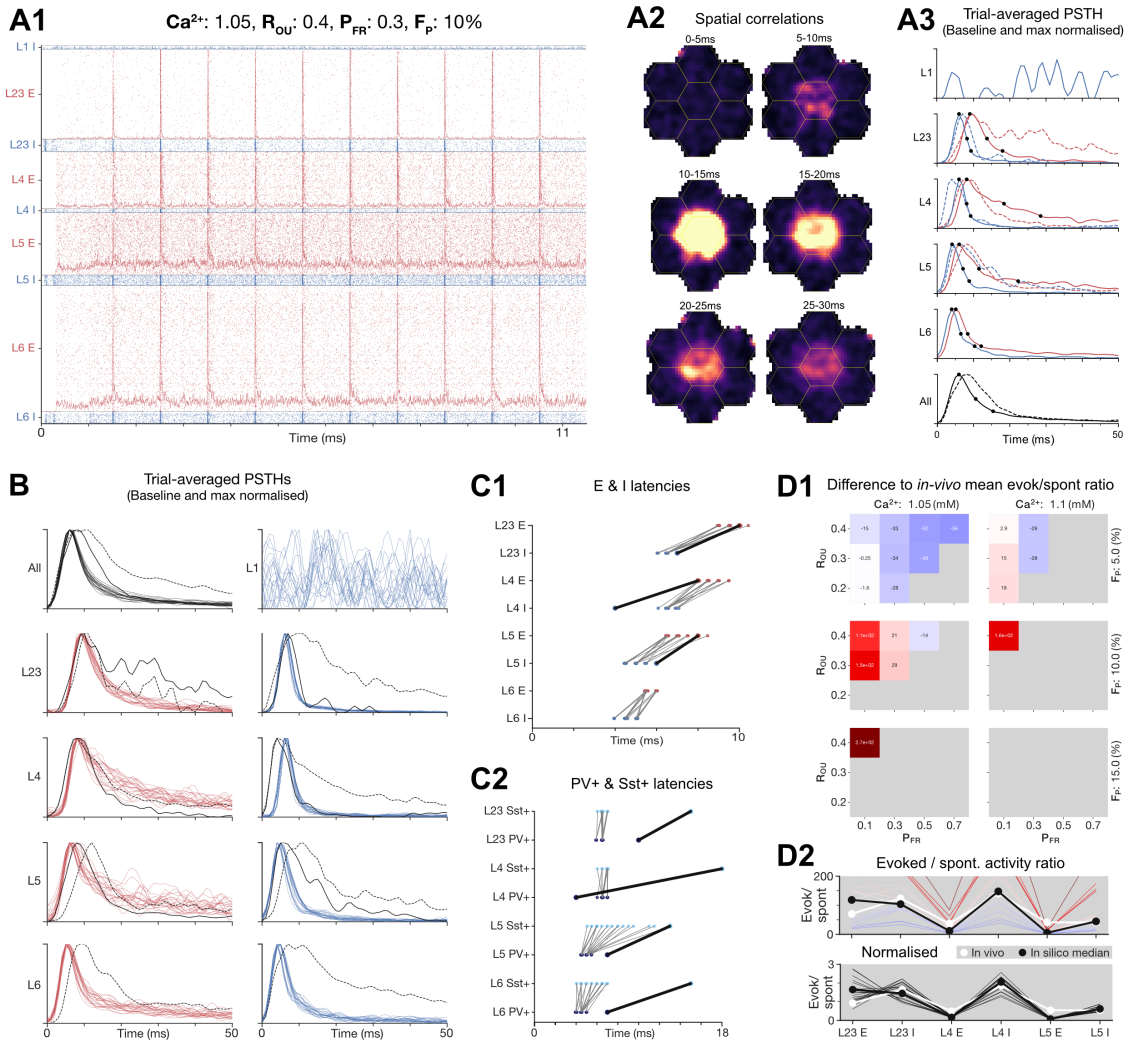

Figure 8: **Single whisker deflection results. A1:** Spiking activity and histograms (baseline and max normalised) for each layer-wise E and I population for the parameter combination $[Ca^{2+}]_o = 1.05\,\text{mM}$, $R_{OU} = 0.4$, $P_{FR} = 0.3$ and $F_P = 10\%$ over the course of the 10 whisker deflection test protocol. **A2:** Spatiotemporal evolution of the trial-averaged stimulus response in flat space. A3: Trial-averaged PSTHs (baseline and max normalised) for the entire population, and for each layer-wise E and I population for the same parameter combination (solid) and for the *in vivo* dataset (dashed). **B:** The trial-averaged PSTHs (baseline and max normalised) for all of the parameter combinations which passed the initial criteria. **C:** Latencies of different populations (C1) and inhibitory subpopulations (C2) for the criteria passing combinations. Black lines show the *in vivo* reference. **D1:** Heatmap with parameter combinations which failed the criteria tests masked out. For the *in vivo* dataset and each simulation, the mean of R_E over populations is calculated. The heatmap shows the *in vivo* mean subtracted from the *in silico* mean for each simulation. **D2:** Upper: R_E by population. One line per simulation. Simulation line colour shows heatmap metric. White shows *in vivo* values. Thick black line shows median of *in silico* values. Lower: Normalised ratios of each simulation (and the *in vivo* dataset) by dividing by the mean of the population ratio of the simulation.

The same trends were found for all other parameter combinations that passed the initial criteria for similarity to *in vivo* based on response latencies and decays (Fig. 8B; see Methods), indicating that this is a general property of the model. The remaining results and observations in this section apply to simulations with parameter combinations passing these criteria. As *in vivo*, the latencies of the layer-wise I populations are faster than the corresponding E population (Fig. 8C1). For L2/3 and L5 the difference between the E and I latencies are in fact the same as *in vivo*. In general, the latencies increase with distance from the bottom of L6 (i.e., with distance from the thalamus, Fig. 4C), except for the L4 I group *in vivo*. This exception is not matched by the *in silico* population, which is 2-3 ms slower, indicating room for improvement in further iterations (see Discussion).

PV+ and Sst+ subpopulations respond reliably in layers 2-6, but the 5HT3aR+ subpopulation responses are weaker and less reliable (Supp. Fig. S4). As responses were recorded extracellularly in (Reyes-Puerta et al., 2015), interneuron subtypes could not be further distinguished. Therefore, we compared their latencies instead to (Yu et al., 2019), who used intracellular recordings in an active whisker touch paradigm. This makes a direct, quantitative comparison difficult. Nevertheless, it can be noted that PV+ latencies precede Sst+ latencies *in vivo*, and either precede or are simultaneous with Sst+ latencies for almost all of the simulations (Fig. 8D2).

Simulations that did not pass the criteria for similarity to *in vivo* were characterized by overly sustained, bursting, or secondary rebound responses over the whole circuit or in certain populations (Fig. S4). The simulations not passing the criteria were restricted to a contiguous part of the parameter space (Fig. 8C1), characterized by combinations of high P_{FR}, $[Ca^{2+}]_o$ and F_P with lower R_{OU}. Notably, *in vivo*-like responses are supported at lower FRs (i.e., lower values of P_{FR}) with weakly correlated spontaneous activity (compare Fig. 8C1 with Fig. 6C3), offering a prediction that true *in vivo* firing rates are within the range of these lower FRs.

So far, we considered the latency of population responses. We characterized the magnitude of responses by R_E, the ratio between the peak of the evoked response and the pre-stimulus baseline activity level. Assuming that extracellular sampling biases are similar during spontaneous and evoked activity, R_E factors out the effect of extracellular sampling bias, providing a bias-free metric for comparing response magnitude with *in vivo*. Nonetheless, it is possible that there are differences between the biases during the evoked and spontaneous periods.

We found that decreasing R_{OU} and P_{FR}, and increasing $[Ca^{2+}]_o$ and F_P led to a global increase of R_E, and that for a large part of the parameter space results matched the *in vivo* data closely (Fig. 8D2 top). Interestingly, the median *in silico* ratios (black) are similar to the *in vivo* ratios. Also, the parameter combination closest to *in vivo* was central in the space of simulations that passed the criteria for *in vivo*-like latencies and decays. This consistency between latency-based and amplitude-based quality metrics further validates the *in vivo*-like region of the parameter space.

When normalizing with respect to the response magnitude of the entire population, the subpopulation ratios are remarkably constant, indicating that variation of the parameters provides a global scaling of excitability. Overall, the ratios of the layer-wise I populations are similar to *in vivo* over all parameter combinations (Fig. 8D2 bottom),

while the responses of L23 E, and L4 E and L5 E, are slightly greater and weaker, respectively, than the corresponding *in vivo* data.

The responses of the layer-wise E and I populations to the active whisker touch stimulus were similar to the *in vivo* active whisker touch responses in the same region of the 4D parameter space where responses were similar to single whisker deflections (Supp. Fig. S5), providing a strong validation of the model. The latencies of the populations were also similar to *in vivo*, with the main discrepancy being slower responses relative to *in vivo* in L4 (E and I). With respect to the meta-parameters, we found that the anesthetized state was characterized by lower firing rates (P_{FR}) and reduced external noise levels (lower R_{OU}) compared to the awake active whisker touch paradigm. This is based on identifying areas with low absolute ratio differences (indicated white in Figs. 8D1 and S5B). These results fit with what might be expected under anaesthetized and awake states respectively, and provide predictions of the spontaneous firing rates, noise levels and corresponding *in silico* regimes for the two *in vivo* states.

In summary, the latencies of the layer-wise E/I populations are similar to *in vivo* both for the single whisker deflections and active whisker touches, with several subtle differences on the order of 1-3 ms. Future model refinement (i.e., integration of additional data sources) may improve the similarity to *in vivo*. The results highlight a region of the parameter space in which both spontaneous and evoked activity are consistent with the spontaneous and evoked *in vivo* datasets. For the remaining experiments, we use either of the two parameter combinations $[Ca^{2+}]_o = 1.05\,\text{mM}$, $R_{OU} = 0.4$ and $P_{FR} = 0.3$ or 0.5, as these combinations support realistic *in vivo*-like responses to the two stimulus types over a range of fiber percentages (F_P).

3.4 In-silico experimentation

Building upon the *in vivo*-like activity states, we combined various simulation techniques to recreate laboratory experiments from the literature (see Methods).

3.4.1 L4's contribution to L2/3 responses during whisker hold stimulus

In the canonical model of the cortex (reviewed e.g., in Lübke and Feldmeyer, 2007; Feldmeyer, 2012) information from the thalamus arrives to L4, then propagates to L2/3, from there to L5 (which serves as the main cortico-cortical output layer) and lastly to L6 (which projects back to the thalamus). The coordinated action of all layers of S1 is required for high-level behavioral tasks (Park et al., 2020). As the canonical model is based on the highest layer-wise density of axons, it cannot describe all interactions in the cortex. For example VPM does not only innervate L4, but also the border of L5 and L6, as well as the bottom of L2/3 (Meyer et al., 2010; Constantinople and Bruno, 2013; Sermet et al., 2019).

To study how L4 contributes to the stimulus preference of L2/3 PCs, Varani et al. (2022) used optogenetic inactivation of L4 PCs during whisker stimulation and quantified the changes in the subthreshold response of L2/3 PCs. They found, that the early phase of the subthreshold response significantly differed from the control condition, if the whisker was deflected in either the most or the least preferred direction (see the top and bottom rows of their Fig. 5B-C). From this they concluded that both L4 and VPM contribute to the direction tuning of L2/3 PCs. After reproducing their experimental conditions *in*

silico (Fig. 9A-D; see Supp. Methods) we confirmed that we can reproduce their results, i.e., subthreshold responses of L2/3 PCs decreased, when L4 PCs were inhibited (Fig. 9E, for preferred direction whisker deflections).

We then leveraged our *in silico* setup to study what Varani et al. (2022) could not, because of methodological limitations. The authors aimed to test how direct E connections from L4 PCs to L2/3 PCs influence the stimulus representation in L2/3. This connection can not specifically be blocked *in vivo*, however, instead only 95% of the L4 PC population are inhibited (as well as some lower L3 PCs). In our setup we could selectively block the connection and found almost the same result (Fig. 9E, F). This extends the conclusion of Varani et al. (2022): L4 PCs contribute to the stimulus preference of L2/3 PCs via direct excitatory connections, and not via disynaptic inhibition.

The authors also discussed studying L5 PCs contribution to the L2/3 responses (as a large fraction of L5 PC axons terminate in L2/3), but this is infeasible with current mouse lines. Leveraging our model, we found that L5 contributes much less to subthreshold L2/3 traces than L4 (Fig. 9F right). Extending to other presynaptic layers, we found that the contribution of L2/3 is similar to that of L4, whereas inputs from L6 are negligible (Fig. 9F right). Whilst there might be mouse lines targeting L5 PCs in the near future (which could validate our predicitons), blocking L2/3 connections between L2/3 cells without hyperpolarizing the same L2/3 population seems to be achievable only *in silico*.

3.4.2 Contrast tuning modulation by optogenetic activation of interneuron subtypes

Shapiro et al. (2022) compared the modulatory effects of optogenetic activation of interneuron subtypes on contrast tuning of neurons in V1. Whilst visual regions differ from somatosensory regions, the study provided an opportunity to explore the generality of interactions between inhibitory and excitatory cortical populations. We therefore created a version of the study *in silico*, presenting drifting grating patterns with various contrast levels through the VPM inputs (Fig. 10A; see Supp. Methods) in an *in vivo*-like state ($[Ca^{2+}]_o = 1.05\,\text{mM}$, $R_{OU} = 0.4$, and $P_{FR} = 0.3$).

Mirroring the analyses of Shapiro et al. (2022), we first identified a population of neurons based on their contrast tuning. Specifically, we considered neurons with robust, monotonically increasing tuning behavior (see Supp. Methods). Overall, we found 228 PCs and 259 PV+ interneurons with robust tuning within a single simulated column. Within a central cylinder with a radius of $50\,\mu m$, i.e. within spike detection range of a vertically penetrating extracellular electrode (Henze et al., 2000; Buzsáki, 2004), we found 15 PCs and 13 PV+ interneurons with robust tuning, which is roughly comparable to the average number of tuned cells per mouse of 8.2 PCs and 3.0 PV+ neurons respectively in Shapiro et al. (2022). Unlike the original study we found no Sst+ neurons with robust tuning.

As in the original study, the firing rates of both PCs and PV+ neurons were affected by optogenetic activation of the PV+ subpopulation (Fig. 10C), resulting in changes to the contrast tuning curves of these populations (Fig. 10D). The main effect of the optogenetic manipulation was an increase in contrast tuning for PV+ and a decrease for PCs. As in (Shapiro et al., 2022), the tuning curves could be accurately fit by sigmoidal functions

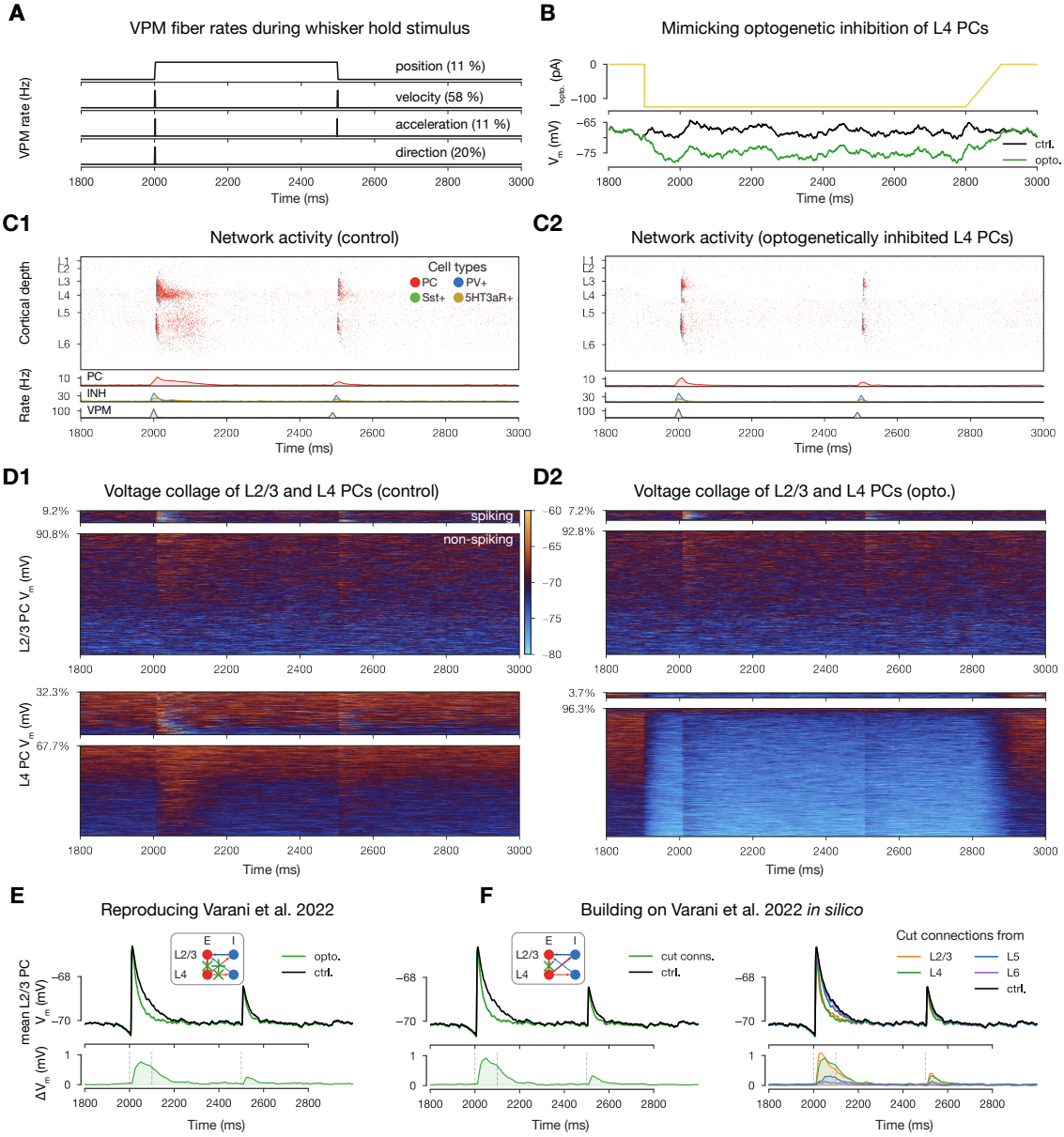

Figure 9: **Reproducing the experiments of Varani et al. (2022). A:** Schematics of whisker kinetics and VPM fiber rates during 500 ms long whisker hold stimulus. Fraction of VPM fibers coding for that kinetic feature are taken from Petersen et al. (2008). **B:** Mimicking the effect of the activation of an inhibitory opsin (Halo) *in silico*. Injected somatic hyperpolarizing current (mimicking opsin activation) at the top, and the resulting somatic voltage trace (from a combination of injected conductance, current, and synaptic PSPs from the network) at the bottom. **C:** Raster plots of the microcircuit's activity and population firing rates below. **C1**: Control conditions, **C2**: 95% of L4 PCs inhibited (by direct somatic current injection depicted in B above, see Supp. Methods). **D**: Voltage traces of all L2/3 (top) and all L4 (bottom) PCs. Within the individual panels spiking traces are at the top, while subthreshold ones at the bottom. **D1** and **D2** depict the same conditions as C above. E: Comparison of average traces from selected L2/3 PCs (see Supp. Methods) in control (black) and optogenetically inhibited (green) conditions. **F:** Same as E, but instead of mimicking the optogenetic inhibition of L4 PCs, only their connections to L2/3 PCs are "cut" (compare inset with the one in E). The right part depicts connections systematically cut from PCs in all layers, while the one on the left shows L4 only for a better visual comparison with the conditions of Varani et al. (2022) in E to its left.

($r^2_{PV+} = 0.995 \pm 0.008$; $r^2_{PC} = 0.990 \pm 0.012$), and consequently the effect of optogenetic activation could be quantified in terms of changes to the fitted parameters (Fig. 10D1 inset, E). Consistent with the findings by Shapiro et al. (2022), we found great variability between neurons with increasing trends for m in PV+ and c_{50} in PCs, and decreasing trends for R_{max} in PV+ and both m and R_{max} in PCs. Unlike in (Shapiro et al., 2022), we found in addition an increasing trend of c_{50} also in PV+ interneurons.

Shapiro et al. (2022) explored three mathematical models (see Supp. Methods) describing the effect of the optogenetic manipulation on the sigmoidal curve for PV+ neurons. As in that study, we found that the saturation additive model provided the best fit to the data (Fig. S8A, B1). The mathematical model combined an additive term with saturation at high contrasts; the relative contributions of both effects varied strongly between individual neurons (Fig. S8C1). At low intensities of the optogenetic manipulation, this distribution matched qualitatively the results of Shapiro et al. (2022), but at higher intensities we observed a shift towards stronger saturation.

The original study described the effect of the optogenetic manipulation on PCs by combining the saturation additive model for the PV+ subpopulation with a simplified model of PCs receiving inhibitory conductances proportional to the PV+ firing rate. Once again, we found that the simplified model provided a good description of the observations (Fig. S8B2). The relative contributions of saturation and addition in this model qualitatively matched the original study, although their absolute strengths are weaker (Fig. S8C2).

3.4.3 Tuning of I subtypes to synchronous and rate-coded signals

We also compared the *in vivo* state of our model with the results of a recent *in vitro* study (Prince et al., 2021), which explored how different interneuron subtypes represent signals that are encoded as changes in the firing rate or synchronicity of PCs (Fig. 11A; see Supp. Methods). While in the original *in vitro* study stimulation of 10 PCs was sufficient to find a decodable signal, we expected a larger number to be required under our *in vivo*-like conditions, due to the lower synaptic reliability at the lower $[Ca^{2+}]_o$, and the higher level of noise. Indeed, we found little discernible mutual information in interneuron spiking for the activation of 10 PCs that increased with the number of activated neurons (Fig. 11C, D right). For 1000 activated neurons each of the 3 interneuron subpopulations in L2/3 showed clear but qualitatively unique modulation for both encoding schemes (Fig. 11B). As in (Prince et al., 2021) we found differences in the encoding capabilities of the inhibitory subpopulations (Fig. 11C, D). The authors of the original study pointed out the importance of membrane properties and short-term dynamics of synaptic inputs onto the subpopulations in shaping the results. Note, that the lower synaptic reliability *in vivo* weakens synaptic depression (Borst, 2010), and the ongoing background input leads to higher membrane conductance (Destexhe et al., 2001), therefore our results are expected to differ substantially, and provide an independent prediction for a different dynamic state that the authors themselves suggested to investigate. We found strongest encoding in PV+ neurons for both schemes, and overall low encoding strength in Sst+ neurons. Further, we found overall low amounts of mutual information for the synchronous stimulus, which is in line with Prince et al. (2021), as they linked encoding of that stimulus to depressing synaptic dynamics, which would be weakened *in vivo*.

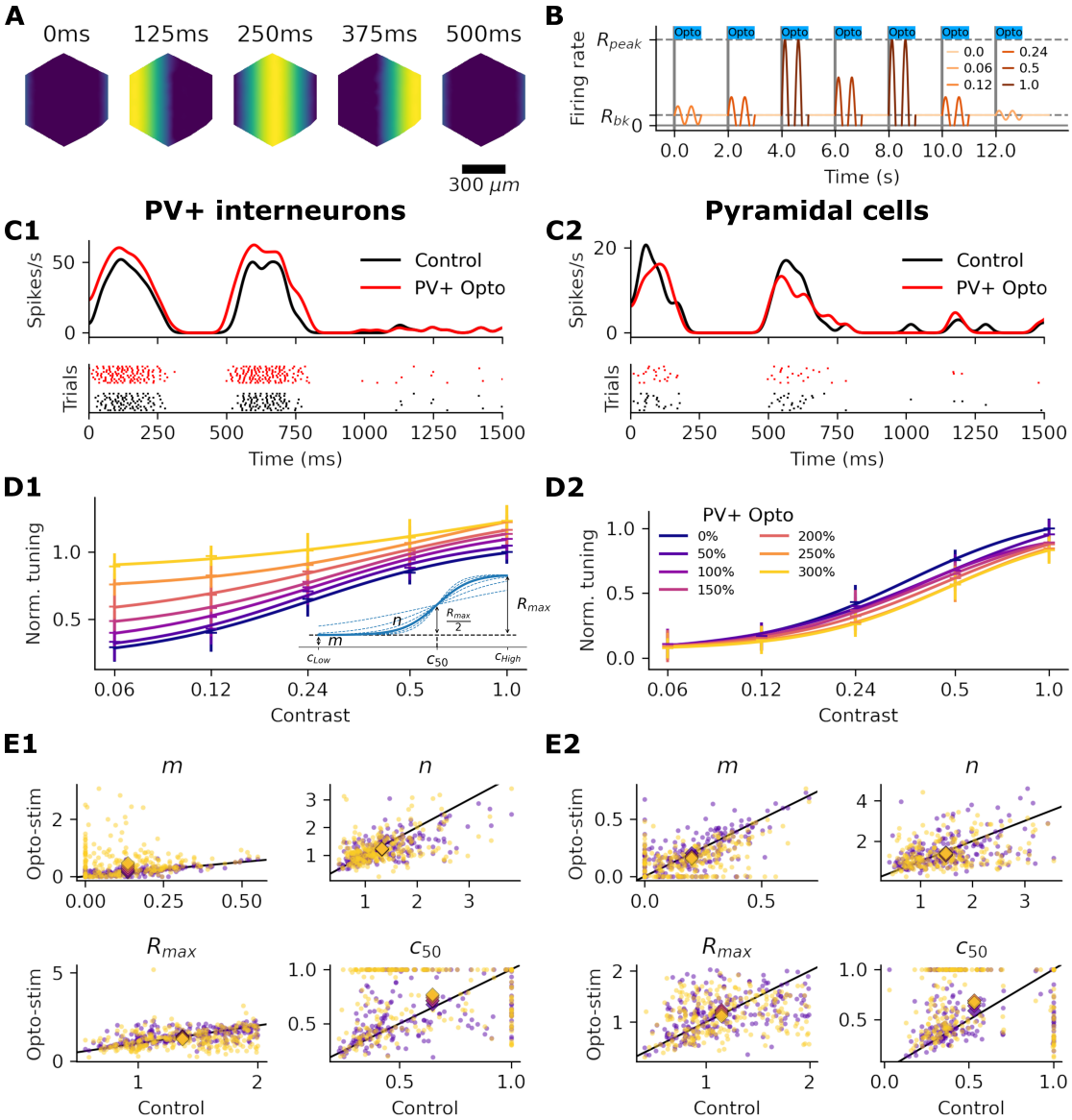

Figure 10: **Contrast tuning modulation by optogenetic activation of PV+ interneurons. A:** Spatial distribution of firing rates of VPM fibers projecting to a single simulated column at different points in time, corresponding to linear drifting gratings with a temporal frequency of $f_{temp} = 2\,\text{Hz}$ and a spatial frequency of $f_{spat} = 0.001\,\text{cycles}/\mu\text{m}$. **B:** Firing rate signal of a single VPM fiber corresponding to a random sequence of drifting grating patterns with different contrast levels C, as indicated by the legend. All optogenetic stimuli targeting PV+ (or Sst+) interneurons were completely overlapping with the grating stimulus intervals, as indicated by the blue bars. **C1:** Spiking activity and PSTH of an exemplary PV+ interneuron over 10 repetitions (trials) in response to a grating stimulus at maximum contrast ($C = 1.0$) without (black) and with (red) medium strength (150%) optogenetic stimululation. **D1:** Contrast tuning modulation of an exemplary PV+ interneuron by different levels of PV+ optogenetic stimulation, ranging from 0% (baseline) to 300%. The individual markers denote actual data points (mean ± SD over 10 repetitions, normalized to baseline response at maximum contrast) while solid lines illustrate sigmoidal fits to these data points. Inset: Illustration of sigmoidal parameters m, n, R_{max}, and c_{50}. **E1:** Scatter plots showing the fitted sigmoidal parameter values in control condition vs. PV+ optogenetic stimulation at lowest (50%) and highest (300%) level respectively for all 259 robustly tuned PV+ interneurons. Diamond markers indicate mean values over neurons, including all optogenetic stimulation levels from 50% to 300%. Colors as in panel D2 legend. **C2/D2:** Same as C1/D1, but for exemplary PCs. **E2:** Same as E1, but for all 228 robustly tuned PCs.

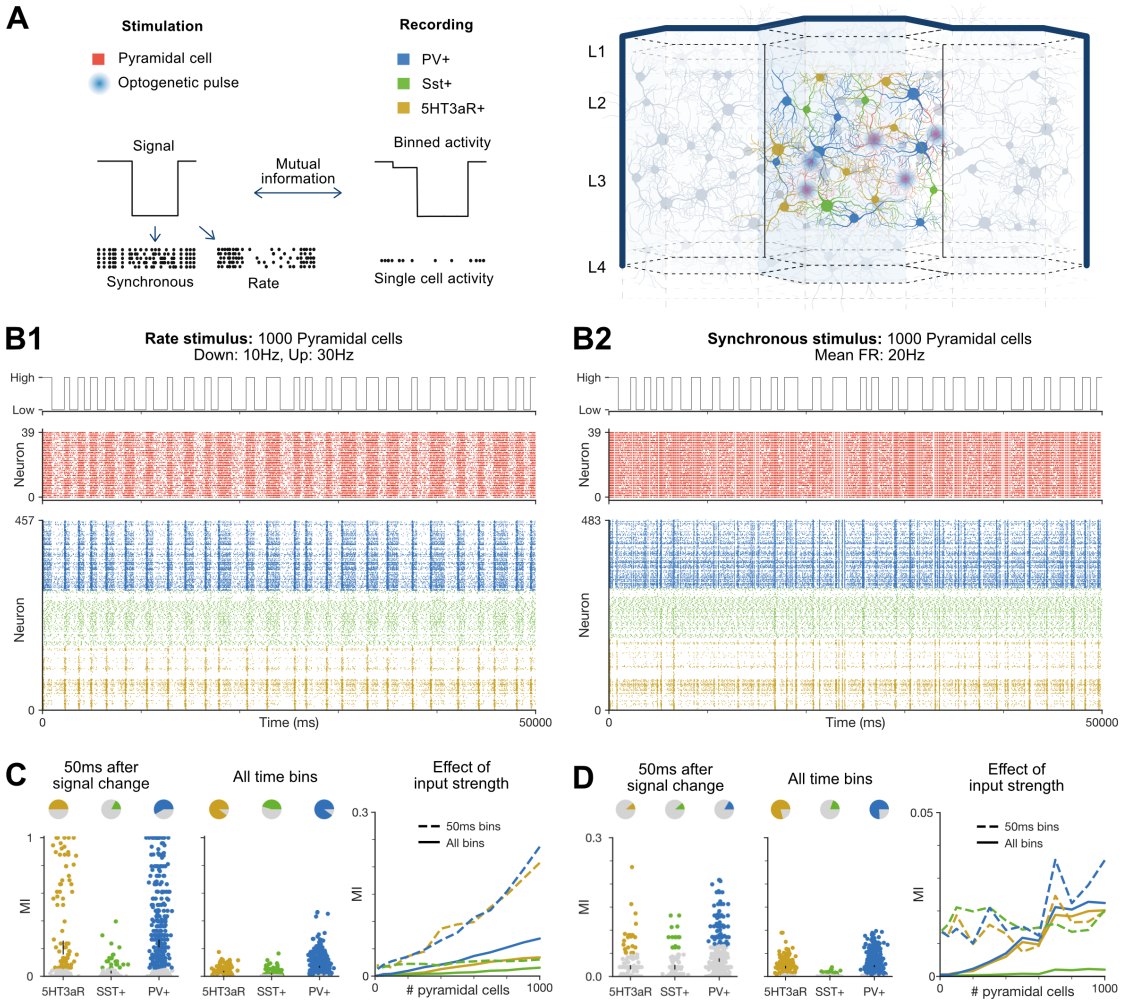

Figure 11: **Synchronous and rate encoding by interneuron subtypes.** **A:** Illustration of experimental paradigm. A binary signal is encoded either through changes in the rate or synchronicity of optogenetic pulses applied to a set of PCs. We define a direct correspondence between single optogenetic pulses and single spikes. Spiking activity is measured in PV+, Sst+ and 5HT3aR+ cells, and the mutual information between the binned activity of individual cells and the original binary signal is measured. **B:** Visualization of the rate (B1) and synchronous (B2) coded stimulus experiments stimulating 1000 PCs, showing the binary signal (top), input neuron spike trains for 40 neurons (middle), and responses of the 3 L2/3 neuron types. **C:** Results for the rate coded stimulus experiment in B1. Left: Mutual information between spiking activity and the binary signal (one point for each cell that spiked at least once). Only activity in the 50 ms following the change of the binary signal is considered. Cells with mutual information not significantly different from that of a shuffled control are coloured grey. Centre: Same as left but considering all time bins. Right: The effect of the number of stimulus neurons on the mean single cell mutual information for each subpopulation. **D:** The same as C but for the synchronous stimulus type.

3.5 Independent functional units emerging at larger spatial scales

After calibrating the model of extrinsic synaptic input for a seven column subvolume, we tested to what degree the calibration generalizes to the entire nbS1. Notably, this included addition of long-range connectivity (Reimann et al., 2022a). The total number of local and long-range synapses in the model was 9138 million and 4075 million, i.e., on average full model simulations increased the number of intrinsic synapses onto a neuron by 45%. Particularly, the final $\phi_{1.05,0.4}$ calibrated for the seven column subvolume was used in conjunction with $P_{FR} \in [0.1, 0.15, ..., 0.3]$. Each of the full nbS1 simulations (using $[Ca^{2+}]_o = 1.05\,\text{mM}$ and $R_{OU} = 0.4$) produced stable non-bursting activity, except for the simulation for $P_{FR} = 0.3$, which produced network-wide bursting activity.

Activity levels in the simulations of spontaneous activity were heterogeneous, ranging from a mean firing rate of 0.15 Hz to 0.3 Hz (when activity was averaged in flatspace; Fig. 12A1). The subregion with consistently higher firing rates was the upper lip representation (S1ULp), separated from the sub-regions of lower activity by the dysgranular zones (S1DZ, S1DZO). This demonstrates that the larger spatial scale of the model supports several independently acting functional units. Locations with higher firing rates were accompanied by higher spiking correlations of the local population (Fig. 12A2), indicating activity that was more driven by intrinsic excitation. Unlike in the simulations of smaller volumes, the correlation emerged mostly as a result of short, transient packets of activity in layer 6 (Fig. 12B, C). Consequently, deviation from the target P_{FR} in those cases was largest in L6 (Fig. 12D). Taken together, it appears as if the additional synapses from long-range connectivity moved the model along the spectrum from extrinsically vs. intrinsically driven, but further for some regions than for others. We confirmed a divergence into two populations: one with correlation slightly increased from the simulations of smaller volumes, and one with almost maximal correlations (Fig. 12E). This distinction was determined mostly in layer 6 with increases of correlations in other layers remaining small.

We repeated the previous single whisker deflection evoked activity experiment in the full model, providing a synchronous thalamic input into the forelimb sub-region (S1FL; Fig. 12F,G). Responses in S1FL were remarkably similar to the smaller simulations, including the delays and decays of activity (Fig. 12F). However, in addition to a localized primary response in S1FL within $350\,\mu m$ of the stimulus, we found several secondary responses at distal locations (Fig. 12G), which was suggestive of selective propagation of the stimulus-evoked signal to downstream areas efferently connected by long-range connectivity.

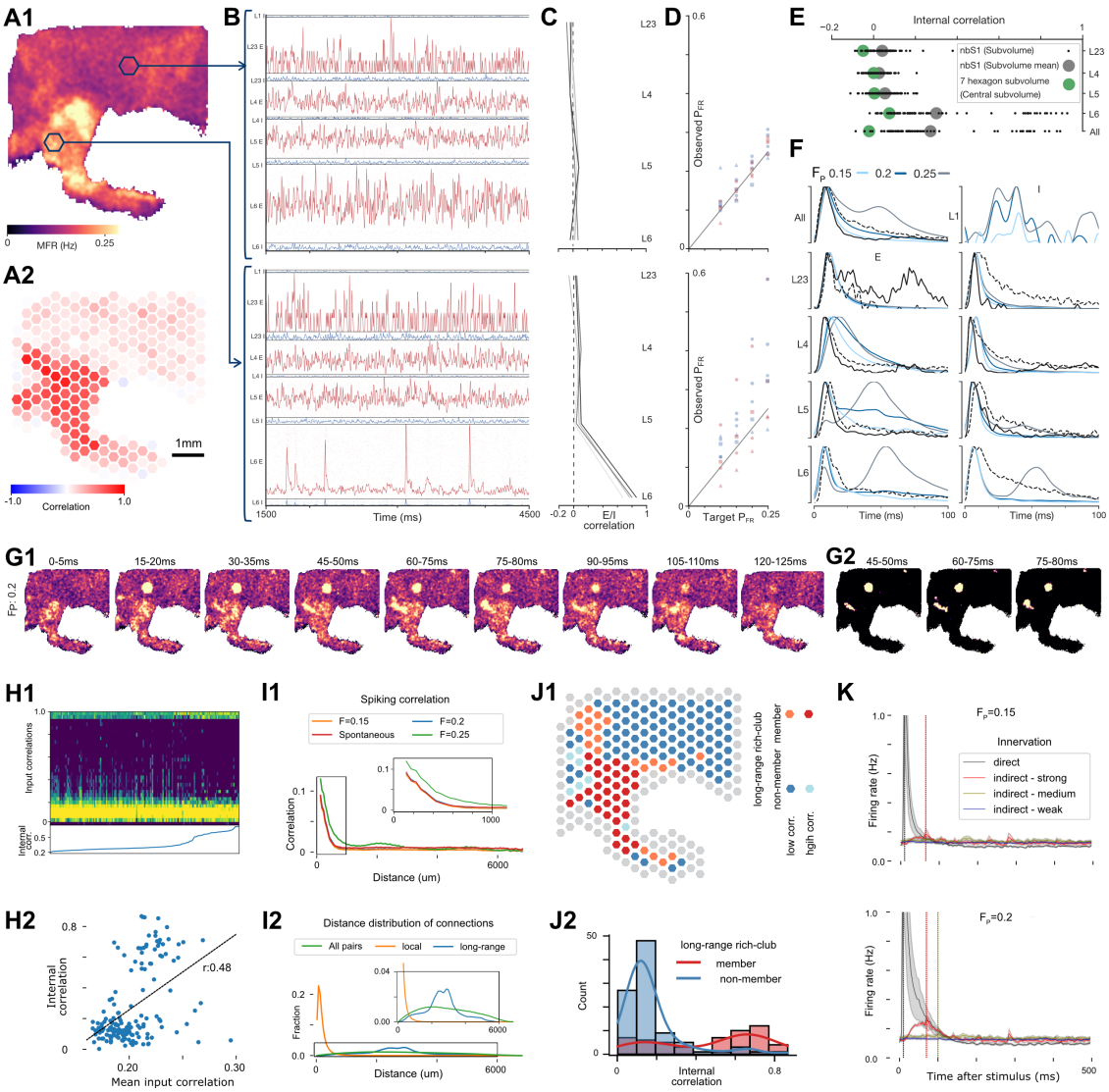

Figure 12: **Full nbS1 spontaneous and evoked activity.** **A1:** Mean firing rates across the model for the parameter combination $[Ca^{2+}]_o = 1.05\,\text{mM}$, $R_{OU} = 0.4$, $P_{FR} = 0.2$. **A2:** Spiking correlations of E/I subpopulations in 240 hexagonal subvolumes (diameter: $\approx 460\,\mu m$) of the nbS1 model. **B:** Spiking activity and max normalised histograms for each layer-wise E and I population for the same parameter combination as in A, and the 0th (upper) and 59th (lower) subvolumes in A2. **C:** Correlations between E and I populations by layer for the four non-bursting simulations. Colour of line from light to dark represents P_{FR}. **D:** Target vs. observed P_{FR} values for the four non-bursting simulations. The number of sides of each marker corresponds to the layer, with L2/3 represented by a triangle. Red and blue shapes represent E and I populations respectively. **E:** Distributions of spiking correlations of layer-specific populations in $460\,\mu m$ hexagonal subvolumes of the nbS1 model (black dots; mean values: grey). Compared to the corresponding values when a smaller subvolume is simulated in isolation (green). **F:** Trial-averaged PSTHs (baseline and max normalised) for the entire population, and for each layer-wise E and I population for each evoked parameter combination. For $F_P = 15\%$ and $F_P = 25\%$ respectively, the evoked responses passed and failed the latency and decay-based criteria tests for similarity to *in vivo*. Response for $F_P = 20\%$ passed the tests for all populations except L5 E which showed a more sustained response than *in vivo*. **G1:** Trial-averaged activity of the full circuit for $F_P = 20\%$ following the single whisker deflection stimulus. **G2:** Subset of time windows from F1 shown with only the top 2% of bins for each time window after the baseline activity level has been subtracted.

H: Correlations of long-range inputs. **H1:** Distribution of spiking correlations of inputs into 240 subvolumes. Calculated at reduced spatial resolution, based on connection counts and correlations between the subvolumes (see Supp. Methods). Subvolumes are sorted by the E/I correlation of neurons within them. For spontaneous activity. **H2:** Mean of the correlations of inputs into 240 subvolumes against internal spiking correlation for all subvolumes during spontaneous activity. Black line: linear fit. Calculated based on connection counts and correlations between $50\,\mu m$ hexagonal subvolumes (see Supp. Methods). Data for evoked activity for both panels is shown in Supp. Fig. S9. **I1**: Spiking correlations of subvolumes against their distances in spontaneous (red) and evoked (orange: $F_p = 0.15\%$, blue: $F_p = 0.2\%$, green: $F_p = 0.25$) activity. For increased spatial resolution, smaller ($58\,\mu m$) subvolumes were used, hence correlation values are not comparable to values in B. **I2:** Distribution of soma distances of neuron pairs connected by local (orange) or long-range (blue) connectivity. Green: distances of all pairs, independent of connectivity. **J1:** Classification of subvolumes based on low or high internal correlation and membership in the long-range rich club Data for evoked activity is shown in Supp. Fig. S9. **J2:** E/I correlation of subvolumes for members of the rich club (red) and non-members (blue). **K:** Firing rates of subvolumes following a stimulus with $F_P = 0.15\%$ (top) and $F_P = 0.2\%$ (bottom). Mean (lines) and SEM (shaded area) over 10 repetitions shown for subvolumes that are directly innervated by the VPM stimulus (black), that are strongly innervated by directly innervated subvolumes (with over 10^6 synapses, red), or by medium strength (over 10^5 synapses, yellow) or weak (over 10^4 synapses) indirect innervation. Dashed lines indicate locations of peaks.

As the model is homogeneous across the different subregions in terms of neuronal morphologies and physiology, we expected the differences in spontaneous and evoked activity across the model to be explained by the topology of synaptic connectivity. While the extrinsic input from the OU injections was uncorrelated by design, synaptic input from local connectivity would feature at least some degree of correlation. This led to the question, how correlated was the input from long-range connections? We estimated for each pair of long-range connections innervating a $460\,\mu m$ hexagonal subvolume its spiking correlation and compared the resulting distribution to the correlation within the subvolume itself (see Supp. Methods; Supp. Fig. 12H1). We found low correlations for most pairs, but with a significant number of high-correlation outliers for subvolumes with high internal correlations. Moreover, when we considered the mean of the measure, we found that it explains most of the variability in internal correlations, for both spontaneous (Fig. 12H2) and evoked states (Supp. Fig. S9).

This led to the following tentative explanation: Local connectivity provides inputs from within $500\,\mu m$, which is virtually guaranteed to be correlated to some degree (Fig. 12I1 vs. I2, orange). This is a result of connections being *locally dense*, as they are concentrated within a small neighborhood. (Fig. 12I2, green vs. orange). Long-range connectivity originates from further away, sampling from different functional units that may or may not be correlated, and being more diluted (Fig. 12I2, green vs. blue). Consequently, long-range inputs are likely to act not much different from the uncorrelated OU process, unless this is overcome by a non-random topology of long-range connectivity. Specifically, we considered the long-range connectivity at meso-scale in terms of the graph of synapse counts between $460\,\mu m$ subvolumes. When the graph was thresholded at 8 million synapses, most subvolumes lacked connections at that strength completely, but others formed a single connected component, indicating the formation of a *rich club* (Colizza et al., 2006; Fig. 12J1, red and orange). We found that subvolumes with high internal correlation were part of the rich club, or directly adjacent to one of its members (Fig. 12J1, J2). In the presence of strong thalamic inputs, this could be overcome, as the increased activity level spread along sufficiently strong long-range connections (Fig. 12K),

albeit with substantial delays between 60 and 100 ms. This could induce high correlations in strongly connected parts of the model, also outside the rich club (Supp. Fig. S9) and shows that the model supports selective propagation of activity to areas efferently connected with long-range connectivity.

4 Discussion

We have demonstrated the physiology and emergent activity of a data-driven, biophysically detailed model of the rat non-barrel primary somatosensory cortex. The model was built with the goal of anatomical completeness, i.e., a one-to-one correspondence between parts of the model and mechanisms or cells of the brain, with an explicit distinction between what is included and what is not in the model. Based on our validations, the model comes close to completeness in terms of neuronal composition, intrinsic synaptic connectivity, and the diversity of neuronal and synaptic physiology, thereby providing biological interpretability of simulation results.

The model exhibited a spectrum of dynamical states that were compatible with *in vivo* spontaneous activity, ranging from highly asynchronous to highly synchronous regimes. A region of the parameter space defined by three meta-parameters supported *in vivo*-like responses to single whisker deflection and active whisker touch stimuli, under anesthetized and awake conditions, respectively. While these responses are from the barrel field, which is not part of the model, single whisker deflections and active whisker touches offer some of the simplest cortical stimulus-response paradigms, providing the opportunity to study fundamental principles of neural dynamics and information processing; in particular, the correspondence between atomic units of sensory information and neural representations.

These initial validations against data from simple stimuli are crucial for complex models, as they provide context for more complex validations. If a model were able to reproduce properties of neural activity in more complex experimental paradigms, but not for more simple experimental paradigms, then it would suggest that the model is acting in a regime different from the corresponding biological tissue. Moreover, in a rich and complex nonlinear system, the source of discrepancies with *in vivo* activity are simpler to ascertain under simpler experimental protocols.

The process of delineating the *in vivo*-like regime also provided insights on its own. First, activity states in the *in vivo*-like regime had increasingly correlated spiking activity and were bounded by states with bursts of activity. This indicates that the *in vivo*-like activity is at the edge of the transition to synchronous activity that has been characterized as computationally optimal in the theoretical literature (edge of chaos, Beggs and Plenz, 2003; Legenstein and Maass, 2007). Additionally, we provided a prediction of the number of thalamic fibers that are stimulated for active and passive whisker touch. Finally, responses were generally closer to the biological data for values of the P_{FR} meta-parameter between 0.1 and 0.3, predicting a severe overestimation of mean firing rates by extracellular spike sorting techniques. It has been pointed out before that spike-sorted multi-electrode extracellular recordings are biased towards larger and more active neurons, leading to overestimates of population activity (Olshausen and Field, 2006). Supporting our estimates, patch-clamp experiments have shown ubiquitous neuronal silence (Crochet and Petersen, 2006), and found spontaneous and stimulus-evoked firing rates in the rat barrel cortex that are as much as 10 times lower than for extracellular recordings (0.05-0.15 Hz vs. 0.8-1.5 Hz; Olshausen and Field, 2006).

Using activity data from any recording technique comes with its own set of challenges and biases (Shoham et al., 2006; Olshausen and Field, 2006; Barth and Poulet, 2012; Wohrer et al., 2013). Calcium imaging and patch-clamp experiments are less biased to-

wards frequently spiking neurons (Wohrer et al., 2013), yet the former can only infer spiking activity and may be biased towards neurons that favour marker expression or uptake. Patch-clamp techniques can reduce firing rates and be biased towards larger or more active neurons (Olshausen and Field, 2006); and are also limited to recording a few neurons simultaneously, preventing characterizations of single trial population dynamics.

Given these complications, how can we be confident that the dynamic states characterized in the model are *in vivo*-like? Certain other features of an *in vivo*-like state are fulfilled by the model. First, we demonstrated correlated spontaneous dynamics in the form of global and local fluctuations and dynamic E-I balance, as found experimentally (Renart et al., 2010). Second, population firing rate distributions were long-tailed with sub 1 Hz peaks, and the distributions were similar for spontaneous and stimulus-evoked activity, as has been previously reported (Wohrer et al., 2013), and such mean firing rates below 1 Hz are also required by metabolic constraints (Attwell and Laughlin, 2001; Lennie, 2003). For evoked activity, we compare the temporal profile of specific subpopulation responses to single whisker deflections and active whisker touches. Regarding response sparsity, comparison of several techniques suggests that 10-20% of neurons spike on a single stimulus trial in the barrel cortex (Barth and Poulet, 2012). Additionally, the majority of cells responding to single whisker deflections spike just once, with the state of spontaneous activity affecting responses on individual trials (Isbister et al., 2021). Both these aspects are consistent with what we found in the model.

As a consequence of the modelling approach, extrinsic sources of excitation from regions that are not part of the model were missing. We model them by injecting a somatic conductance calibrated for specific sub-populations. Although abstract relative to the rest of the model, we found that the amplitudes of the injections could be predicted from the amount of missing extrinsic synapses, suggesting they indeed provide a functional representation of their anatomical counterparts. Lastly, by modeling the extrinsic connectivity in this modular way, it can be refined or replaced in the future, independent of the core model, when larger fractions of the brain are modelled.

Our approach to obtaining *in vivo*-like activity contrasts with a recent approach in a large-scale biophysical model of primary visual cortex of similar scale to our smaller subvolume (Billeh et al., 2020). There, they delivered extrinsic inputs through dendritic synapses instead of somatic injection, which is more anatomically realistic, and they adjusted intrinsic recurrent weights to match extracellularly recorded firing rates. They find a single activity state, instead of the *in vivo*-compatible spectrum here that allowed us to contrast anesthetized and awake states.

Part of the calibration of extrinsic inputs was the approximation of the relationship between unconnected and connected firing rates for different subpopulations. We simplified this highly complex problem of many variables by approximating it only for states where firing rates are a constant proportion of reference rates, thereby making it dependent on only a single variable, P_{FR}. This required several refinement steps, but the number of iterations could be reduced by starting with a calibration from a related model. The efficiency of the optimisation process is critical, given the large computational cost of simulations. The ratios of connected divided by unconnected firing rates are a prediction of the degree to which the activity of a population is determined by incoming connections from local sources. We found an increase of the importance of local connectivity from

superficial to deeper layers. This is largely in line with the canonical view of the cortex (Lübke and Feldmeyer, 2007; Feldmeyer, 2012), which places layers 5 and especially 6 at the end of local (i.e., intra-columnar) information flow.

It is important to highlight several ways in which the model deviates from the biological data. For example, differences in the timing of responses of inhibitory subpopulations to stimuli were not reproduced. Furthermore, the model omits several known anatomical elements, such as glia and the presence of gap junctions between certain neurons types, but the clear spatial context of the model provides a natural scaffold to add them in the future. Some shortcomings indicate a lack of available experimental data. For example, the physiological strength of thalamic inputs onto many cortical populations remain unclear as the best available data mixes structural and physiological strength (Sermet et al., 2019). Importantly, improving on these mismatches can provide insights. Specifically, our modelling techniques assume generality of rules and parameters, unless indicated by the data. Therefore, violations indicate specific biological rules. For example, the thalamic inputs into the model innervate any dendrite placed in the targeted layers equally. The delay of responses of PV+ and Sst+ neurons in layer 4 could be adjusted to match the biological data better by biasing the innervation to prefer PV+ dendrites over Sst+ dendrites. We release this model to allow the community to identify further data-model mismatches, revealing gaps in current understanding of cortex, and drive further insights and refinement.

In simulations of spontaneous activity of the model, we found emerging spatial inhomogeneities in network activity. Specifically, we observed sharp transitions in firing rates and pairwise correlations at disgranular zones. This highlights that the model supports several, independently acting functional units. Analysis of spatial correlations suggests a radius of approximately $400\,\mu m$ for a single unit. This property that was not present in the previous intra-regional scale model (Markram et al., 2015), but is rather an emergent property of the inter-regional scale, demonstrating that we achieved our goal of building a model that can be used to study long-range interactions between individual regions. Analyzing the source of the inhomogeneities suggested a prominent role of a non-random rich-club structure of long-range connections at the meso-scale. Within functional units, we found that the inhomogeneous increases of spiking correlations were confined to spontaneous packets of activity in L6.

In addition to demonstrating close similarity with *in vivo* responses to single whisker deflection and active whisker touch, we also reproduced protocols from three published laboratory experiments. The selected paradigms used a wide array of experimental techniques, which could be accurately recreated due to the close spatial and anatomical correspondence between the model and the biological tissue. Additionally, we were able to go beyond the original experiments. For example, we predicted an increased number of neurons would be required to have a decodable effect on postsynatic activity under *in vivo* conditions over the *in vitro* conditions of the original experiment. This can be explained by the presence of more noise at the lower synaptic reliability under *in vivo* conditions. This demonstrates that the approach of modelling entire brain regions can be used to probe further the topics of the original articles and cortical processing more generally. For example, we have already demonstrated the role of correlations in the long-rage interactions between regions in shaping the local activity state. But this was limited to spontaneous activity or individual, simple stimuli. The model also allows the

simulation-based study of processing in cortical hierarchies in more complex setups, for example studying the integration of increasing numbers of stimuli applied to distal parts of the model. This line of inquiry will also allow us to improve the model of extrinsic synaptic inputs. To minimize assumptions about model-extrinsic activity, we modeled these as statistically independent conductance injections. In the biological brain, these inputs are signals from other regions rather than noise, and would have certain correlations. Studying activity in more complex simulation paradigms at large spatial scales may allow us to characterize expected correlations and replace independent with more specific conductance injections.

Furthermore, the model will allow us to create more specific predictions about the severity and nature of the extracellular spike sorting bias. An earlier version of the model has been used to simulate cortical extracellular potentials (Reimann et al., 2013). We can use the present version of the model to emulate recordings with different types of extracellular electrodes and compare spike sorting results to the ground truth. The large scale of the model ensures the presence of contributions of distal neurons to the signal; together with the *in vivo*-like state this will make the prediction biologically relevant.

Finally, the model provides an opportunity to study synaptic plasticity under *in vivo*-like conditions at the level of interacting regions, thought to play an important role in cortical learning. Plasticity has been extensively characterized at the level of pairs of neurons (Markram et al., 1997b; Larsen and Sjöström, 2015), or in terms of changes in individual neurons. However, the study of the relationship between plasticity and learning has been hampered by the small spatial scale of the circuits studied relative to the circuits involved in learning. In an earlier version of this model, we implemented a plasticity rule that captures the roles of calcium and dendritic integration in plasticity (Chindemi et al., 2022). Together with the present model, we can bridge the scales from these local mechanisms to interregional interactions to elucidate the structure of learning in neocortical hierarchies.

References

Abdellah, M., Hernando, J., Eilemann, S., Lapere, S., Antille, N., Markram, H., and Schürmann, F. (2018). NeuroMorphoVis: A collaborative framework for analysis and visualization of neuronal morphology skeletons reconstructed from microscopy stacks. *Bioinformatics*, 34(13):i574–i582.

Al-Juboori, S. I., Dondzillo, A., Stubblefield, E. A., Felsen, G., Lei, T. C., and Klug, A. (2013). Light scattering properties vary across different regions of the adult mouse brain. *PloS one*, 8(7):e67626.

Amzica, F., Massimini, M., and Manfridi, A. (2002). Spatial buffering during slow and paroxysmal sleep oscillations in cortical networks of glial cells in vivo. *Journal of Neuroscience*, 22(3):1042–1053.

Ascoli, G. A. et al. (2008). Petilla terminology: Nomenclature of features of GABAergic interneurons of the cerebral cortex. *Nature Reviews Neuroscience*, 9(7):557–568.

Attwell, D. and Laughlin, S. B. (2001). An energy budget for signaling in the grey matter of the brain. *Journal of Cerebral Blood Flow & Metabolism*, 21(10):1133–1145.

Azimipour, M., Baumgartner, R., Liu, Y., Jacques, S. L., Eliceiri, K. W., and Pashaie, R. (2014). Extraction of optical properties and prediction of light distribution in rat brain tissue. *Journal of biomedical optics*, 19(7):075001.

Barros-Zulaica, N., Rahmon, J., Chindemi, G., Perin, R., Markram, H., Muller, E., and Ramaswamy, S. (2019). Estimating the Readily-Releasable Vesicle Pool Size at Synaptic Connections in the Neocortex. *Frontiers in Synaptic Neuroscience*, 11(29).

Barth, A. L. and Poulet, J. F. (2012). Experimental evidence for sparse firing in the neocortex. *Trends in neurosciences*, 35(6):345–355.

Beggs, J. M. and Plenz, D. (2003). Neuronal avalanches in neocortical circuits. *Journal of neuroscience*, 23(35):11167–11177.

Beierlein, M. and Connors, B. W. (2002). Short-term dynamics of thalamocortical and intracortical synapses onto layer 6 neurons in neocortex. *Journal of Neurophysiology*, 88(4):1924–1932.

Beierlein, M., Gibson, J. R., and Connors, B. W. (2003). Two Dynamically Distinct Inhibitory Networks in Layer 4 of the Neocortex. *Journal of Neurophysiology*, 90(5):2987–3000.

Berger, T. (2009). *Properties of Neocortical Microcircuits*. PhD thesis, Ecole Polytechnique Fédérale de Lausanne.

Berger, T., Larkum, M. E., and Lüscher, H. R. (2001). High Ih channel density in the distal apical dendrite of layer V pyramidal cells increases bidirectional attenuation of EPSPs. *Journal of Neurophysiology*, 85(2):855–868.

Billeh, Y. N., Cai, B., Gratiy, S. L., Dai, K., Iyer, R., Gouwens, N. W., Abbasi-Asl, R., Jia, X., Siegle, J. H., Olsen, S. R., Koch, C., Mihalas, S., and Arkhipov, A. (2020). Systematic Integration of Structural and Functional Data into Multi-Scale Models of Mouse Primary Visual Cortex. *Neuron*, 106(3):388–403.

Bolaños-Puchet, S. and Reimann, M. W. (in prep.). Flattening of enhanced cortical atlases opens up new possibilities for data-driven modeling and data visualization. *in prep.*

Borst, J. G. G. (2010). The low synaptic release probability in vivo. *Trends in neurosciences*, 33(6):259–266.

Brasier, D. J. and Feldman, D. E. (2008). Synapse-specific expression of functional presynaptic NMDA receptors in rat somatosensory cortex. *Journal of Neuroscience*, 28(9):2199–2211.

Buzsáki, G. (2004). Large-scale recording of neuronal ensembles. *Nature Neuroscience*, 7(5):446–451. Number: 5 Publisher: Nature Publishing Group.

Chindemi, G., Abdellah, M., Amsalem, O., Benavides-Piccione, R., Delattre, V., Doron, M., Ecker, A., Jaquier, A. T., King, J., Kumbhar, P., Monney, C., Perin, R., Rössert, C., Tuncel, M. A., van Geit, W., DeFelipe, J., Graupner, M., Segev, I., Markram, H., and Muller, E. (2022). A calcium-based plasticity model predicts long-term potentiation and depression in the neocortex. *Nature Communications*, 13(3038).

Colizza, V., Flammini, A., Serrano, M. A., and Vespignani, A. (2006). Detecting rich-club ordering in complex networks. *Nature physics*, 2(2):110–115.

Constantinople, C. M. and Bruno, R. M. (2013). Deep Cortical Layers Are Activated Directly by Thalamus. *Science*, 340(6140):1591–1594.

Cremonesi, F., Hager, G., Wellein, G., and Schürmann, F. (2020). Analytic performance modeling and analysis of detailed neuron simulations. *International Journal of High Performance Computing Applications*, 34((4)):428–449.

Crochet, S. and Petersen, C. C. (2006). Correlating whisker behavior with membrane potential in barrel cortex of awake mice. *Nature Neuroscience*, 9(5):608–610.

Dai, K., Hernando, J., Billeh, Y. N., Gratiy, S. L., Planas, J., Davison, A. P., Dura-Bernal, S., Gleeson, P., Devresse, A., Dichter, B. K., Gevaert, M., King, J. G., van Geit, W. A., Povolotsky, A. V., Muller, E., Courcol, J. D., and Arkhipov, A. (2020). The SONATA data format for efficient description of large-scale network models. *PLoS Computational Biology*, 16(2):e1007696.

Datwani, A., Iwasato, T., Itohara, S., and Erzurumlu, R. S. (2002). NMDA receptor-dependent pattern transfer from afferents to postsynaptic cells and dendritic differentiation in the barrel cortex. *Molecular and Cellular Neuroscience*, 21(3):477–492.

De Kock, C., Bruno, R. M., Spors, H., and Sakmann, B. (2007). Layer-and cell-type-specific suprathreshold stimulus representation in rat primary somatosensory cortex. *The Journal of physiology*, 581(1):139–154.

Destexhe, A., Rudolph, M., Fellous, J. M., and Sejnowski, T. J. (2001). Fluctuating synaptic conductances recreate in vivo-like activity in neocortical neurons. *Neuroscience*, 107(1):13–24.

Diamond, M. E., Armstrong-James, M., and Ebner, F. F. (1992). Somatic sensory responses in the rostral sector of the posterior group (pom) and in the ventral posterior medial nucleus (vpm) of the rat thalamus. *Journal of Comparative Neurology*, 318(4):462–476.

Ecker, A., Romani, A., Sáray, S., Káli, S., Migliore, M., Falck, J., Lange, S., Mercer, A., Thomson, A. M., Muller, E., Reimann, M. W., and Ramaswamy, S. (2020). Data-driven integration of hippocampal CA1 synaptic physiology in silico. *Hippocampus*, 30(11):1129–1145.

Feldmeyer, D. (2012). Excitatory neuronal connectivity in the barrel cortex. *Frontiers in Neuroanatomy*, 6(24).

Feldmeyer, D., Egger, V., Lübke, J., and Sakmann, B. (1999). Reliable synaptic connections between pairs of excitatory layer 4 neurones within a single 'barrel' of developing rat somatosensory cortex. *Journal of Physiology*, 521(1):169–190.

Feldmeyer, D., Lübke, J., and Sakmann, B. (2006). Efficacy and connectivity of intracolumnar pairs of layer 2/3 pyramidal cells in the barrel cortex of juvenile rats. *Journal of Physiology*, 575(2):583–602.

Feldmeyer, D., Lübke, J., Silver, R. A., and Sakmann, B. (2002). Synaptic connections between layer 4 spiny neurone-layer 2/3 pyramidal cell pairs in juvenile rat barrel cortex: Physiology and anatomy of interlaminar signalling within a cortical column. *Journal of Physiology*, 538(3):803–822.

Feldmeyer, D., Roth, A., and Sakmann, B. (2005). Monosynaptic connections between pairs of spiny stellate cells in layer 4 and pyramidal cells in layer 5A indicate that lemniscal and paralemniscal afferent pathways converge in the infragranular somatosensory cortex. *Journal of Neuroscience*, 25(13):3423–3431.

Felleman, D. J. and Van Essen, D. C. (1991). Distributed hierarchical processing in the primate cerebral cortex. *Cerebral Cortex*, 1:1–47.

Fuhrmann, G., Segev, I., Markram, H., and Tsodyks, M. (2002). Coding of Temporal Information by Activity-Dependent Synapses. *Journal of Neurophysiology*, 87(1):140–148.

Gao, L., Liu, S., Gou, L., Hu, Y., Liu, Y., Deng, L., Ma, D., Wang, H., Yang, Q., Chen, Z., Liu, D., Qiu, S., Wang, X., Wang, D., Wang, X., Ren, B., Liu, Q., Chen, T., Shi, X., Yao, H., Xu, C., Li, C. T., Sun, Y., Li, A., Luo, Q., Gong, H., Xu, N., and Yan, J. (2022). Single-neuron projectome of mouse prefrontal cortex. *Nature Neuroscience*, 25(4):515–529.

Gias, C., Hewson-Stoate, N., Jones, M., Johnston, D., Mayhew, J., and Coffey, P. (2005). Retinotopy within rat primary visual cortex using optical imaging. *Neuroimage*, 24(1):200–206.

Gonzalez, K. C., Losonczy, A., and Negrean, A. (2022). Dendritic Excitability and Synaptic Plasticity In Vitro and In Vivo. *Neuroscience*, 489:165–175.

Gupta, A., Wang, Y., and Markram, H. (2000). Organizing principles for a diversity of GABAergic interneurons and synapses in the neocortex. *Science*, 287(5451):273–278.

Harris, J. A., Mihalas, S., et al. (2019). Hierarchical organization of cortical and thalamic connectivity. *Nature*, 575(7781):195–202.

Henze, D. A., Borhegyi, Z., Csicsvari, J., Mamiya, A., Harris, K. D., and Buzsaki, G. (2000). Intracellular features predicted by extracellular recordings in the hippocampus in vivo. *Journal of neurophysiology*, 84(1):390–400.

Isbister, J. B., Reyes-Puerta, V., Sun, J.-J., Horenko, I., and Luhmann, H. J. (2021). Clustering and control for adaptation uncovers time-warped spike time patterns in cortical networks in vivo. *Scientific Reports*, 11(1):1–20.

Jahr, C. E. and Stevens, C. F. (1990). Voltage dependence of NMDA-activated macroscopic conductances predicted by single-channel kinetics. *The Journal of neuroscience*, 10(9):3178–3182.

Jones, H. and Keep, R. (1988). Brain Fluid Calcium Concentration and Response To Acute Hypercalcaemia During Development in the Rat. *Journal of Physiology*, 402:579–593.

Kawaguchi, Y., Karube, F., and Kubota, Y. (2006). Dendritic branch typing and spine expression patterns in cortical nonpyramidal cells. *Cerebral Cortex*, 16(5):696–711.

Kumbhar, P., Hines, M., Fouriaux, J., Ovcharenko, A., King, J., Delalondre, F., and Schürmann, F. (2019). CoreNEURON : An Optimized Compute Engine for the NEURON Simulator. *Frontiers in Neuroinformatics*, 13(63).

Larkman, A. U. (1991). Dendritic morphology of pyramidal neurones of the visual cortex of the rat: Iii. spine distributions. *Journal of comparative neurology*, 306(2):332–343.

Larkum, M. E., Zhu, J. J., and Sakmann, B. (2001). Dendritic mechanisms underlying the coupling of the dendritic with the axonal action potential initiation zone of adult rat layer 5 pyramidal neurons. *Journal of Physiology*, 533(2):447–466.

Larsen, R. S. and Sjöström, P. J. (2015). Synapse-type-specific plasticity in local circuits. *Current Opinion in Neurobiology*, 35:127–135.

Le Bé, J. V., Silberberg, G., Wang, Y., and Markram, H. (2007). Morphological, electrophysiological, and synaptic properties of corticocallosal pyramidal cells in the neonatal rat neocortex. *Cerebral Cortex*, 17(9):2204–2213.

Legenstein, R. and Maass, W. (2007). Edge of chaos and prediction of computational performance for neural circuit models. *Neural networks*, 20(3):323–334.

Lennie, P. (2003). The cost of cortical computation. *Current biology*, 13(6):493–497.

Ling, D. S. and Benardo, L. S. (1999). Restrictions on inhibitory circuits contribute to limited recruitment of fast inhibition in rat neocortical pyramidal cells. *Journal of Neurophysiology*, 82(4):1793–1807.

Loebel, A., Silberberg, G., Helbig, D., Markram, H., Tsodyks, M., and Richardson, M. J. E. (2009). Multiquantal release underlies the distribution of synaptic efficacies in the neocortex. *Frontiers in Cellular Neuroscience*, 3(27).

Lübke, J. and Feldmeyer, D. (2007). Excitatory signal flow and connectivity in a cortical column: Focus on barrel cortex. *Brain Structure and Function*, 212:3–17.

Markram, H., Lübke, J., Frotscher, M., Roth, A., and Sakmann, B. (1997a). Physiology and anatomy of synaptic connections between thick tufted pyramidal neurones in the developing rat neocortex. *Journal of Physiology*, 500(2):409–440.

Markram, H., Lübke, J., Frotscher, M., and Sakmann, B. (1997b). Regulation of Synaptic Efficacy by Coincidence of Postsynaptic APs and EPSPs. *Science*, 275(5297):213–215.

Markram, H., Muller, E., Ramaswamy, S., Reimann, M. W., et al. (2015). Reconstruction and Simulation of Neocortical Microcircuitry. *Cell*, 163(2):456–492.

Markram, H., Toledo-Rodriguez, M., Wang, Y., Gupta, A., Silberberg, G., and Wu, C. (2004). Interneurons of the neocortical inhibitory system. *Nature Reviews Neuroscience*, 5(10):793–807.

Markram, H., Wang, Y., and Tsodyks, M. (1998). Differential signaling via the same axon of neocortical pyramidal neurons. *PNAS*, 95(9):5323–8.

Massimini, M. and Amzica, F. (2001). Extracellular calcium fluctuations and intracellular potentials in the cortex during the slow sleep oscillation. *Journal of Neurophysiology*, 85(3):1346–1350.

Mesradi, M., Genoux, A., Cuplov, V., Abi-Haidar, D., Jan, S., Buvat, I., and Pain, F. (2013). Experimental and analytical comparative study of optical coefficient of fresh and frozen rat tissues. *Journal of biomedical optics*, 18(11):117010.

Meyer, H. S., Wimmer, V. C., Hemberger, M., Bruno, R. M., De Kock, C. P., Frick, A., Sakmann, B., and Helmstaedter, M. (2010). Cell type-specific thalamic innervation in a column of rat vibrissal cortex. *Cerebral Cortex*, 20(10):2287–2303.

Muller, E., Buesing, L., Schemmel, J., and Meier, K. (2007). Spike-Frequency Adapting Neural Ensembles: Beyond Mean Adaptation and Renewal Theories. *Neural Computation*, 19:2958–3010.

Nevian, T., Larkum, M. E., Polsky, A., and Schiller, J. (2007). Properties of basal dendrites of layer 5 pyramidal neurons: A direct patch-clamp recording study. *Nature Neuroscience*, 10(2):206–214.

Newton, T. H., Reimann, M. W., Abdellah, M., Chevtchenko, G., Muller, E. B., and Markram, H. (2021). In silico voltage-sensitive dye imaging reveals the emergent dynamics of cortical populations. *Nature Communications*, 12(3630).

Nolte, M., Gal, E., Markram, H., and Reimann, M. W. (2020). Impact of higher order network structure on emergent cortical activity. *Network Neuroscience*, 4(1):292–314.

Nolte, M., Reimann, M. W., King, J. G., Markram, H., and Muller, E. B. (2019). Cortical reliability amid noise and chaos. *Nature Communications*, 10(3792).

Ohana, O. and Sakmann, B. (1998). Transmitter release modulation in nerve terminals of rat neocortical pyramidal cells by intracellular calcium buffers. *The Journal of Physiology*, 513(1):135–148.

Olshausen, B. A. and Field, D. J. (2006). What is the other 85 percent of v1 doing. *L. van Hemmen, & T. Sejnowski (Eds.)*, 23:182–211.

Park, J. M., Hong, Y. K., Rodgers, C. C., Dahan, J. B., Schmidt, E. R., and Bruno, R. M. (2020). Deep and superficial layers of the primary somatosensory cortex are critical for whisker-based texture discrimination in mice. *bioRxiv*.

Pedreira, C., Martinez, J., Ison, M. J., and Quiroga, R. Q. (2012). How many neurons can we see with current spike sorting algorithms? *Journal of neuroscience methods*, 211(1):58–65.

Petersen, R. S., Brambilla, M., Bale, M. R., Alenda, A., Panzeri, S., Montemurro, M. A., and Maravall, M. (2008). Diverse and Temporally Precise Kinetic Feature Selectivity in the VPm Thalamic Nucleus. *Neuron*, 60(5):890–903.

Prince, L. Y., Tran, M. M., Grey, D., Saad, L., Chasiotis, H., Kwag, J., Kohl, M. M., and Richards, B. A. (2021). Neocortical inhibitory interneuron subtypes are differentially attuned to synchrony-and rate-coded information. *Communications Biology*, 4(1):1–16.

Qi, G. and Feldmeyer, D. (2016). Dendritic Target Region-Specific Formation of Synapses between Excitatory Layer 4 Neurons and Layer 6 Pyramidal Cells. *Cerebral Cortex*, 26(4):1569–1579.

Reimann, M. W., Anastassiou, C. A., Perin, R., Hill, S. L., Markram, H., and Koch, C. (2013). A biophysically detailed model of neocortical local field potentials predicts the critical role of active membrane currents. *Neuron*, 79(2):375–390.

Reimann, M. W., Nolte, M., Scolamiero, M., Turner, K., Perin, R., Chindemi, G., Dłotko, P., Levi, R., Hess, K., and Markram, H. (2017). Cliques of neurons bound into cavities provide a missing link between structure and function. *Frontiers in Computational Neuroscience*, 11(48).

Reimann, M. W., Puchet, S. B., Santander, D. E., Courcol, J.-D., et al. (2022a). Modeling and simulation of rat non-barrel somatosensory cortex. part i: Modeling anatomy. *bioRxiv*.

Reimann, M. W., Riihimäki, H., Smith, J. P., Lazovskis, J., Pokorny, C., and Levi, R. (2022b). Topology of synaptic connectivity constrains neuronal stimulus representation, predicting two complementary coding strategies. *PLoS ONE*, 17(1):e0261702.

Renart, A., De La Rocha, J., Bartho, P., Hollender, L., Parga, N., Reyes, A., and Harris, K. D. (2010). The asynchronous state in cortical circuits. *science*, 327(5965):587–590.

Reva, M., Rössert, C., Arnaudon, A., Damart, T., Mandge, D., Tuncel, A., Ramaswamy, S., Markram, H., and Van Geit, W. (2022). A universal workflow for creation, validation and generalization of detailed neuronal models. *bioRxiv*.

Reyes, A. and Sakmann, B. (1999). Developmental switch in the short-term modification of unitary EPSPs evoked in layer 2/3 and layer 5 pyramidal neurons of rat neocortex. *Journal of Neuroscience*, 19(10):3827–3835.

Reyes-Puerta, V., Sun, J.-J., Kim, S., Kilb, W., and Luhmann, H. J. (2015). Laminar and columnar structure of sensory-evoked multineuronal spike sequences in adult rat barrel cortex in vivo. *Cerebral Cortex*, 25(8):2001–2021.

Rozov, A., Burnashev, N., Sakmann, B., and Neher, E. (2001). Transmitter release modulation by intracellular ca2+ buffers in facilitating and depressing nerve terminals of pyramidal cells in layer 2/3 of the rat neocortex indicates a target cell-specific difference in presynaptic calcium dynamics. *The Journal of physiology*, 531(3):807–826.

Sermet, B. S., Truschow, P., Feyerabend, M., Mayrhofer, J. M., Oram, T. B., Yizhar, O., Staiger, J. F., and Petersen, C. C. (2019). Pathway-, layer-and cell-type-specific thalamic input to mouse barrel cortex. *eLife*, 8:e52665.

Shapiro, J. T., Michaud, N. M., King, J. L., and Crowder, N. A. (2022). Optogenetic activation of interneuron subtypes modulates visual contrast responses of mouse v1 neurons. *Cerebral Cortex*, 32(5):1110–1124.

Shoham, S., O'Connor, D. H., and Segev, R. (2006). How silent is the brain: is there a "dark matter" problem in neuroscience? *Journal of Comparative Physiology A*, 192(8):777–784.

Silberberg, G. and Markram, H. (2007). Disynaptic Inhibition between Neocortical Pyramidal Cells Mediated by Martinotti Cells. *Neuron*, 53(5):735–746.

Sizemore, A. E., Giusti, C., Kahn, A., Vettel, J. M., Betzel, R. F., and Bassett, D. S. (2018). Cliques and cavities in the human connectome. *Journal of computational neuroscience*, 44:115–145.

Stepanyants, A., Martinez, L. M., Ferecskó, A. S., and Kisvárday, Z. F. (2009). The fractions of short- and long-range connections in the visual cortex. *PNAS*, 106(9):3555–3560.

Stuart, G. J. and Sakmann, B. (1994). Active propogation of somatic action potentials into neocortical pyrimidal cell dendrites. *Nature*, 367(January):69–72.

Tsodyks, M. and Markram, H. (1997). The neural code between neocortical pyramidal neurons depends on neurotransmitter release probability. *PNAS*, 94:719–723.

Van Geit, W., Gevaert, M., Chindemi, G., Rössert, C., Courcol, J. D., Muller, E. B., Schürmann, F., Segev, I., and Markram, H. (2016). BluePyOpt: Leveraging open source software and cloud infrastructure to optimise model parameters in neuroscience. *Frontiers in Neuroinformatics*, 10(17).

Varani, S., Vecchia, D., Zucca, S., Forli, A., and Fellin, T. (2022). Stimulus Feature-Specific Control of Layer 2 / 3 Subthreshold Whisker Responses by Layer 4 in the Mouse Primary Somatosensory Cortex. *Cerebral Cortex*, 32(7):1419–1436.

Vargas-Caballero, M. and Robinson, H. P. (2003). A slow fraction of Mg2+ unblock of NMDA receptors limits their contribution to spike generation in cortical pyramidal neurons. *Journal of Neurophysiology*, 89(5):2778–2783.

Wang, Y., Gupta, A., Toledo-Rodriguez, M., Wu, C. Z., and Markram, H. (2002). Anatomical, physiological, molecular and circuit properties of nest basket cells in the developing somatosensory cortex. *Cerebral cortex*, 12(4):395–410.

Wohrer, A., Humphries, M. D., and Machens, C. K. (2013). Population-wide distributions of neural activity during perceptual decision-making. *Progress in neurobiology*, 103:156–193.

Wozny, C. and Williams, S. R. (2011). Specificity of synaptic connectivity between layer 1 inhibitory interneurons and layer 2/3 pyramidal neurons in the rat neocortex. *Cerebral Cortex*, 21(8):1818–1826.

Yang, D., Günter, R., Qi, G., Radnikow, G., and Feldmeyer, D. (2020). Muscarinic and Nicotinic Modulation of Neocortical Layer 6A Synaptic Microcircuits Is Cooperative and Cell-Specific. *Cerebral Cortex*, 30(6):3528–3542.

Yang, D., Qi, G., Ding, C., and Feldmeyer, D. (2022). Layer 6A Pyramidal Cell Subtypes Form Synaptic Microcircuits with Distinct Functional and Structural Properties. *Cerebral Cortex*, 32(10):2095–2111.

Yu, J., Hu, H., Agmon, A., and Svoboda, K. (2019). Recruitment of gabaergic interneurons in the barrel cortex during active tactile behavior. *Neuron*, 104(2):412–427.

Data and Code Availability

The seven column subvolume of the model is available under the following DOI: 10.5281/zenodo.7930276 in SONATA format (Dai et al., 2020). The following software is available on the Blue Brain GitHub page:

- Electrical models were optimized using eFEL and BluePyOpt
- Circuits and simulations were analyzed using Blue Brain SNAP, based on libsonata and NeuroM
- Simulations were executed using CoreNeuron (Kumbhar et al., 2019)

The simulator front-end that loads the SONATA model, and instantiates the simulation to be run in CoreNEURON will be open sourced upon journal submission on the same GitHub page.

Acknowledgements

The authors would like to thank Fabien Delalondre, Adrien Devresse, Hugo Dictus, Juan B. Hernando, Nicolas Cornu, Daniel Fernandez, Jeremy Fouriaux and Ioannis Magnakaris for helpful discussions and contributions to the model; Eva Kenny for help with project management; Cyrille Favreau, Marwan Abdellah and Nadir Roman for support with graphics and figure design and Karin Holm and Akiko Sato for support of manuscript development and helpful discussions. The authors would also like to thank Heiko Luhmann, Vicente Reyes Puerta and Jhy-Jung Sun for supporting access to data used in the primary validation of the model.

Funding

This study was supported by funding to the Blue Brain Project, a research center of the École polytechnique fédérale de Lausanne (EPFL), from the Swiss government's ETH Board of the Swiss Federal Institutes of Technology.

Supplementary Material

Supplementary Methods

Ohrstein-Uhlenbeck process for missing input compensation

Random background synaptic inputs, representing uncorrelated inputs from other brain regions not present in the model, are modelled as a conductance-based somatic injection (Fig. 5A2). Specifically, we inject conductance signals described by an Ornstein-Uhlenbeck (OU) process (similar to Destexhe et al. (2001)), given by the following equation:

$$\frac{dg(t)}{dt} = -\frac{1}{\tau}[g(t) - g_0] + \sqrt{D} \tag{1}$$

where $g(t)$ is the conductance signal, g_0 its mean value, τ is the decay time constant, D is the diffusion coefficient, and $\chi(t)$ is a Gaussian white noise process. The diffusion coefficient can also be expressed in terms of the standard deviation σ of the signal: $D = \frac{2\sigma^2}{\tau}$. Note that we only consider an excitatory conductance signal representing long-range excitatory drive, whereas local inhibitory input is deemed sufficient within the circuit model.

As we are modeling a non-specific random background noise, we use a different, uncorrelated OU process for each cell.

Given the diversity of morphologies and electrical behaviors of cells in our circuit, we scale the mean and standard deviation of the injected signal based on individual cell properties. Specifically, we compute the input resistance R_{in} of each cell at its resting potential, then take its reciprocal value $G_{in} = 1/R_{in}$ (units of conductance). The mean g_0 and standard deviation σ of the injected conductance signal are then expressed as percentages OU_μ and OU_σ of this input conductance G_{in}:

$$g_0 = \frac{OU_\mu}{100} * G_{in} \tag{2}$$

$$\sigma = \frac{OU_\sigma}{100} * G_{in} \tag{3}$$

The OU_μ and OU_σ percentage values are used in the calibration technique described in the following sections. To reiterate, OU_μ and OU_σ scale the mean of the injected conductance and the size its fluctuations respectively.

Modelling optogenetic inhibition or activation

We model optogenetic inhibition or activation of a neuron population through a current injection at the soma of each cell in the population, with an intensity proportional to the cell's threshold current (see Reva et al. (2022)). To mimic the conditions of surface illumination, we considered the dependence of effective depolarization strength on cortical depth using a modified Beer-Lambert law approximation for the exponential attenuation of light intensity through scattering tissue (Al-Juboori et al., 2013; Azimipour et al., 2014, Supp. Fig. S2B):

$$I(d) = I_0 \exp(-\mu_{eff}\, d) \tag{4}$$

where $I(d)$ describes the light intensity at depth d (in mm), with a maximum light intensity I_0 (on the surface of the cortex) and an effective attenuation coefficient given by:

$$\mu_{eff} = \sqrt{3\mu_a(\mu_a + \mu_s')} \tag{5}$$

Values for the absorption coefficient μ_a and the reduced scattering coefficient μ_s' were interpolated for the chosen wavelength from Mesradi et al. (2013). For implementation reasons, the targeted cells were grouped into depth bins and for each group the intensity at the center of the bin was used. Bins were equally distributed in terms of the injected current, and not in terms of depth. The value of I_0 was calibrated independently for each experimental paradigm.

Modelling sensory inputs

Sensory inputs were simulated using a three step procedure (Supp. Fig. S2C2): First, a time series representing sensory stimulation is assigned to each selected thalamic fiber; second, the time series is optionally transformed with a fiber-dependent transfer function; third, a spike train is generated from the time series through a stochastic spiking process. Thalamic input fibers were associated with roughly columnar, overlapping volumes of the model that they formed synaptic connections in (Reimann et al., 2022a). Their centers were projected into the plane using a flat map of the model (Bolaños-Puchet and Reimann,

prep), yielding $[x_\zeta, y_\zeta]$, the *flat locations* of each fiber ζ. A sensory stimulus was defined based on fiber location as $\rho_\zeta(t) = \rho(x_\zeta, y_\zeta, t)$. The stimulus function could be partially stochastic and its value was evaluated for each time bin of the simulation (Supp. Fig. S2C1). Next, a fiber could be associated with a transfer function υ_ζ that transforms the results of ρ. If none is mentioned, identity was used as transfer function. Finally, a spiking process ψ was used to instantiate a spike train for each fiber, based on its transformed time series. That is, the spike train associated with ζ was $\Gamma_\zeta = \psi(\upsilon_\zeta(\rho_\zeta))$. The processes used were stochastic, leading to different spike trains for fibers associated with the same time series. Different, specific ρ, υ and ψ were used for different experimental paradigms that will be further described below.

L4's contribution to L2/3 responses during a whisker hold stimulus

To study how input from L4 contributes to L2/3 subthreshold responses Varani et al. (2022) used a 500 ms long whisker hold paradigm, while patch-clamping PCs in L2/3 in anesthetized and awake mice. We encoded the whisker hold stimulus as a step function ($\rho_\zeta(t) = 1$, if 2000 ms $\leq$ t $<$ 2500 ms, 0 otherwise) in 10% of the VPM fibers within the seven column subvolume. One of four transfer functions were assigned to each fiber, based on the types of kinetic response properties of thalamic neurons identified in (Petersen et al., 2008). The types were selective for whisker position (υ_{pos}), velocity (υ_{vel}), acceleration (υ_{acc}), or direction (υ_{dir}), and were implemented as:

$$
\begin{aligned}
\upsilon_{pos}(t) &= r_{max} \cdot \rho(t) \\
\upsilon_{vel}(t) &= r_{max} \cdot (\rho(t+1) - \rho(t)) \\
\upsilon_{acc}(t) &= r_{max} \cdot (\rho(t+1) - 2\rho(t) + \rho(t-1)) \\
\upsilon_{dir}(t) &= r_{max} \cdot |\rho(t+1) - \rho(t)|_+
\end{aligned}
$$

where $r_{max} = 150$ Hz denotes the firing rate of a thalamic fiber when its associated feature property is at the fiber's preferred value. Transfer functions were randomly assigned to fibers with the fractions identified in Petersen et al. (2008) (Fig. 9A, 11% coding for position and acceleration, 58% for velocity and 20% for direction). The spiking process ψ was an adapting Markov process (Muller et al., 2007) with an adaptation time constant of 100 ms. As the whisker movements were short lasting, rates were evaluated at submillisecond (0.1) resolution.

Similarly to before, only the seven column subvolume (210k neurons) was used for the simulations, and the *in vivo*-like state was realized as $Ca^{2+} = 1.05$ mM, $R_{OU} = 0.4$, and $P_{FR} = 0.3$.

The optogenetic inhibition in this experiment targeted 95% (in line with (Varani et al., 2022)) of excitatory cells in layer 4. The authors found a few cells which also tested positive for Halo at the bottom of L3 as well, but as they did not quantify it, we decided not to target any lower L3 PCs in the *in silico* version of the experiment. Based on the 595 nm wavelength (yellow light) parameters were set to $\mu_a \approx 0.49\,mm^{-1}$ and $\mu'_s \approx 4.12\,mm^{-1}$. For the depth-based spatial binning of cells, 5 bins were used in L4. After scanning several values, I_0 was set to -200% as that reproduced the ≈ 10 mV hyperpolarization of L4 PCs observed *in vivo*. In line with the *in vivo* experiment, the optogenetic stimulus ended in a (100 ms long) ramp to avoid rebound spikes (Fig. 9B).

When going beyond reproducing the same experimental conditions and instead leveraging the *in silico* nature of our setup, synaptic pathways were lesioned by selecting the excitatory population in a given layer as the pre-synaptic population and the excitatory population in L2/3 as the post-synaptic population and not instantiating the connecting synapses during the simulation.

L2/3 PCs had to meet three criteria to be included in the subsequent analysis. Firstly, their activity was required to remain subthreshold during the 500 ms long whisker hold stimulus and in 200 ms long time windows before and after the stimulus, both in control and *in silico* optogenetic runs. Second, they had to be innervated by at least one (active) VPM fiber. Third, the derivative of their voltage trace had to cross the 1 mV/ms threshold in a 20 ms time window after stimulus onset in the control simulation. The last two were motivated by comparing subthreshold voltages to voltage traces from Varani et al. (2022) that showed large, stimulus evoked EPSPs. Around 8% of L2/3 PCs in the central column met all the above criteria and their voltages were averaged to arrive to the traces shown in Fig. 9E-F. Thus, unlike in the original analysis, cells rather than trials were averaged. The motivation for this approach is that while *in vivo* it is easier to repeat the same paradigm after establishing stable recording conditions in a given cell, *in silico* it is quicker to record from all cells in a single simulation, instead of repeating the stimulus several times.

Contrast tuning modulation by optogenetic activation of interneuron subtypes

We studied the effect of optogenetic activation of interneuron subtypes on contrast tuning in a similar way as described in a recent experimental study in anaesthetized mice (Shapiro et al., 2022). We ran a series of 14 simulations lasting 100 s each, with drifting grating patterns used as input stimuli to our model. We applied grating patterns with five different contrast levels in random order, each of which was presented 10 times within each simulation. A contrast stimulus was always presented for 1 s, followed by a 1 s (blank) inter-stimulus interval. At the same time, we optogenetically activated PV+ or Sst+ interneurons in the same region as targeted by the drifting gratings with six different depolarization strengths, including strength zero (i.e., no activation) as a baseline condition. All optogenetic stimuli lasted 1 s and were completely overlapping with all the grating stimulus intervals within a simulation, while keeping the interneuron subtype and depolarization level constant throughout a simulation. We then fitted sigmoidal functions to the observed contrast tuning responses and quantified the effects of optogenetic activation in the same way as described by Shapiro et al. (2022) by fitting saturation additive and conductance-based models to interneuron and PC responses respectively. More details can be found in the following subsections.

Drifting grating stimuli with different contrasts Since our model comprises the nbS1 and not the V1 brain area, we modelled visual drifting gratings in a more abstract way, without taking specifics of the visual system into account. In particular, we defined $\rho(x_\zeta, y_\zeta, t)$ as a spatio-temporal rate pattern corresponding to linear sinusoidal drifting gratings for a fraction F_P of 937 VPM fibers projecting to a single simulated column (30k neurons, 520 μm diameter). For all other VPM fibers ρ was zero. The gratings had a temporal frequency of $f_{temp} = 2\,\text{Hz}$ and a spatial frequency of 0.03 cycles/degree which we translated to $f_{spat} = 0.001\,\text{cycles}/\mu m$ by assuming a cortical magnification factor in rat of 30 μm/degree (Gias et al., 2005). In Fig. 10A, the spatial grating patterns are illustrated at

different points in time.

As in Shapiro et al. (2022), we used five contrast levels $C \in [0.06, 0.12, 0.24, 0.5, 1.0]$ which were defined as the Michelson contrast given the minimum and maximum luminance values L_{min} and L_{max}:

$$C(L_{min}, L_{max}) = \frac{L_{min} - L_{max}}{L_{min} + L_{max}} \tag{6}$$

Since the physical quantity of luminance does not have a clear correspondence in our model, we used normalized luminance values L_{min} and L_{max} between 0.0 and 1.0 by computing the inverse Michelson contrast centered around a mean normalized luminance of 0.5. The resulting values of L_{min} and L_{max} where then scaled and shifted to the minimum and maximum rates of the sinusoidal modulation R_{min} and R_{max} respectively such that the peak firing rate at contrast 1.0 was given by R_{peak} and the mean of the modulation corresponding to the background firing rate at contrast 0.0 was given by R_{bk}. The resulting sinusoidal input rate signal can be written as:

$$\rho_\zeta(t) = R(t, l_\zeta) = R_{min} + 0.5(R_{max} - R_{min})\Big[1 + \sin(2\pi\, f_{temp}\, t - 2\pi\, f_{spat}\, l_\zeta)\Big]\Big|_+ \tag{7}$$

where t is the time in seconds, l_ζ the linear position of ζ within the grating, and $|_+$ denotes that firing rates are truncated to positive values only. Fig. 10B illustrates a random series of rate signals corresponding to different contrasts. No transfer function was used, and spiking process ψ was an adapting Markov process (Muller et al., 2007) with an adaptation time constant of 100 ms. Values for F_P, R_{peak}, and R_{bk} were determined beforehand by a parameter optimization so that the resulting grating responses were qualitatively comparable with the ones reported by Shapiro et al. (2022), see next subsection for details.

Calibration of drifting grating stimulus We ran a parameter scan to determine optimal values for F_P (fraction of 937 VPM fibers projecting to the central column of our model to apply grating stimulus to), R_{peak} (peak firing rate at contrast 1.0), and R_{bk} (background firing rate at contrast 0.0). This calibration was done by running 45 simulations using all combinations of parameter values in the ranges $F_P \in [0.5, 0.75, 1.0]$, $R_{peak} \in [5.0, 10.0, 15.0, 20.0, 25.0]$ Hz and $R_{bk} \in [0.05, 0.1, 0.2]$ Hz, and selecting the optimal combination amongst them. Each simulation lasted 40 s during which 20 contrast stimuli were presented for 1 s, followed by a 1 s (blank) inter-stimulus interval. Four contrast levels $C \in [0.06, 0.12, 0.5, 1.0]$ were presented five times each in random order, which was sufficient to fit sigmoidal tuning functions with four parameters (see Eq. 9).

We observed that especially under strong stimulus conditions the response rates of PCs to the first and second cycle of the sinusoidal grating pattern (1 s stimulus at $f_{temp} = 2$ Hz) were quite different, with the second response largely attenuated due to synaptic depletion. Therefore, we extracted first and second peak firing rates r_1 and r_2 respectively from the peristimulus time histograms (PSTHs) computed with 1 ms resolution and 20 ms Gaussian smoothing (Fig. S6). We defined a measure of the normalized peak difference as the Michelson contrast of the peak rates r_1 and r_2, given by

$$\hat{r}_{diff} = \frac{r_1 - r_2}{r_1 + r_2} \tag{8}$$

Additionally, we extracted average firing rates for each contrast level of the whole population of PCs within the full (1 s) as well as the first and second halves (0.5 s each)

of the stimulation intervals. We then fitted sigmoidal tuning functions with parameters c_{50}, m, n, and R_{max} (see Eq. 9) to these average tuning responses (Fig. S7). Finally, as summarized in Fig. S6 and S7, we selected the best combination of parameters based on the following selection criteria:

- The peak firing rates in response to the grating stimulus should be sufficiently strong, covering a range of values including the one reported in (Shapiro et al., 2022, cf. Fig. 1D). So we imposed the constraint that the maximum peak rates over the whole population of PCs of the first and second peaks r_1 and r_2 respectively should be at least $r_{th} = 30\,\mathrm{Hz}$ at maximum contrast.
- The peak responses to the first and second cycle of the grating stimulus should not be too different. So we aimed for a low peak difference $\hat{r}_{diff}$ at maximum contrast.
- The overall tuning response of the PCs should be in a regime where the tuning curve would have a sigmoidal shape, meaning that it should be increasing but saturating with increasing contrasts. To fulfill this constraint, we aimed for
  - Low c_{50}, i.e., the inflection point of the tuning curve would be at low contrasts
  - High n, i.e., a steep non-linear increase of the tuning curve until saturation

In order to combine these criteria independent of the actual scales of $\hat{r}_{diff}$, c_{50} and n, we computed their individual rank scores in decreasing ($\hat{r}_{diff}$, c_{50}: lower is better) or increasing (n: higher is better) order. We then selected the parameter combination with the highest product of rank scores, excluding the ones with peak firing rates r_1 and r_2 below r_{th} and the ones with c_{50} values close to 1.0 (border cases). We found an optimal parameter combination of $F_P = 1.0$, $R_{peak} = 10.0\,\mathrm{Hz}$, and $R_{bk} = 0.20\,\mathrm{Hz}$ which we used throughout this *in-silico* experiment.

Optogenetic stimulation Optogenetic stimulation was targeted at either 1654 PV+ or 822 Sst+ interneurons in a single column. We used parameters $\mu_a \approx 0.46\,\mathrm{mm}^{-1}$ and $\mu_s' \approx 5.38\,\mathrm{mm}^{-1}$, based on the wavelength of 470 nm (blue light; see Fig. S2). I_0 was increased from 0% to 300% in steps of 50%.

Quantification of contrast tuning responses by sigmoidal functions We quantified contrast tuning responses in the same way as described by Shapiro et al. (2022), by least-squares fitting sigmoidal functions to the normalized tuning curves. Normalized tuning curves were obtained by computing the time-averaged firing rates of all 1 s stimulus intervals and dividing them by the mean baseline firing rate (i.e., w/o optogenetic stimulation) at the highest contrast level. The sigmoidal function was given by

$$R(c) = \frac{R_{max}\, c^n}{c^n + c_{50}^n} + m \tag{9}$$

where $R(c)$ describes the response amplitude at contrast c, m is the baseline response at minimum contrast, R_{max} is the maximum increase above baseline, n defines the steepness of the curve, and c_{50} is the contrast at half R_{max}. We used the coefficient of determination (r^2 score) as a measure of the goodness of fit.

Detection of neurons with robust contrast tuning We identified PV+, Sst+, and pyramidal neurons with robust contrast tuning behavior under all conditions. In the experimental study of Shapiro et al. (2022), tetrode recordings were used together with spike sorting. Correspondingly, we only considered neurons firing at rates above 0.5 Hz under all stimulus conditions, meaning they could potentially be detected by spike sorting (Pedreira et al., 2012). In addition, we considered neurons as being robustly tuned if they had strictly monotonically increasing tuning curves.

Modelling the effects of optogenetic stimulation of interneurons Direct photostimulation effects on interneurons were modelled by a divisive scaling model $R_{div}(c)$, a subtractive shifting model $R_{sub}(c)$, or a saturation additive model $R_{sat}(c)$ (Shapiro et al., 2022). For fitting these models, the parameters c_{50}, m, n, and R_{max} of the underlying contrast tuning function $R(c)$ were kept constant at values obtained from baseline fits (i.e., w/o optogenetic stimulation). The divisive scaling model was defined as

$$R_{div}(c) = R(c)/g \tag{10}$$

with a scaling term g. The subtractive shifting model was given by

$$R_{sub}(c) = R(c) - h \Big|_{+} \tag{11}$$

with a shifting term h and rectification to rates equal or above zero. The saturation additive model was defined as

$$R_{sat}(c) = R(c) + \frac{S\, c^{-n}}{c^{-n} + c_{50}^{-n}} + A \tag{12}$$

with a saturation term S and an additive term A. We used the r^2 score to measure the goodness of model fits.

Indirect effects on PCs receiving inhibitory input from optogenetically activated interneurons were modelled by a conductance-based model $R_{cond}(c)$, assuming a saturating additive model description of interneurons (Shapiro et al., 2022). Response rates under this conductance-based model were given by

$$R_{cond}(c) = \Big[\Delta V(c) - V_{th}\Big]^3 \Big|_{+} \tag{13}$$

with a spike threshold $V_{th} = 3.4\,\mathrm{mV}$ and rectification to rates equal or above zero. The membrane potential $\Delta V(c)$ as a function of contrast was given by

$$\Delta V(c) = \frac{g_L\, R_L + g_E(c)\, R_E + g_I(c)\, R_I}{g_L + g_E(c) + g_I(c)} - V_r \tag{14}$$

with values for leak conductance $g_L = 6\,\mathrm{nS}$, leak reversal potential $R_L = -50\,\mathrm{mV}$, excitatory reversal potential $R_E = 0\,\mathrm{mV}$, inhibitory reversal potential $R_I = -65\,\mathrm{mV}$, and resting potential $V_r = -50\,\mathrm{mV}$ as reported by Shapiro et al. (2022). The excitatory synaptic conductance was given by

$$g_E(c) = \frac{g_{E_max}\, c^n}{c^n + c_{50}^n} + g_{E_min} \tag{15}$$

with the excitatory conductances at low/high contrast given by g_{E_min} and g_{E_max} respectively. The inhibitory synaptic conductance was given by

$$g_I(c) = g_E(c) + \frac{S\,c^{-n}}{c^{-n} + c_{50}^{-n}} + \Delta g_{IE_min} + A \tag{16}$$

with an inhibitory conductance offset $\Delta g_{IE_min} = 2\,\text{nS}$ at low contrast relative to g_{E_min}.

In a first step, parameters S and A were set to zero and the model parameters $c50$, g_{E_min}, g_{E_max}, and n were fit to baseline responses of PCs. In a second step, those parameter values were kept constant and the model parameters S and A were fit to PC responses under photostimulation conditions. Again, we used the r^2 score to measure the goodness of model fits.

Tuning of inhibitory sub-types to synchronous and rate-coded signals

We also compared the *in vivo* state of our model with the results of a recent *in vitro* study (Prince et al., 2021), which explored how neurons with different biophysical properties encode different types of signals. The *in vitro* study optically activated groups of 10 PCs in slices of L2/3 barrel cortex from mouse lines labelling fast-spiking (FS) and regular-spiking (RS) interneurons. Each PC was targeted individually and a binary signal was encoded either through changes in the rate of optical pulses applied to the 10 stimulus neurons, or through changes in the synchronicity of the pulses. The mutual information shared between the binary signal (when encoded either as changes in firing rate or synchronicity) and the firing rate of different inhibitory sub-types (recorded using whole-cell patch clamping *in vitro*) was analysed.

While the *in vitro* stimuli used optical pulses targeted at single neurons with timings drawn from Poisson processes, it was not necessary to explicitly model such an optical stimulus *in silico*, as we can instead elicit spikes directly in the model. In the original study, the 10 stimulus neurons were uniformly separated in a grid-like pattern at horizontal and vertical distances of $\sim 50\,\mu m$. The binary signal alternated between two states at random intervals of 2-7 s. For the rate coding paradigm, the timings of the optical pulses for the 10 stimulus neurons were drawn from 10 independent inhomogeneous Poisson processes, with the rates of optical activation varying between 5 Hz and 0.5 Hz for the up and down states respectively (average firing rate: 2.7 Hz). For the synchronous case, the timings of the optical pulses for the 10 stimulus neurons were drawn from a single inhomogeneous Poisson process during the up state, or 10 independent inhomogeneous Poisson processes during the down state. For the synchronous case, the firing rates of the up and down state were both 2.7 Hz. We therefore tested stimulus encoding using a range of stimulus neuron counts: from 10 to 1,000.

In our interpretation of the study, mutual information was measured between the binary signal and neural activity during a 0-5 ms and 5-50 ms window following a change in the signal. These represented 'early' and 'late' stimulus encoding windows following the change in the signal, respectively. As the synchronous up state activated synchronous patterns at a rate of 2.7 Hz, we calculated that a synchronous pattern would only be activated during the early and late windows with probability 0.0135 ($= 2.7 * 5/1000$) and 0.1125 ($= 2.7 * 45/1000$) respectively. We therefore chose to use higher FR of 20 Hz for the synchronous up and down states, and to analyse mutual information between the

binary signal and all 50 ms bins. To afford comparison with the rate code experiment type, we used 30 Hz and 10 Hz as the FRs of the up and down states respectively. We also compare stimulus coding during the first 50 ms following the stimulus change for both the synchronous and rate stimulus types.

Analysis of long-range connectivity and correlations between subvolumes

We split the neurons in the model into hexagonal subvolumes of a specified diameter d considering their locations in a flattened view (Bolaños-Puchet and Reimann, prep) . We then counted the number of long-range connections within and between the hexagonal subvolumes, yielding in S, the adjacency matrix of the resulting directed graph. Distances between hexagonal subvolumes were calculated by considering the centers of the hexagons in the flattened view. We also calculated the correlations of spiking activity of pairs of hexagonal subvolumes: We pooled all spikes within a hexagonal subvolume and counted their number in 5 ms time bins; then calculated the Pearson correlation of the resulting time series. The correlation within a hexagonal subvolume was calculated similarly, but using the separate time series of the excitatory and inhibitory populations. Together, this yielded F, the matrix of correlations of subvolumes.

Based on S and F we calculated the expected correlations of long-range inputs as follows: Let i be a hexagonal subvolume and S_i the column of S associated with input counts into i. Then $P = S_i \cdot S_i^\top$ is in the matrix of counts of pairs of inputs for all pairs of hexagonal subvolumes. Combining P and F allows us to estimate the distribution of correlations of long-range inputs into i, albeit at the population rather than single-cell level.

For the correlation in Fig. 12A2, H, J1 a hexagon size of $400\mu m$ was used; in Fig. 12I2 a smaller size of only $50\mu m$ was used.

Node participation

Given a connectivity graph G, a directed n-simplex in G is a set of $n+1$ nodes which are all all-to-all connected in G in a feed-forward fashion, i.e., such that any subset of these has a unique source and a unique sink (see Reimann et al. (2017) for more details). The *n-node participation* of a node v in G is the number of directed n-simplices this node is part of. In particular, for $n = 1$, this is the total degree of the node in G. Thus, this can be though of a generalization of the notion of degree that takes into account account higher order interactions and has been shown to strongly correlate with other node centrality metrics Sizemore et al. (2018).

Supplementary Tables and Figures

Table S1: **Excitatory synaptic pathways.** Average class parameters are marked in bold and are used predictively (in lack of reference *in vitro* data) for the remaining pathways belonging to the same class. Physical dimensions are as follows: peak conductance $\hat{g}$: nS, depression and facilitation time constants D, F, and the EPSC τ_{decay}: ms, the Hill coefficient of the nonlinear, $[Ca^{2+}]_o$ dependent scaling of release probability U_{Hill}: mM, the release probability U_{SE}, the average number of vesicles in the release-ready pool N_{RRP}, and the NMDA/AMPA ratio $\hat{g}_{ratio}$ are dimensionless.

Pre	**Post**	$\hat{g}$	U_{SE}	D	F	N_{RRP}	τ_{decay}	$\hat{g}_{ratio}$	U_{Hill}
				PC to Sst+IN (E1)					
PC	MC	0.2±0.1	0.09±0.12	138±211	670±830	1.5	1.74±0.18	0.8	2.79
PC	**PT**	**0.6±0.5**	**0.02±0.00**	**194±18**	**507±37**	**4.5**	**1.74±0.18**	**0.8**	**1.09**
PC	**DT**	**0.2±0.1**	**0.02±0.00**	**194±18**	**507±37**	**1.5**	**1.74±0.18**	**0.8**	**2.79**
				PC to PC (E2)					
L23_PC	L23_PC	1.0±0.5	0.46±0.26	671±17	17±5	2.6	1.74±0.18	0.7	2.79
L4_PC	L4_PC	0.6±0.3	0.86±0.09	671±17	17±5	1.0	1.74±0.18	0.9	2.79
L4_SSC	L23_PC	0.2±0.1	0.79±0.04	671±17	17±5	1.8	1.74±0.18	0.5	2.79
L5_STPC	L5_STPC	0.9±0.3	0.39±0.03	690±90	44±21	1.0	1.74±0.18	0.7	2.79
L5_TTPC	L5_TTPC	1.9±1.0	0.38±0.10	365±100	25±45	2.8	1.74±0.18	0.7	2.79
L23_PC	L5_TTPC	0.5±0.2	0.50±0.02	671±17	17±5	1.5	1.74±0.18	0.7	2.79
L4_SSC	L5_STPC	0.6±0.3	0.50±0.02	671±17	17±5	1.2	1.74±0.18	0.7	2.79
L4_SSC	L6_PC	0.4±0.2	0.50±0.02	671±17	17±5	1.0	1.74±0.18	0.7	2.79
L6_TPC:A	L6_TPC:A	1.0±0.5	0.37±0.11	280±90	90±80	1.0	1.74±0.18	0.7	2.79
L6_TPC:C	L6_TPC:C	0.5±0.2	0.23±0.06	420±340	200±130	1.0	1.74±0.18	0.7	2.79
L6_IPC	L6_IPC	0.9±0.3	0.23±0.06	420±340	200±130	1.0	1.74±0.18	0.7	2.79
L6_PC to same L6_PC		**0.8±0.2**	**0.23±0.06**	**420±340**	**200±130**	**1.0**	**1.74±0.18**	**0.7**	**2.79**
L6_TPC:A	L6_TPC:C	1.2±0.5	0.23±0.06	420±340	200±130	1.0	1.74±0.18	0.7	2.79
L6_TPC:A	L6_BPC	0.3±0.1	0.23±0.06	420±340	200±130	1.0	1.74±0.18	0.7	2.79
L6_TPC:C	L6_IPC	0.2±0.1	0.23±0.06	420±340	200±130	1.0	1.74±0.18	0.7	2.79
L6_IPC	L6_BPC	0.4±0.1	0.23±0.06	420±340	200±130	1.0	1.74±0.18	0.7	2.79
L6_BPC	L6_TPC:A	0.2±0.1	0.23±0.06	420±340	200±130	1.0	1.74±0.18	0.7	2.79
L6_PC to diff. L6_PC		**0.5±0.4**	**0.23±0.06**	**420±340**	**200±130**	**1.0**	**1.74±0.18**	**0.7**	**2.79**
PC	**PC**	**0.7±0.4**	**0.50±0.02**	**671±17**	**17±5**	**1.5**	**1.74±0.18**	**0.7**	**2.79**
				PC to Sst-IN (E2)					
PC	NBC	0.6±0.4	0.72±0.12	227±70	13±24	4.5	1.74±0.18	0.8	1.09
PC	**PT**	**0.6±0.5**	**0.50±0.02**	**671±17**	**17±5**	**4.5**	**1.74±0.18**	**0.8**	**1.09**
PC	L1_GABAB-	0.3±0.1	0.50±0.02	671±17	17±5	1.5	1.74±0.18	0.8	1.94
L6_TPC:A	L6_BC	0.4±0.1	0.58±0.13	240±80	70±90	1.5	1.74±0.18	0.8	1.09
L6_TPC:C	L6_BC	0.4±0.1	0.36±0.21	380±310	280±340	1.5	1.74±0.18	0.8	1.09
L6_IPC	L6_BC	0.3±0.1	0.51±0.20	440±300	100±50	1.5	1.74±0.18	0.8	1.09
L6_PC	**L6_BC**	**0.4±0.1**	**0.47±0.21**	**370±290**	**155±215**	**1.5**	**1.74±0.18**	**0.8**	**1.09**
PC	**IN**	**0.4±0.1**	**0.50±0.02**	**671±17**	**17±5**	**1.5**	**1.74±0.18**	**0.8**	**1.94**

Proximal Targeting inhibitory mtypes: N/L/SBC, CHC. N/LBC etypes: cACint, cIR, bAC, bIR, cNAC have E1, while the rest of etypes; and SBC and CHC mtypes have E2 short-term dynamics.
Distal Targeting inhibitory mtypes: BP, DBC, BTC. L1_GABAB- comprise all non NGC mtypes in L1

Table S2: **Inhibitory synaptic pathways.** Average class parameters are marked in bold and are used predictively (in lack of reference *in vitro* data) for the remaining pathways belonging to the same class. Physical dimensions are as follows: peak conductance $\hat{g}$: nS, depression and facilitation time constants D, F, and the IPSC τ_{decay}: ms, the Hill coefficient of the nonlinear, $[Ca^{2+}]_o$ dependent scaling of release probability U_{Hill}: mM, the release probability U_{SE}, the average number of vesicles in the release-ready pool N_{RRP}, and the $GABA_B/GABA_A$ ratio $\hat{g}_{ratio}$ are dimensionless.

Pre	**Post**	$\hat{g}$	U_{SE}	D	F	N_{RRP}	τ_{decay}	$\hat{g}_{ratio}$	U_{Hill}
				IN to PC (I1)					
L6_BC	L6_BC	2.3±0.5	0.16±0.10	45±21	376±253	1.0	10.40±6.20	0.0	1.94
SBC (cACint)	PC	1.9±1.0	0.16±0.10	45±21	376±253	3.3	10.40±6.20	0.0	1.94
				IN to PC and IN (I2)					
MC	PC	3.0±1.5	0.30±0.08	1250±520	2±4	1.0	8.30±2.20	0.0	1.94
DT	**PC**	**3.0±1.5**	**0.25±0.13**	**706±405**	**21±9**	**1.0**	**8.30±2.20**	**0.0**	**1.94**
NBC	PC	1.9±1.0	0.14±0.05	875±285	22±5	3.3	8.30±2.70	0.0	1.94
NGC	PC	0.2±0.1	0.25±0.13	706±405	21±9	1.0	36.50±1.30	0.8	1.94
L1_GABAB-	PC	0.3±0.1	0.25±0.13	706±405	21±9	1.0	8.30±2.20	0.0	1.94
SBC (dNAC)	PC	1.9±1.0	0.25±0.13	706±405	21±9	3.3	8.30±2.20	0.0	1.94
IN	*****	**2.3±0.5**	**0.25±0.13**	**706±405**	**21±9**	**1.0**	**8.30±2.20**	**0.0**	**1.94**
				IN to PC (I3)					
L6_BC	L6_PC	1.9±1.0	0.44±0.25	195±190	200±320	1.0	10.40±6.20	0.0	1.94
PT	**PC**	**1.9±1.0**	**0.32±0.14**	**144±80**	**62±31**	**3.3**	**6.40±1.70**	**0.0**	**1.94**

Proximal Targeting inhibitory mtypes: N/L/SBC, CHC. N/LBC etypes: cNAC, dSTUT, cSTUT, bSTUT have I3, while the rest of etypes; and SBC (except: cACint and dNAC) and CHC mtypes have I2 short-term dynamics. Distal Targeting inhibitory mtypes: BP, DBC, BTC. L1_GABAB- comprise all non NGC mtypes in L1

Table S3: **Thalamocortical synaptic pathways.** Values taken from the internal connectivity (Table S1) are marked in bold. Physical dimensions are the same as in Table S1.

Pre	**Post**	$\hat{g}$	U_{SE}	D	F	N_{RRP}	τ_{decay}	$\hat{g}_{ratio}$	U_{Hill}
				VPM, POm to Sst+IN (E1)					
*	Sst+	**0.2±0.1**	**0.09±0.12**	**138±211**	**670±830**	**1.5**	**1.74±0.18**	**0.8**	**2.79**
				VPM, POm to PC (E2)					
VPM	L23_PC	1.7±0.6	0.75±0.1	**671±17**	**17±5**	**1.5**	**1.74±0.18**	**0.7**	**2.79**
VPM	L4_PC	1.1±0.4	0.75±0.1	**671±17**	**17±5**	**1.5**	**1.74±0.18**	**0.7**	**2.79**
VPM	L56_PC	2.4±0.9	0.75±0.1	**671±17**	**17±5**	**1.5**	**1.74±0.18**	**0.7**	**2.79**
POm	PC	1.7±0.6	0.75±0.1	**671±17**	**17±5**	**1.5**	**1.74±0.18**	**0.7**	**2.79**
				VPM, POm to PV+IN (E2)					
VPM	L4_PV+	1.4±0.4	**0.72±0.12**	**227±70**	**13±24**	**4.5**	**1.74±0.18**	**0.8**	**1.09**
VPM	L6_PV+	3.1±1.0	**0.72±0.12**	**227±70**	**13±24**	**4.5**	**1.74±0.18**	**0.8**	**1.09**
VPM	L235_PV+	2.2±0.4	**0.72±0.12**	**227±70**	**13±24**	**4.5**	**1.74±0.18**	**0.8**	**1.09**
POm	PV+	2.2±0.4	**0.72±0.12**	**227±70**	**13±24**	**4.5**	**1.74±0.18**	**0.8**	**1.09**
				VPM, POm to 5HT3aR+IN (E2)					
*	5HT3aR+	**0.4±0.1**	**0.50±0.02**	**671±17**	**17±5**	**1.5**	**1.74±0.18**	**0.8**	**1.94**

Sst+ inhibitory mtypes: MC and BP, DBC, BTC (cACint etype only). PV+ inhibitory mtypes: N/LBC, CHC. 5HT3aR+ mtypes: the rest of the mtypes not listed above (e.g. NGC, SBC, and everything in L1).

Table S4: Validation of PSP amplitudes (see Figure 3B1)

Pre	**Post**	*in vitro* (mV)	*in silico* (mV)	Reference
L23_PC	L23_PC	1.00±0.70	0.99±0.67	Feldmeyer et al. (2006)
L23_PC	L5_TTPC	0.30±0.30	0.30±0.24	Reyes and Sakmann (1999)
L4_EXC	L4_EXC	1.59±1.51	1.62±1.31	Feldmeyer et al. (1999)
L4_SSC	L23_PC	0.70±0.60	0.66±0.34	Feldmeyer et al. (2002)
L4_SSC	L5_STPC	0.60±0.40	0.59±0.33	Feldmeyer et al. (2005)
L4_SSC	L6_PC	0.29±0.16	0.30±0.30	Qi and Feldmeyer (2016)
L5_TTPC	L5_TTPC	1.30±1.10	1.24±0.73	Markram et al. (1997a)
L5_STPC	L5_STPC	0.80±0.20	0.75±0.40	Le Bé et al. (2007)
L6_BPC	L6_TPC:A	0.21±0.00	0.22±0.15	Berger (2009)
L6_IPC	L6_BPC	0.42±0.18	0.42±0.21	Berger (2009)
L6_IPC	L6_IPC	1.05±0.31	1.09±0.81	Berger (2009)
L6_TPC:C	L6_IPC	0.18±0.00	0.19±0.13	Berger (2009)
L6_TPC:C	L6_TPC:C	0.43±0.22	0.43±0.29	Berger (2009)
L6_TPC:A	L6_BPC	0.32±0.27	0.31±0.17	Berger (2009)
L6_TPC:A	L6_TPC:C	1.19±0.15	1.10±0.63	Berger (2009)
L6_TPC:A	L6_TPC:A	1.51±0.98	1.45±1.11	Berger (2009)
L23_PC	L1_GABAB-	1.10±0.30	1.09±0.83	Wozny and Williams (2011)
L4_EXC	L4_FS	2.20±2.20	2.17±2.46	Beierlein et al. (2003)
L5_TTPC	L5_MC	0.28±0.30	0.28±0.33	Silberberg and Markram (2007)
L6_IPC	L6_BC	1.59±1.60	1.56±1.48	Berger (2009)
L6_TPC:A	L6_BC	2.20±3.28	2.02±1.44	Berger (2009)
L6_TPC:C	L6_BC	1.29±1.65	1.28±0.84	Berger (2009)
L6_PC	L6_MC	0.20±0.12	0.15±0.14	Berger (2009)
L1_NGC	L23_PC	0.58±0.10	0.54±0.41	Wozny and Williams (2011)
L1_GABAB-	L23_PC	0.27±0.04	0.26±0.13	Wozny and Williams (2011)
L4_FS	L4_EXC	1.10±0.80	1.14±0.81	Beierlein et al. (2003)
L5_MC	L5_TTPC	0.50±0.40	0.47±0.25	Silberberg and Markram (2007)
VPM	L4_EXC	2.40±2.00	2.51±2.10	Beierlein et al. (2003)
VPM	L4_FS	4.10±3.20	4.09±2.52	Beierlein et al. (2003)
VPM	L6_EXC	1.20±0.80	1.28±1.96	Beierlein and Connors (2002)
VPM	L6_FS	3.90±3.50	3.11±2.57	Beierlein and Connors (2002)

Thick-tufted mtypes: L5_TPC:A, L5_TPC:B. Slender-tufted mtypes: L5_TPC:C, L5_UPC.

Table S5: Validation of first PSP amplitudes' CVs (see Figure 3B2)

Pre	**Post**	*in vitro* (mV)	*in silico* (mV)	Reference
L4_EXC	L4_EXC	0.37±0.16	0.25±0.06	Feldmeyer et al. (1999)
L4_EXC	L4_FS	0.27±0.13	0.38±0.25	Beierlein et al. (2003)
L4_FS	L4_EXC	0.25±0.11	0.28±0.09	Beierlein et al. (2003)
L4_SS	L5_STPC	0.33±0.20	0.43±0.06	Feldmeyer et al. (2005)
L4_SS	L6_PC	0.50±0.11	0.51±0.06	Qi and Feldmeyer (2016)
L4_SS	L23_PC	0.27±0.13	0.32±0.07	Feldmeyer et al. (2002)
L5_TTPC	L5_TTPC	0.31±0.14	0.39±0.09	Barros-Zulaica et al. (2019)
L5_STPC	L5_STPC	0.58±0.24	0.51±0.06	Le Bé et al. (2007)
L23_PC	L23_PC	0.33±0.18	0.43±0.15	Feldmeyer et al. (2006)
L234_PC	L234_NBC	0.32±0.08	0.21±0.08	Wang et al. (2002)

Thick-tufted mtypes: L5_TPC:A, L5_TPC:B. Slender-tufted mtypes: L5_TPC:C, L5_UPC.

Table S6: Validation of mPSC frequency (see Figure 3E2)

Pre	**Post**	*in vitro* (Hz)	*in silico* (Hz)	Reference
E	L23_PC	8.20±2.90	9.36±4.38	Brasier and Feldman (2008)
E	L4_PC	11.90±2.40	15.64±7.84	Brasier and Feldman (2008)
E	L6_CC	2.80±0.80	3.87±2.14	Yang et al. (2020)
E	L6_CT	0.95±0.36	1.41±0.74	Yang et al. (2020)
I	L5_PC	21.10±4.80	16.06±6.74	Ling and Benardo (1999)
Cortico-cortical mtypes: L6_UPC, L6_IPC, L6_HPC.				
Cortico-thalamic mtypes: L6_TPC:A, L6_TPC:C.				

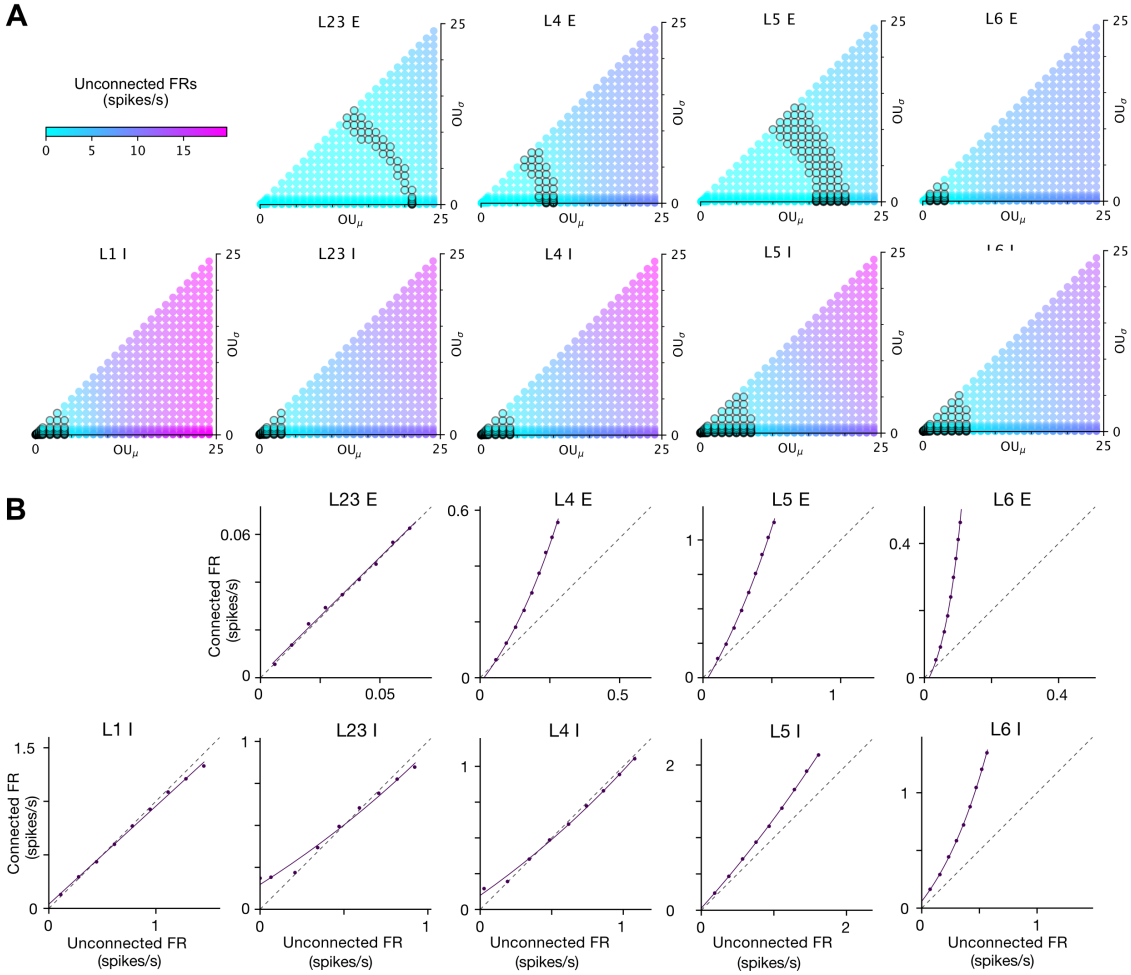

Figure S1: **Spontaneous activity calibration: estimating χ and ϕ.** **A**: Population unconnected FRs from unconnected simulations of a single column. Simulations vary by OU_μ and OU_σ. Colour shows FR. Black circles show region where FRs are greater than 0 and less than the population's *in vivo* reference FR. The dependence of unconnected FR on OU_μ and OU_σ is heterogeneous across populations. **B**: Final estimation of $\phi_{1.1,0.4}$ for each neuron group. Exponential fit of unconnected vs connected FRs for each population after 5th iteration. The final fits are heterogeneous across populations.

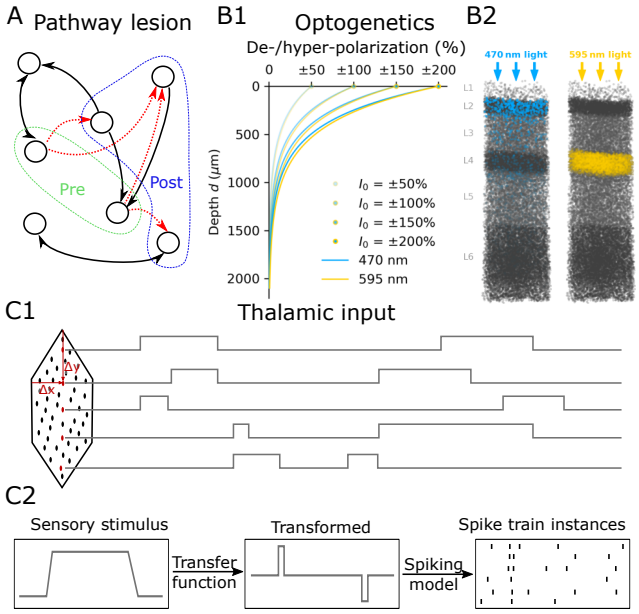

Figure S2: ***In silico* experimental methods.** **A:** Synaptic pathway lesions. After selecting a pre- (green) and post-synaptic (blue) population of neurons, connections between them in the specified direction are removed (red arrows). **B:** Optogenetic manipulations. **B1:** Decay with depth of the strength of a stimulus applied to mimic the effect of optogenetic manipulations with 470 nm (blue) and 595 nm (yellow) light. Indicated for exemplary intensities (values of I_0). **B2:** Targeted neuronal populations in two *in silico* optogenetic experiments. Density of affected cells (combination of expression level and light depth) indicated by the corresponding color of light. Unaffected populations in grey. Left: Excitation of inhibitory populations. Right: Inhibition of PCs in L4. **C:** Stimulation with thalamic inputs. **C1:** Each thalamic fiber in the model is assigned a position in a flat coordinate system. Based on the coordinates, type of fiber (VPM vs. POm), or randomly, time series of sensory stimulation are assigned to the fibers. **C2:** Sensory stimuli are transformed by a transfer function capturing pre-thalamic processing. The transfer function can simply be identity. The transformed signal is then used with a spiking model to generate stochastic spike trains that serve as inputs into a simulation.

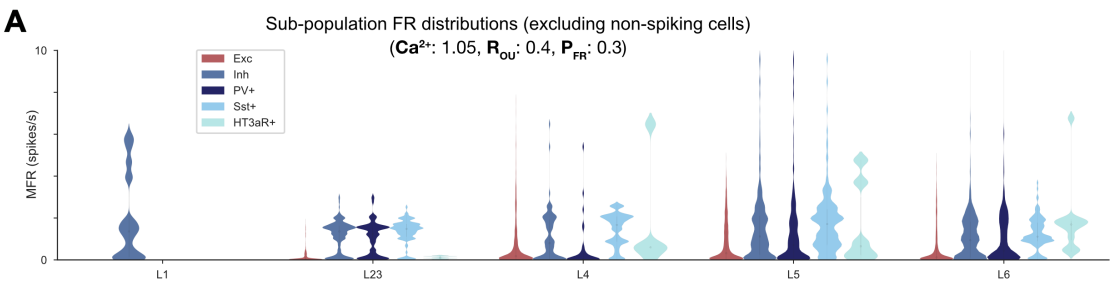

Figure S3: **Firing rate distributions.** **A**: Firing rate distributions of different subpopulations for the one of the parameter combinations. Non-spiking cells are excluded for improved visualisation of the distributions.

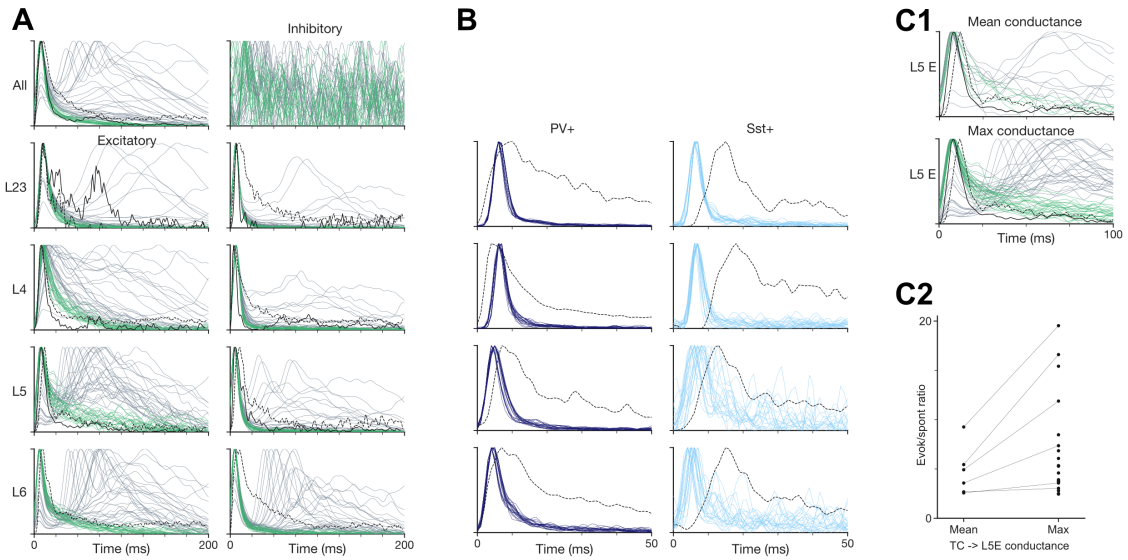

Figure S4: **Whisker deflection responses - supplementary.** **A:** PSTHs in response to the single whisker deflection stimulus for all parameter combinations. PSTHs of simulations which passed the initial criteria are coloured green, whilst those which did not are coloured grey. **B:** Layer-wise PV+ and Sst+ subpopulation PSTHs for simulations which passed the criteria. **C:** Analysis of evoked responses of L5 E under two simulation cases. The first case uses the mean of the VPM to L4 E and L6 E synaptic conductance for the VPM to L5 E conductance, whilst the second uses the maximum of the two values (VPM to L6 E). **C1:** For the two simulation cases, L5 E PSTHs for the criteria passing (green) and failing (grey) simulations. For the mean case, some of the simulations that do not burst or do not have a secondary rebound, fail the criteria because of low signal to noise. **C2:** Ratios between evoked and spontaneous activity of L5 E population for criteria passing simulations. There are fewer criteria passing simulations for the mean case, and those that do are much lower than the *in vivo* reference (40.2).

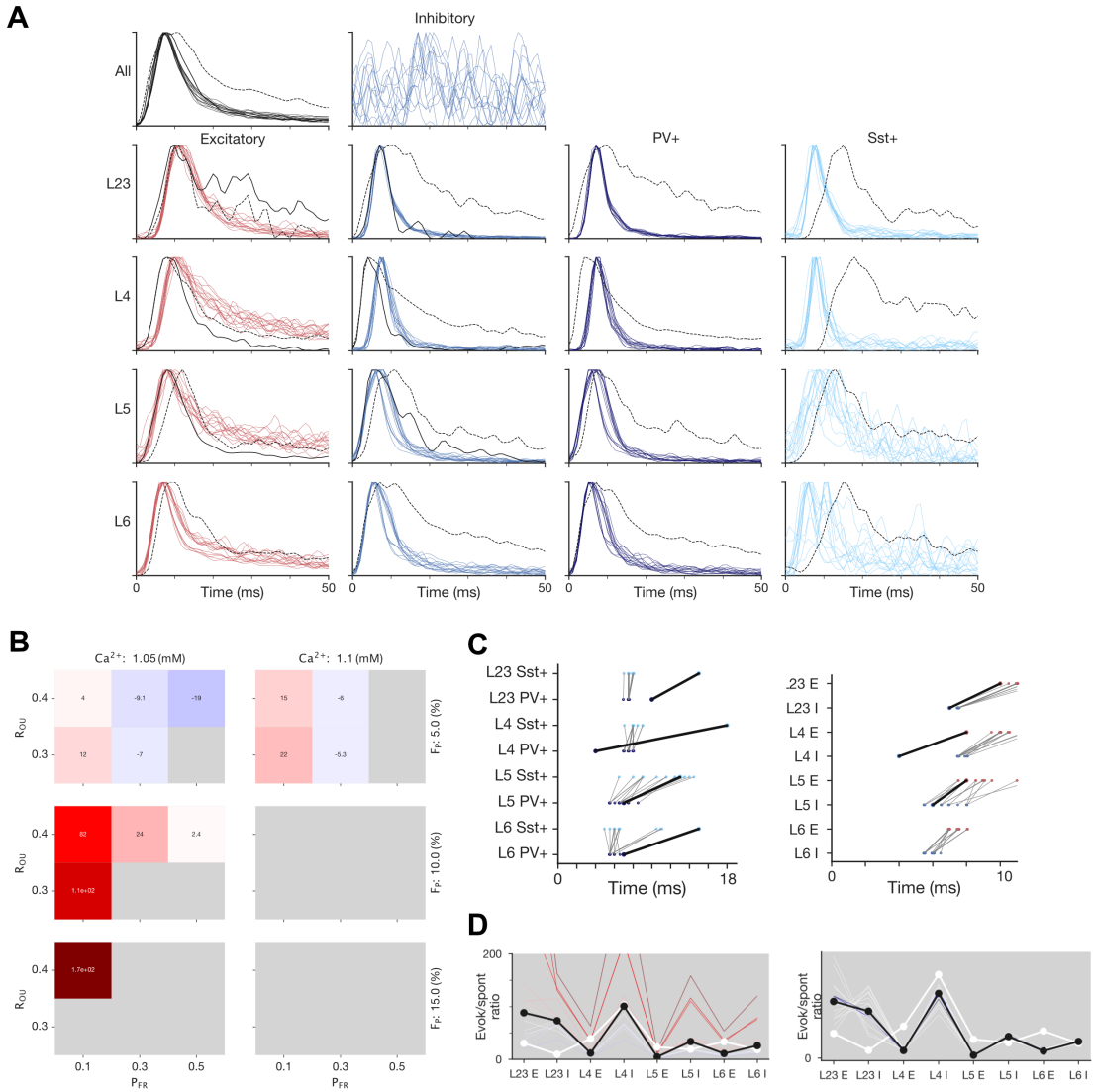

Figure S5: **Active whisker touch responses - supplementary**: Same as Fig. 8 but using a VPM stimulus and *in vivo* reference for the active whisker touch paradigm (see Methods).

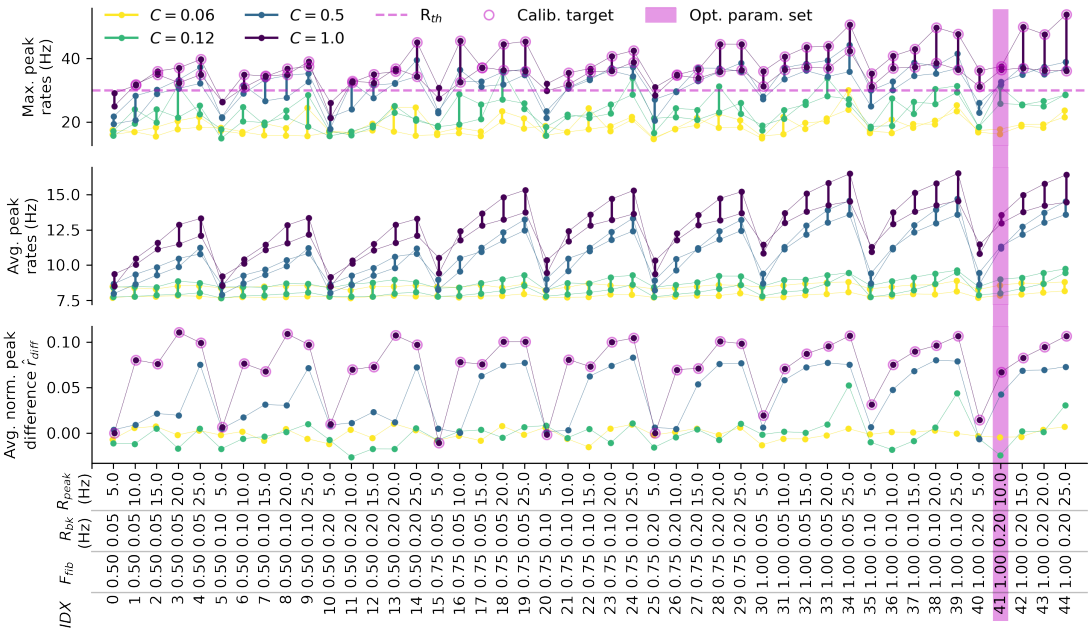

Figure S6: **Calibration of the drifting grating stimulus based on peak firing rates.** The drifting grating stimulus was calibrated by running a parameter scan of 45 simulations to determine optimal values for F_P, R_{bk}, and R_{peak}. The maximum (top) and average (middle) of the first and second peak firing rates r_1 and r_2 (connected points) over the whole population of PCs, together with the average of the normalized peak difference (Michelson contrast) $\hat{r}_{diff}$ (bottom) are summarized. Different colors indicate different contrast levels $C \in [0.06, 0.12, 0.5, 1.0]$. The rate threshold $r_{th} = 30\,\text{Hz}$ at maximum contrast, the calibration target values that were taken into account for selecting the optimal parameter set, as well as the optimal parameter set ($F_P = 1.0$, $R_{bk} = 0.2\,\text{Hz}$, and $R_{peak} = 10.0\,\text{Hz}$), are highlighted.

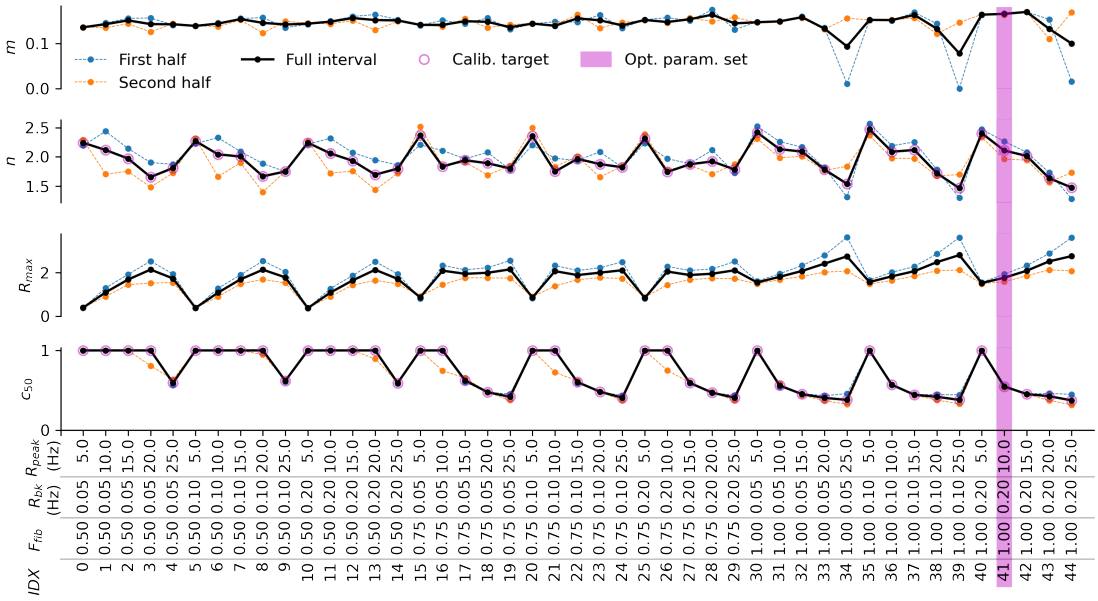

Figure S7: **Calibration of the drifting grating stimulus based on sigmodal parameters.** The drifting grating stimulus was calibrated by running a parameter scan of 45 simulations to determine optimal values for F_P, R_{bk}, and R_{peak}. The values of the four parameters m, n, R_{max}, and c_{50} for fitting a sigmoidal function to the average firing rates of the whole population of PCs within the full stimulation interval are summarized. Dashed lines indicate fitted parameter values when considering only the first or second half of the response interval. Calibration target values that were taken into account for selecting the optimal paramter set, as well as the optimal parameter set ($F_P = 1.0$, $R_{bk} = 0.2\,\mathrm{Hz}$, and $R_{peak} = 10.0\,\mathrm{Hz}$), are highlighted.

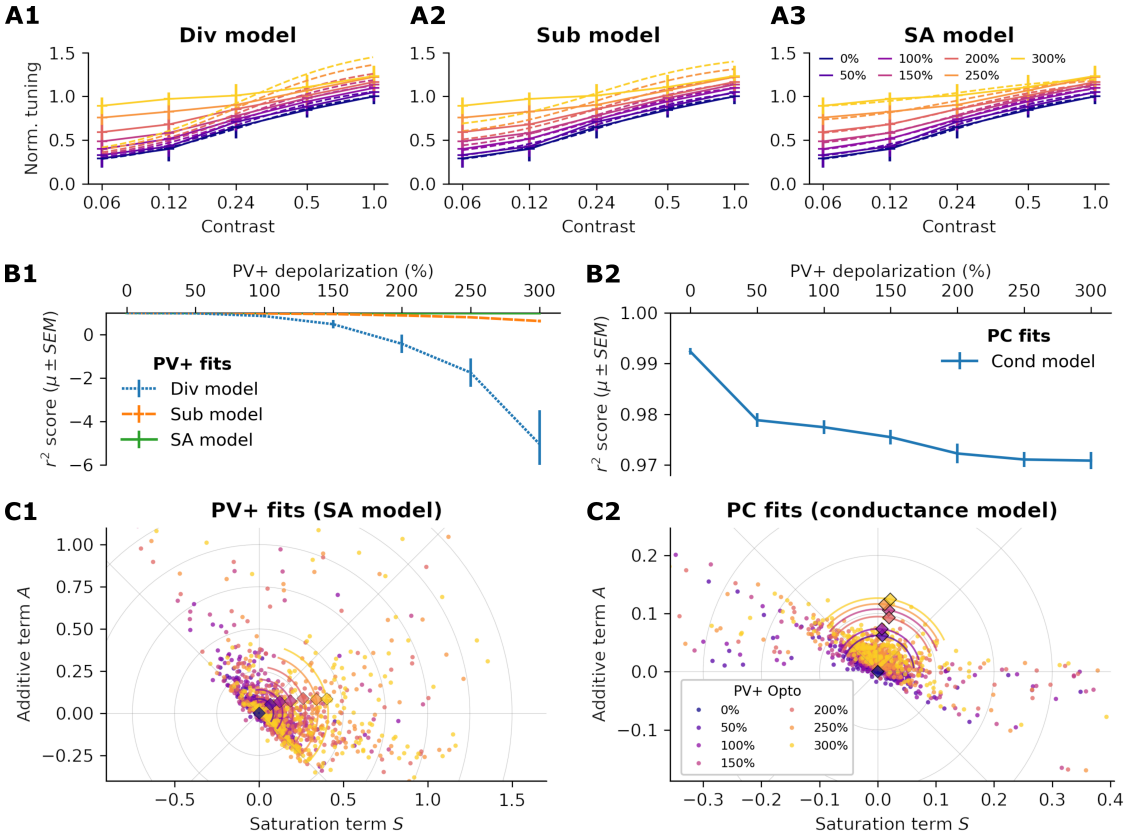

Figure S8: **Modelling the effects of optogenetic stimulation of interneurons. A1-A3:** Divisive scaling (Div), subtractive shifting (Sub), and saturation additive (SA) model fits (dashed lines) to responses of an exemplary PV+ interneuron (solid lines) at different levels of PV+ optogenetic stimulation, ranging from 0% (baseline) to 300%. **B1:** Goodness of Div/Sub/SA model fits ($\mu \pm SEM$ of r^2 score) for different depolarization levels over all 259 robustly tuned PV+ interneurons, showing that direct photostimulation effects on interneurons can be best described by the saturation additive model. **C1:** Polar plot of S (saturation) and A (additive) parameter values of the SA model fits to all 259 robustly tuned PV+ interneurons at different levels of PV+ optogenetic stimulation. Diamond markers indicate mean values (in polar coordinates) over neurons, colored arc lines the circular SD of the polar angles. **B2:** Same as B1, but for conductance-based model fits describing indirect photostimulation effects on all 228 robustly tuned PCs, assuming a saturating additive model description of interneurons. **C2:** Same as C1, but for the conductance-based model fits to all robustly tuned PCs.

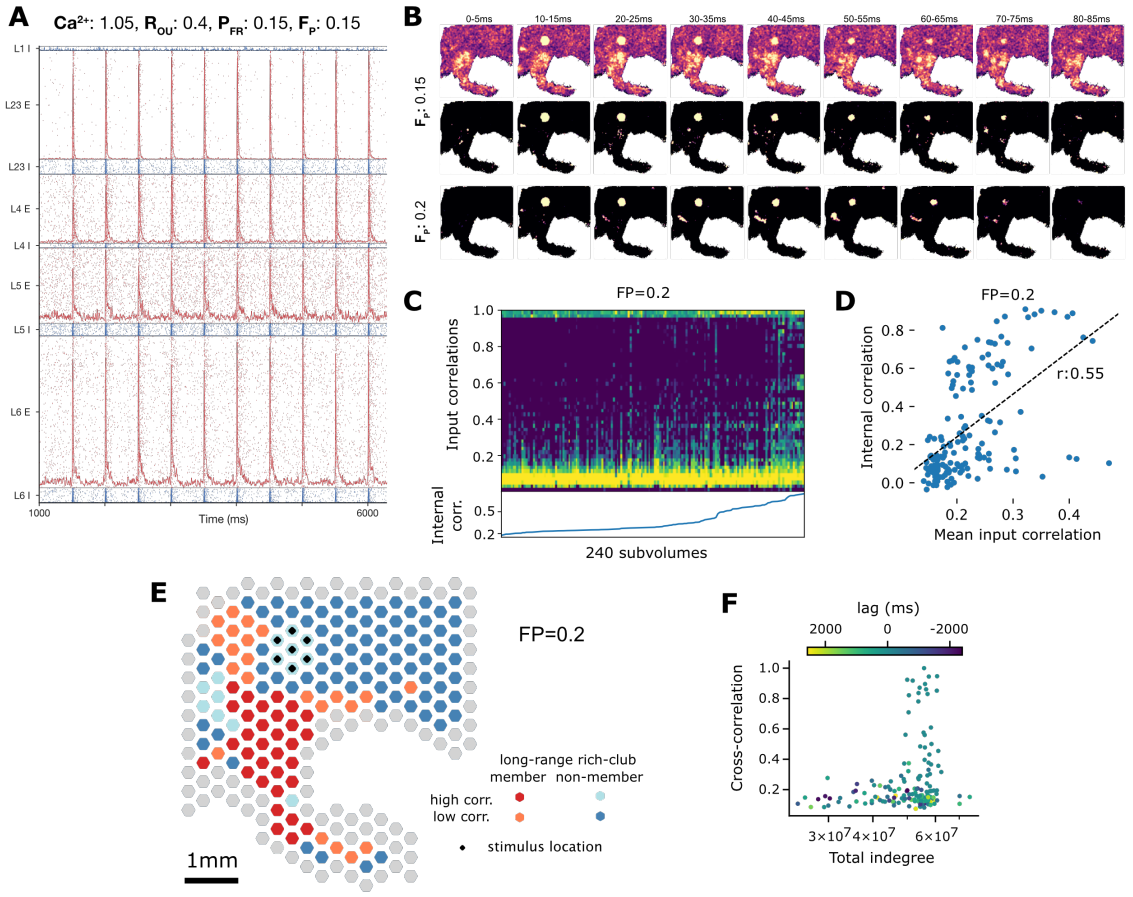

Figure S9: **Full nbS1 - supplementary**: **A:** Evoked responses of a single hexagonal over 10 single whisker deflections. **B:** Trial-averaged activity of the full circuit for $F_P = 15\%$ following the single whisker deflection stimulus (top). Middle and bottom: trial-averaged activity of the full circuit for $F_P = 15\%$ following the single whisker deflection stimulus for $F_P = 15\%$ and $F_P = 20\%$, showing only the top 2% of bins for each time window after the baseline activity level has been subtracted. **C:** Correlations of long-range inputs. B1: Distribution of spiking correlations of inputs into 240 subvolumes. Calculated at reduced spatial resolution, based on connection counts and correlations between the subvolumes (see Supp. Methods). Subvolumes are sorted by the E/I correlation of neurons within them. For evoked activity with $F_P = 20\%$. **D:** Mean of the correlations of inputs into 240 subvolumes against internal spiking correlation for all subvolumes during spontaneous activity. Black line: linear fit. Calculated based on connection counts and correlations between 50 μm hexagonal subvolumes (see Supp. Methods). **E:** Classification of subvolumes based on low or high internal correlation and membership in the long-range rich club. Data for evoked activity ($F_P = 20\%$). **F:** Indegree from the subvolume innervated by the VPM stimulus against correlation with that subvolume, indicated for all other subvolumes. Color indicates the Δt with maximum correlation.